Universitat
de les Illes Balears

DOCTORAL THESIS

2022

PAPER BIOSENSORS FOR THE RAPID DIAGNOSIS OF INFECTIONS AND SEPSIS USING PLASMONIC NANOPARTICLES

Francy Alejandra Alba Patiño

Universitat
de les Illes Balears

DOCTORAL THESIS

2022

Doctoral Program of Chemical Science and Technology

PAPER BIOSENSORS FOR THE RAPID DIAGNOSIS OF INFECTIONS AND SEPSIS USING PLASMONIC NANOPARTICLES

Francy Alejandra Alba Patiño

Thesis Supervisor: Roberto de la Rica Quesada
Thesis Tutor: Laura Daniela Ferrer Trovato

Doctor by the Universitat de les Illes Balears

Universitat de les Illes Balears

Dr Roberto de la Rica, principal investigator at the Health Research Institute of the Balearic Islands, Spain

DECLARE:

That the thesis titles *Paper biosensors for the rapid diagnosis of infections and sepsis using plasmonic nanoparticles,* presented by Francy Alejandra Alba Patiño to obtain a doctoral degree, has been completed under my supervision and meets the requirements to opt for an International Doctorate.

For all intents and purposes, I hereby sign this document.

Roberto de la Rica

Palma de Mallorca, Spain. April 19, 2022

ACKNOWLEDGEMENTS

I would like to thank Roche and Govern de les Illes Balears for a fellowship for doctoral studies “Stop fuga de cerebros”. Furthermore, I appreciate the opportunity to be part of the Multidisciplinary sepsis group and the Health Research Institute of the Balearic Islands (IdISBa).

I would like also thank to my lab partners for teaching me so many things and contributing to my development as a scientist. I appreciate the wonderful lab environment they have created.

I would also like to extend my thanks to the University of the Balearic Islands for its support, especially to the Chemistry department, and the Iberian Nanotechnology Laboratory for giving me the opportunity to do my PhD stay there, especially to the Water Quality group and Dr. Laura Rodriguez Lorenzo.

Finally, I wish to thank Dr. Roberto de la Rica for being my mentor since I arrived in Spain. Thank you for believing in me and supporting me during these years.

DEDICATORIA

Quiero dedicar esta tesis a toda mi familia en Colombia, a quienes agradezco todo el apoyo que me han brindado durante estos años fuera del país. Especialmente, a mis abuelas y abuelos por ser mis grandes maestros y mi inspiración cada día.

También, quiero dedicar este trabajo a mi familia en España, a Daniela, Fernando y Santiago por acompañarme en esta travesía de construir un futuro fuera.

Finalmente, quisiera agradecer a todas las personas que me han acogido en este país, y a quienes me han brindado su ayuda y su amistad, porque han hecho que mi vida aquí sea más sencilla y alegre.

ABREVATIONS

3D	Three dimensional
AFM	Atomic force microscopy
ALP	Alkaline phosphatase
AR	Augmented reality
AuNDs	Gold nanodumbbells
AuNPs	Gold nanoparticles
BAS	Bronchial aspirate
BSA	Bovine serum albumin
CCD	Charge-coupled device
ChOx	Cholesterol oxidase
CLSM	Confocal laser scanning microscopy
CMOS	Complementary metal-oxide-semiconductor
CMV	Cytomegalovirus
CRP	C-reactive protein
CS	Capture sites
DAMPs	Damage-associated molecular patterns
DLS	Dynamic light scattering
DTT	Dithiotreitol
EDX	Energy-dispersive X-ray spectroscopy
ELISA	Enzyme-Linked Immunosorbent Assay
EPS	Extracellular polymeric substances
FT-IR	Fourier transform infrared spectroscopy
gB	Glycoprotein B
HRP	Horseradish peroxidase
HSA	Human serum albumin
ICU	Intensive care unit
IL-6	Interleukin-6
LB	Luria−Bertani
LDH	Lactate dehydrogenase
LFT	Lateral flow test
LOD	Limit of detection
LOX	Lactate oxidase
LSPR	Localized surface plasmon resonance
MF	Mixed flora
MPI	Mean pixel intensity
MR-proADM	Mid-regional proadrenomedulin
oPADs	Origami paper-based analytical devices
PA	*Pseudomonas aeruginosa*
PCR	Polymerase chain reaction
PCT	Procalcitonin
PI	Pixel intensity or Polydispersity index
POC	Point of care
PSS	Polystyrene sulfonate
PTSD	Post-traumatic stress disorder
PVP	Polyvinylpyrrolidone
RGB	Red, green, and blue
RIA	Radioimmunoassay
ROI	Region of interest
RT	Room temperature

RT-PCR	Reverse transcription-polymerase chain reaction
SAXS	Small-angle X-ray scattering
SEM	Scanning electron microscopy
SERS	Surface-enhanced Raman spectroscopy
SIRS	Systemic inflammatory response syndrome
SOFA	Sequential Organ Failure Assessment
T-AgNPrs	Triangular silver nanoprisms
TEM	Transmission Electron Microscopy
TNF-α	Tumor necrosis factor-alpha
UV	Ultraviolet
XRD	X-ray diffraction
μPADs	Microfluidic paper-based analytical devices

INDEX

FIGURE INDEX

TABLE INDEX

EQUATIONS INDEX

ABSTRACT

Colorimetric paper biosensors based on nanotechnology are suitable for point of care testing, since paper is flexible, absorbent, cheap, light and can be easily disposed of by incineration. Colorimetric signals from these sensors are commonly produced by gold nanoparticles (AuNPs), since they exhibit intense colors due to their high molar extinction coefficient. Those signals can be detected by eye or by using a specialized reader. Recently, new approaches have used mobile phone cameras to detect those colorimetric signals, avoiding the need to purchase additional instruments. Although AuNPs are ideal for paper biosensors, one limitation of their use is the difficulty to achieve signal amplification, since the signal only depends on the extinction coefficient of the nanoparticles and the number of specific interactions with the target. Another limitation is that nanoparticles tend to adsorb irreversibly to paper substrates after drying, which makes it difficult to store them in reservoirs made of this material. To overcome this issue, glass fiber has been integrated in paper platforms such as lateral flow tests (LFTs). In fact, most LFTs are made of cellulose, nitrocellulose and glass fiber. However, the incorporation of materials is not fully compatible with biosensor designs such as origami paper-based analytical devices. These biosensors are meant to be entirely made of paper with the purpose of simplifying their fabrication and facilitating the contact between the parts without the use of additional adhesives.

In this PhD thesis a new and versatile technology that allows overcoming the limitations of traditional paper biosensors was developed. This versatile technology can be used for the rapid detection of both pathogens and sepsis marker proteins, in real matrices such as serum, blood, sputum and bronchial aspirate (BAS). It is important to diagnose infectious diseases quickly, since the organisms causing them can easily spread among the population through air, contaminated food, water or body fluids. Furthermore, unattended infections can progress to sepsis, an exaggerated response of the immune system to an infection that can lead to multisystem failure, and that can kill the patient in a few hours.

The following steps were taken in order to adapt paper biosensors for the detection of pathogens and protein biomarkers. First of all, some key aspects of the biosensor fabrication were optimized in order to reduce the assay time without losing sensitivity. This included implementing three AuNPs synthesis methods, such as the reduction of gold ions with either citrate, poly(allylamine hydrochloride) PAH or polyvinylpyrrolidone (PVP). Then, those AuNPs were covered with carboxylate or amine moieties, or polyvinylpyrrolidone (PVP)

respectively to carry out three different bioconjugation routes for protein attachment. Moreover, alternating layers of polyelectrolytes were used to improve the binding of the capture antibody to the paper substrate. Best conditions obtained from the experiments were applied for detecting the sepsis biomarker IL-6 in PBS with a limit of detection (LOD) of 0.1 $pg \cdot mL^{-1}$. Then, an increase in IL-6 of only 12.5 $pg \cdot mL^{-1}$ over basal levels was detected with 99% confidence, using whole blood from a healthy donor as biological matrix. The assay was completed in only 17 min.

Secondly, an ultrafast immunosensor made entirely of paper was developed. It implements a new design based on reservoirs for storing antibody-decorated nanoparticles on filter paper. This can be achieved by modifying the filter paper with the polymer polystyrene sulfonate (PSS). Once it is dry, a drop of AuNPs is added and let dry. Nanoparticles in the reservoir can be transferred with high efficiency to a receiving wet paper containing the analyte. Once transferred, AuNPs maintain their color and their bio-recognition function. To test this method, this reservoir was integrated in paper biosensors for the detection of the glycoprotein B from human cytomegalovirus spiked in serum samples. A LOD of 0.03 $ng \cdot mL^{-1}$ was obtained with a total assay time of only 12 minutes.

Afterwards, using the same immunosensor design, the pathogen *Pseudomonas aeruginosa* (PA) was detected in PBS, in only 8 min with a LOD of 10^5 $cells \cdot mL^{-1}$, which is the clinical threshold value for diagnosing an infection. This method relied on, using the endogenous catalase from respiratory samples (mainly produced by catalase-positive bacteria in the sample) to liquefy sputum samples. The liquefied samples were analyzed with the paper immunosensor. As a result, samples positive for PA were differentiated from negative samples, mixed flora samples and even from samples positive for other catalase-positive pathogen.

By implementing the new design with the reservoir, the first biosensors for detecting IL-6 was improved since the assay time was reduced below 10 min and the LOD decreased down to 10^{-3} $pg \cdot mL^{-1}$. Additionally, semi-quantitative measurements were acquired in a wide dynamic range between 10^{-3} and 10^2 $pg \cdot mL^{-1}$ when the matrix was PBS. Because of the low LOD of this immunosensor, blood samples spiked with IL-6 were diluted 1:1000 in order to minimize matrix interferences. Liquefied BAS samples were spiked with IL-6 and then they were also diluted 1:10 before they were analyzed. A dynamic range up to 10^2 $pg \cdot mL^{-1}$ was obtained in both cases. Following this protocol, IL-6 was detected in blood and BAS samples from COVID-19 patients. As a result, patients were stratified according to severity. The ability

of these biosensors to detect cytokines in blood and respiratory samples paves the way for monitoring local inflammation in the lungs as well as systemic inflammation levels in the body.

The colorimetric signals obtained from these four approaches were amplified by performing the assay on a folded piece of paper. The whole strategy is described in a previous work from our lab. On the other hand, colorimetric signals from the biosensors can be read by eye, by photographing the paper or with a smartphone-based densitometry app developed in our lab, making the proposed biosensors a semiquantitative tool. Furthermore, the high sensitivity and rapid turnaround time achieved by the optimizations accomplished and the fully automated densitometry app make our biosensors a complete analytical platform, well suited for measurements in a wide variety of healthcare settings and useful for the identification of potential sepsis cases.

RESUMEN

Los biosensores colorimétricos de papel basados en nanotecnología son adecuados para realizar mediciones en el punto de atención, ya que el papel es flexible, absorbente, económico, liviano y se puede desechar fácilmente mediante incineración. Las nanopartículas de oro (AuNPs) son el material generalmente empleado para producir las señales colorimétricas observadas en estos sensores. Esto es debido a que exhiben colores intensos ya que presentan un alto coeficiente de extinción molar. Esas señales pueden detectarse a simple vista o mediante el uso de un lector especializado. Sin embargo, recientes aplicaciones han utilizado cámaras de teléfonos móviles para capturar las señales, eliminando la necesidad de comprar instrumentos adicionales. Aunque las AuNPs son ideales para biosensores de papel, una limitación de su uso es la dificultad para lograr la amplificación de la señal, ya que la señal depende únicamente del coeficiente de extinción de las nanopartículas y del número de interacciones específicas con el analito objetivo. Otra limitación, es que, una vez secas, las nanopartículas tienden a adsorberse de forma irreversible a los sustratos de papel, lo que dificulta su almacenamiento en reservorios fabricados con este material. Una estrategia planteada para superar este problema, ha sido la integración en la fabricación, de otros materiales distintos al papel, como por ejemplo la fibra de vidrio, que es comúnmente usada en los sensores de flujo lateral (LFTs por sus siglas en inglés). De hecho, la mayoría de los LFTs están compuestos por 3 materiales distintos: la celulosa, la nitrocelulosa y la fibra de vidrio. Lamentablemente, la incorporación de varios materiales es un mismo dispositivo no es totalmente compatible con los diseños tipo origami, dispositivos analíticos hechos a partir de una sola pieza de papel doblado. Al ser completamente de papel se simplifica su fabricación y se permite que todas sus partes estén fácilmente en contacto, evitando el uso de adhesivos adicionales.

En esta tesis doctoral se desarrolló una nueva y versátil tecnología que permite superar las limitaciones de los biosensores de papel tradicionales. Esta tecnología versátil se puede utilizar para la detección rápida tanto de patógenos como de proteínas marcadoras de sepsis, en matrices reales como suero, sangre, esputo y aspirado bronquial (BAS por sus siglas en inglés). Respecto de las enfermedades infecciosas, es importante diagnosticarlas rápidamente, ya que los organismos que las producen pueden propagarse fácilmente entre la población a través del aire, alimentos, agua o fluidos corporales contaminados. Asimismo, infecciones desatendidas pueden progresar a sepsis, una respuesta exagerada del sistema

inmunológico ante una infección que puede provocar una falla multisistémica que puede matar al paciente en unas pocas horas.

Con el fin de adaptar los biosensores de papel para la detección de patógenos y biomarcadores proteicos, se optimizaron algunos aspectos claves de la fabricación como la reducción el tiempo de ensayo sin perder sensibilidad. Esto incluyó la ejecución de tres métodos de síntesis de AuNPs, tales como la reducción de iones de oro con citrato, poli(clorhidrato de alilamina) PAH o polivinilpirrolidona (PVP). Luego, las AuNPs se cubrieron con grupos carboxilo, amino, o polivinilpirrolidona (PVP), respectivamente, para posteriormente ser modificadas con proteínas a través de 3 vías. Del mismo modo, se estudió el uso de capas alternas de polielectrolitos sobre el papel, para mejorar la unión del anticuerpo de captura al sustrato. Las mejores condiciones obtenidas de los experimentos anteriores se aplicaron para la detección en PBS del biomarcador de sepsis interleuquina 6 (IL-6), obteniendo un límite de detección de 0,1 $pg \cdot mL^{-1}$. Posteriormente, empleando el mismo sensor, fue posible detectar un aumento de IL-6 de sólo 12,5 $pg \cdot mL^{-1}$ sobre los niveles basales con un 99% de confianza y utilizando como matriz biológica una muestra de sangre total de un donante sano. El ensayo se completó en sólo 17 min.

En segundo lugar, se desarrolló un inmunosensor ultrarrápido fabricado completamente en papel. Este dispositivo implementa un nuevo diseño basado en reservorios que almacenan nanopartículas decoradas con anticuerpos en papel de filtro. Esto se logró modificando el papel de filtro con el polímero de carga negativa poliestireno sulfonato (PSS). Una vez seco el polímero sobre el papel, se le añade una gota de AuNPs y se deja secar. Las nanopartículas en el reservorio se pueden transferir con gran eficacia a un papel húmedo receptor que contiene el analito. Una vez transferidas, las AuNPs mantienen su color y su función de biorreconocimiento. Para probar este método, se integró este reservorio en biosensores de papel para la detección de la glicoproteína B del citomegalovirus humano añadido a muestras de suero. Se obtuvo un límite bajo de detección de 0,03 $ng \cdot mL^{-1}$ con un tiempo total de ensayo de solo 12 minutos.

Posteriormente, utilizando el mismo diseño, se detectó el patógeno *Pseudomonas aeruginosa* (PA), en solo 8 min con un límite de detección en PBS de 10^5 $células \cdot mL^{-1}$, que es el valor umbral clínico para diagnosticar una infección. Para poder detectar esta bacteria en muestras de esputo, fue necesario introducir un nuevo método que licuara las muestras, ya que su alto contenido de mucinas las hace muy viscosas y densas y, por lo tanto, difíciles de manipular. Este método se basaba en el uso de la catalasa endógena de las muestras

respiratorias (principalmente producida por bacterias catalasa positivas en la muestra) para licuar muestras de esputo. Las muestras licuadas se analizaron con el inmunosensor de papel. Como resultado, fue posible diferenciar las muestras positivas para PA de las muestras negativas, de las muestras con flora mixta e incluso de las muestras positivas para otros patógenos productores de catalasa.

El implementar el nuevo diseño con el reservorio, permitió mejorar los resultados obtenidos con los primeros biosensores que detectaban IL-6. En primer lugar, el tiempo de ensayo se redujo por debajo de los 10 min y, en segundo lugar, el límite de detección (LOD) disminuyó hasta 10^{-3} pg·mL^{-1}. Adicionalmente, se adquirieron medidas semicuantitativas en un amplio rango dinámico entre 10^{-3} y 10^{2} pg·mL^{-1} cuando la IL-6 estaba resuspendida en PBS. Debido al LOD tan bajo de este inmunosensor, muestras de sangre ala cuales se les añadió IL-6 se pudieron diluir 1000 veces para minimizar las interferencias de la matriz, sin afectar la medición. Por otro lado, muestras de BAS previamente licuado se les añadió IL-6 y luego se diluyeron 10 veces antes de ser analizadas. En este caso la dilución de la muestra tampoco afectó a la medición y en cambio los interferentes de la misma se vieron reducidos. Viendo que era posible la detección en muestra complejas, se siguió el mismo protocolo para detectar IL-6 en muestras de sangre y BAS de pacientes con COVID-19. Co los resultados obtenidos, los pacientes fueron estratificados según la gravedad. Es importante resaltar que, la capacidad de estos biosensores para detectar citoquinas en sangre y muestras respiratorias abre el camino para monitorear simultánea y rápidamente la inflamación local en los pulmones, así como los niveles de inflamación sistémica en el cuerpo.

Las señales colorimétricas obtenidas en estas cuatro aplicaciones se amplificaron realizando el ensayo en una tira de papel doblada. Toda la estrategia de amplificación de la señal se describe en un trabajo anterior de nuestro laboratorio. Por otro lado, las señales colorimétricas de los biosensores se pueden ver y analizar a simple vista, fotografiando el papel o con una aplicación móvil de densitometría desarrollada en nuestro laboratorio. Lo anterior, convierte a los biosensores propuestos aquí en una herramienta semicuantitativa. Además, la alta sensibilidad y el rápido tiempo de respuesta logrados por las optimizaciones realizadas junto con la implementación de la aplicación móvil de densitometría, hacen de nuestros biosensores una plataforma analítica completa, muy adecuada para mediciones varios entornos de atención médica y útil para la identificación de posibles casos de sepsis.

RESUM

Els biosensors colorimètrics de paper basats en nanotecnologia són adequats per realitzar mesures al punt d'atenció, ja que el paper és flexible, absorbent, econòmic, lleuger i es pot rebutjar fàcilment mitjançant incineració. Les nanopartícules d'or (AuNPs) són el material generalment emprat per produir els senyals colorimètrics observats en aquests sensors. Això és perquè exhibeixen colors intensos i que presenten un alt coeficient d'extinció molar. Aquests senyals es poden detectar a simple vista o mitjançant un lector especialitzat. A més, en aplicacions recents s'han utilitzat càmeres de telèfons mòbils per capturar els senyals, eliminant la necessitat de comprar instruments addicionals. Encara que les AuNPs són ideals per a biosensors de paper, una limitació del seu ús és la dificultat per aconseguir l'amplificació del senyal, ja que el senyal depèn únicament del coeficient d'extinció de les nanopartícules i del nombre d'interaccions específiques amb l'analit objectiu. Una altra limitació és que, un cop seques, les nanopartícules tendeixen a adsorbir-se de forma irreversible als substrats de paper, cosa que dificulta el seu emmagatzematge en reservoris fabricats amb aquest material. Una estratègia plantejada per superar aquest problema ha estat la integració en la fabricació d'altres materials diferents del paper, com ara la fibra de vidre, que és comunament utilitzada en els sensors de flux lateral (LFTs per les sigles en anglès). De fet, la majoria dels LFTs estan compostos per 3 materials diferents: la cel·lulosa, la nitrocel·lulosa i la fibra de vidre. Malauradament, la incorporació de diversos materials en un mateix dispositiu no és totalment compatible amb els dissenys tipus origami, dispositius analítics fets a partir d'una sola peça de paper doblegat. El fet de ser completament de paper en simplifica la fabricació i es permet que totes les seves parts estiguin fàcilment en contacte, evitant l'ús d'adhesius addicionals.

En aquesta tesi doctoral es va desenvolupar una tecnologia nova i versàtil que permet superar les limitacions dels biosensors de paper tradicionals. Aquesta tecnologia versàtil es pot utilitzar per a la detecció ràpida tant de patògens com de proteïnes marcadores de sèpsia, en matrius reals com sèrum, sang, esput i aspirat bronquial (BAS per les sigles en anglès). És important diagnosticar ràpidament les malalties infeccioses, ja que els organismes que les causen es poden propagar fàcilment entre la població a través de l'aire, aliments, aigua o fluids corporals contaminats. A més, les infeccions no tractades poden progressar a sèpsia, una resposta exagerada del sistema immunològic davant d'una infecció que pot provocar una fallada multisistèmica que pot matar el pacient en poques hores.

Per tal d'adaptar els biosensors de paper per a la detecció de patògens i biomarcadors proteics, es van fer els passos següents. En primer lloc, es van optimitzar alguns aspectes claus de la fabricació del biosensor per reduir el temps d'assaig sense perdre sensibilitat. Això va incloure la implementació de tres mètodes de síntesi d'AuNPs, com ara la reducció d'ions d'or amb citrat, poli(clorhidrat d'alilamina) PAH o polivinilpirrolidona (PVP). Després, les AuNPs es van cobrir amb grups carboxil, amino, o polivinilpirrolidona (PVP), respectivament, per dur a terme tres rutes diferents de bioconjugació per a la unió de proteïnes a la superfície de les nanopartícules. Així mateix, es va estudiar l'ús de capes alternes de polielectròlits per millorar la unió de l'anticòs de captura al substrat de paper. Les millors condicions obtingudes dels experiments anteriors es van aplicar per a la detecció a PBS del biomarcador de sèpsia interleucna 6 (IL-6) obtenint un límit de detecció de 0,1 pg·mL-1. Després, fent servir el mateix sensor, va ser possible detectar un augment d'IL-6 de només 12,5 pg·mL-1 sobre els nivells basals amb un 99% de confiança i utilitzant com a matriu biològica una mostra de sang total d'un donant sa. L'assaig es va completar en 17 min.

En segon lloc, es va desenvolupar un immunosensor ultraràpid fabricat completament en paper. Aquest dispositiu implementa un nou disseny basat en reservoris que emmagatzemen nanopartícules decorades amb anticossos en paper de filtre. Això es va aconseguir modificant el paper de filtre amb el polímer de càrrega negativa poliestirè sulfonat (PSS). Un cop el polímer sobre el paper s'ha assecat, se li afegeix una gota d'AuNPs i es deixa assecar. Les nanopartícules al reservori es poden transferir amb gran eficàcia a un paper humit receptor que conté l'analit. Un cop transferides, les AuNPs mantenen el seu color i la seva funció de bioreconeixement. Per provar aquest mètode, es va integrar aquest reservori en biosensors de paper per a la detecció de la glicoproteïna B del citomegalovirus humà afegit a mostres de sèrum. S'obtingué un límit baix de detecció de 0,03 ng·mL-1 amb un temps total d'assaig de només 12 minuts.

Posteriorment, utilitzant el mateix disseny, es va detectar el patogen Pseudomonas aeruginosa (PA), en només 8 min amb un límit de detecció en PBS de 105 cèl·lules·mL−1, que és el valor llindar clínic per diagnosticar una infecció. Per poder detectar aquest bacteri en mostres d'esput, va caldre introduir un nou mètode que liqüés les mostres, ja que el seu alt contingut de mucines les fa molt viscoses i denses i, per tant, difícils de manipular. Aquest mètode es basava en l'ús de la catalasa endògena de les mostres respiratòries (principalment produïda per bacteris catalasa positius a la mostra) per liquar mostres

d'esput. Les mostres liquades es van analitzar amb l'immunosensor de paper. Com a resultat, va ser possible diferenciar les mostres positives en PA de les mostres negatives, de mostres amb flora mixta i fins i tot de les mostres positives per a altres patògens productors de catalasa.

Implementar el nou disseny amb el reservori va permetre millorar els resultats obtinguts amb els primers biosensors que detectaven IL-6. En primer lloc, el temps d'assaig es va reduir per sota dels 10 min i, en segon lloc, el límit de detecció (LOD) va disminuir fins a 10^{-3} pg·mL-1. Addicionalment, es van adquirir mesures semiquantitatives en unrang dinàmic entre 10^{-3} i 102 pg·mL-1 quan la IL-6 estava resuspesa en PBS. A causa del LOD tan baix d'aquest immunosensor, les mostres de sang a les quals se'ls va afegir IL-6 es van poder diluir 1000 vegades i així minimitzar les interferències de la matriu, sense afectar la mesura. D'altra banda, es va afegir IL-6 a mostres de BAS prèviament liquat que després es van diluir 10 vegades abans de ser analitzades. En aquest cas la dilució també va reduir les interferències sense afectar al valor de la mesura. Veient que era possible la detecció en mostres complexes, es va seguir el mateix protocol per detectar IL-6 en mostres de sang i BAS de pacients amb COVID-19. Amb els resultats obtinguts, els pacients van ser estratificats segons la gravetat. És important destacar que la capacitat d'aquests biosensors per detectar citocines en sang i mostres respiratòries obre el camí per monitoritzar simultàniament i ràpidament la inflamació local als pulmons i els nivells d'inflamació sistèmica al cos.

Els senyals colorimètrics obtinguts en aquestes quatre aplicacions es van amplificar fent l'assaig en una tira de paper doblegada. Tota l'estratègia d'amplificació del senyal es descriu en un treball anterior del nostre laboratori. D'altra banda, els senyals colorimètrics dels biosensors es poden veure i analitzar a simple vista, fotografiant el paper o amb una aplicació mòbil de densitometria desenvolupada al nostre laboratori. Això converteix els biosensors proposats aquí en una eina semiquantitativa. A més, la suma de l'alta sensibilitat, el ràpid temps de resposta i la implementació de l'aplicació mòbil de densitometria fan dels nostres biosensors una plataforma analítica completa, molt adequada per fer mesures en diversos entorns d'atenció mèdica i útil per a la identificació de possibles casos de sèpsia.

This PhD thesis is a compendium of the following accepted and published scientific articles:

1. **Paper biosensors for detecting elevated IL-6 levels in blood and respiratory samples from COVID-19 patients**. Adrover-Jaume, C., Alba-Patiño, A., Clemente, A., Santopolo, G., Vaquer, A., Russell, S. M., Barón, E., González del Campo, M. del M., Ferrer, J. M., Berman-Riu, M., García-Gasalla, M., Aranda, M., Borges, M., & de la Rica, R. (2021). Sensors and Actuators B: Chemical, 330, 129333. https://doi.org/https://doi.org/10.1016/j.snb.2020.129333

2. **Nanoparticle Reservoirs for Paper-Only Immunosensors**. Alba-Patiño, A., Adrover-Jaume, C., & de la Rica, R. (2020). ACS Sensors, 5(1), 147–153. https://doi.org/10.1021/acssensors.9b01937

3. **Nanoparticle-based mobile biosensors for the rapid detection of sepsis biomarkers in whole blood. Nanoscale Advances**. Alba-Patiño, A., Russell, S. M., Borges, M., Pazos-Pérez, N., Álvarez-Puebla, R. A., & de la Rica, R. (2020)., 2(3), 1253–1260. https://doi.org/10.1039/D0NA00026D

4. **Rapid Detection of Pseudomonas aeruginosa Biofilms via Enzymatic Liquefaction of Respiratory Samples**. Clemente, A., Alba-Patiño, A., Rojo-Molinero, E., Russell, S. M., Borges, M., Oliver, A., & De La Rica, R. (2020). ACS Sensors, 5(12), 3956–3963. https://doi.org/10.1021/acssensors.0c01618

These publications are enclosed at the end of this document.

1. INTRODUCTION

1.1 Biosensors

A biosensor is an analytical device that uses biomolecules like proteins, enzymes, antibodies, nucleic acids or hormones to specifically recognize an analyte [1]. These biomolecules are in contact with a transducer which transforms the biochemical reaction into a measurable signal [2]. The resulting signal will be optical, electrochemical, piezoelectric or thermometric (a short explanation and an example of each one can be seen in **Fig. 1.1**), among others, and can be used not only to detect but also to quantify the analyte [3].

Selectivity to the analytes of interest, reproducibility to produce identical responses, stability and robustness under ambient disturbances, sensitivity to analytes at very low concentrations to ensure their existence in the sample, and linearity in a wide range of concentrations are the most important characteristic of a biosensor [4]. Furthermore, it should provide rapid or even real-time responses [5].

The first biosensor developed in a laboratory was a glucose biosensor. It was developed by Clark and Lyons in 1962. After 10 years, in 1973, this glucose biosensor was first commercialized by Yellow Springs Instruments [6]. Since then, biosensors have been envisioned to play a significant analytical role in medicine, agriculture, food safety, bioprocessing, environmental and industrial fields [5]. In addition to glucose, a wide variety of metabolites such as lactate, cholesterol, and creatinine can be detected by using commercial biosensors. Many of these have small dimensions, simple construction and they are ideal for point-of-care sensing [6]. For example, the pregnancy test is a rapid, easy and inexpensive lateral flow test that is worldwide used. Similar devices that have achieved success in the clinical analysis field have detected analytes such as, *Escherichia coli* O157, influenza A and B viruses, *Helicobacter pylori*, human immunodeficiency virus, tuberculosis, and malaria [7]. Regarding the environmental field, commercial tests are used to monitor biochemical oxygen demand (BOD), nitrates and pesticides, among others [7]. For instance, the biofilm-type BOD biosensor consists of a layer of immobilized microorganisms (biorecognition element) sandwiched between a dialysis membrane and a gas-permeable Teflon membrane. When the water sample (e.g. wastewater, effluents and polluted waters) is injected into the system assimilable organic substrates diffuse and are assimilated by the immobilized bacteria, resulting in an increase in the oxygen consumption and therefore, a current decrease that will be detected by an oxygen electrode [8].

In the food industry, it is possible to measure glutamate, glucosa, lactose, etanol, citric acid using amperometric commercial devices which use enzymes as the recognition element [9]. Finally, to perform a biothreat/biowarfare analysis, commercial tests that detect Bacillus anthracis, Salmonella and Botulinum toxin can be used [6]. Moreover, the enhanced sensitivity achieved with nanobiosensors, will rapidly improve the current monitoring capacity and will reduce the cost [10].

Types: according to the transduction method

Electrochemical biosensor: measure the current or potencial produced from reactions between the analyte and the biomolecule (in which ions or electrons are produced or consumed) using an electrode as the transduction element. The electrical signal is mesured by potentiometry, conductometry, amperometry, or voltammetry.

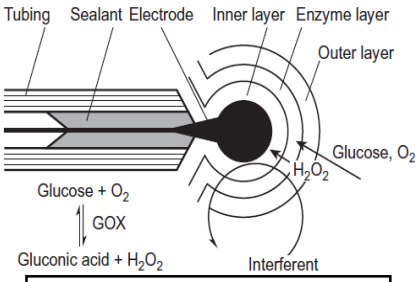

Glucose biosensor

Optical biosensor: Measure the change in the phase, amplitude, polarization, or frequency of the input light produced by the biorecognition process. It can be used for several types of spectroscopy (absorption, fluorescence, phosphorescence, Raman, SERS, refraction, and dispersion spectrometry). These changes can be also observed directly with bare eyes.

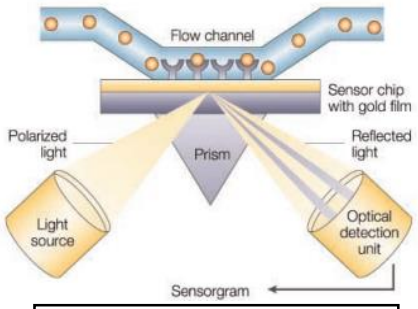

SPR biosensor scheme

Piezoelectric sensor: mesure the changes in resonance frequency of a piezoelectric transducer due to mass changes. The mass increases due to the binding of molecules. The resulting signal can be measured electrically. There are two types: the quartz crystal microbalance and the surface acoustic wave device.

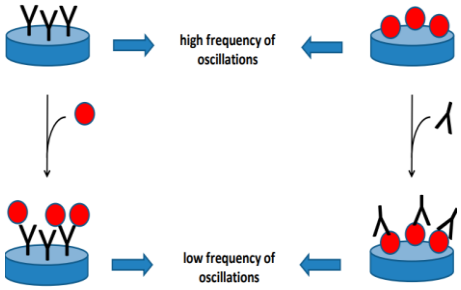

Piezoelectric immunosensor

Calorimetric (thermometric): Measure the total heat produced or absorbed in the biorecognition reaction, that is proportional to the total number of molecules in the reaction. A thermistor (usually metal oxide) or a thermophile (usually ceramic semiconductor) can be used as transducer. These devices do not require frequent recalibration and are insensitive to the optical and electrochemical properties of the sample.

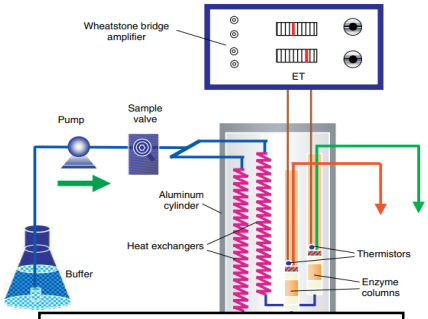

An enzyme thermistor

Fig. 1.1. Types of biosensors: according to the transduction method. [2][10][5][11][12] Examples: implantable glucose electrode[13], suface plasmon resonance biosensor[14], piezoelectric immunosensor [15], enzyme thermistor [16].All types of biosensors described above are well-developed and interesting tools that can detect analytes whit high specificity at low concentrations.

1.1.1 Optical biosensors

These devices employ the interaction of the optical field with a biorecognition element to detect an analyte. They can be divided in two types: 1) label-free: here, the signal is generated directly by the interaction of the analyte with the transducer; 2) label-based: this sensing-mode involves the use of a label (a molecule or nanoparticle in contact with the recognition element) to produce a colorimetric, radioactive, fluorescent or luminescent signal [17].

Surface plasmon resonance (SPR) based biosensors, Localized surface plasmon resonance (LSPR) based biosensors and Surface-enhanced Raman spectroscopy (SERS) based biosensors are some examples of the first type of optical biosensors. Currently, SPR is one of the most widespread and well-known technologies [18]. The SPR phenomenon takes place on the surface of metal when it is illuminated by polarized light at a specific angle. Then, surface plasmons are generated and the intensity of reflected light is reduced depending on the presence of the analyte on the surface of the transducer. To summarize, this technique enables direct, label-free and real-time detection of changes in the refractive index at the sensor surface, which is proportionate to the biomolecule concentration. To give specificity to this method, a biomolecule must be immobilized on the sensor surface [17].

In **Table 1.1** we compare some limitations and advantages of optical and electrochemical biosensors. Within the optical biosensors, specifically the colorimetric ones are mentioned in the table, since in this document the development of three different colorimetric approaches is described.

***Table 1.1**. Comparison chart: Limitations and advantages of colorimetric and electrochemical biosensors.*

Colorimetric Biosensors	**Electrochemical Biosensors**
Some limitations: • Colorimetric assays may present low sensitivity since it is often difficult to transform detectable signals into a color readout [19]. To solve this, a variety of nanomaterials, such as noble metal nanoparticles have been used [19]. Among them, gold nanoparticles stand out due to their high extinction coefficient which is 3 to 5 orders of magnitude higher than those of organic dye molecules [11]. • Amplifying the signal in colorimetric biosensors usually requires labile reagents and/or additional steps, which are not ideal for in-field measurements [20]. To manage this, nanomaterials can be implemented or some architecture modifications in the design of the biosensor could be made [20][21]. • Naked-eye detection of the color is not quantitative. It only works for qualitative analysis [22].	Some limitations: • Not all analytes are intrinsically capable to serve as redox partners in electrochemical reactions, because of that, a label must be introduced to promote the electrochemical reaction at the working electrode [4, 10]. • Power and extra equipment are required. However, their size can be reduced by using modern miniaturization/microfabrication technologies [6, 10]. • Electrochemical biosensors are sensitive to changes in temperature. They must remain a stable temperature or the output signal may be altered [23]. • Many electrochemical sensors need a reference electrode, which is difficult to miniaturize and when they are miniaturized, they do not last very long [24].
Some advantages: • When results are interpreted by eye, [19] they do not require any equipment for analysis, then, the cost for implementing these sensors can be significantly reduced. [11] • Most of them show quick response, are easy to fabricate and are advantageous for point-of-care testing. [4][19] [25] • These devices have been widely used for the quick detection of various analytes such as DNA, proteins, viruses, small molecules, metallic cations, bacteria and others. [25]	Some advantages: • They are among the mostly explored sensors because of their versatility, portability, and fast response. [26] • Most of the electrochemical devices have an excellent repeatability, accuracy and real time measurements. [11] • They show very good selectivity and strong sensitivity so that these sensors present a wide linear response range with low detection limits. [11]

1.1.2 Paper-based biosensors

Paper is a fibrous, soft, and porous matrix. Furthermore, this material is cheap, light, versatile, flexible, eco-friendly, accessible (available worldwide) and biocompatible. [27–29]

Furthermore, paper presents many properties that make it suitable for developing sensing platforms: [30, 31]

1. It can absorb reagents within its matrix avoiding the pipetting of reagent solutions by users and making it ideal for developing microfluidic devices.
2. Paper has a large surface area which allows the immobilization of a large number of sensor molecules and (bio)recognition elements.
3. Capability of self-pumping fluids within the substrate by capillary.
4. Can be chemically modified with biomolecules (e.g. proteins and antibodies) if required.
5. Can be easily sterilized,
6. Disposable by incineration.
7. Its characteristic white color leads to better contrast (e.g. in colorimetric strategies).
8. Paper is easy to produce (it is available in a wide variety of sizes, thicknesses and shapes), store and manipulate.

In the field of paper-based biosensors, different types of paper have been employed depending on the application of the sensor. The most extensively used materials in the literature are Whatman brand chromatography paper and filter grade paper due to their superior wicking ability and their highest content of the fluorophore-free cellulose mass [27, 28]. Nitrocellulose is the reference material for fabricating Lateral flow immunoassays due to the strong absorption of biomolecules through a combination of electrostatic, hydrogen, and hydrophobic forces [27, 32].

Paper-based biosensors can be constructed using common fabrication techniques such as wax printing, photolithography, inkjet printing, laser cutting, etc. at low cost, making them inexpensive and portable platforms for simple, fast and accurate monitoring that is immensely useful in resource-limited settings [27, 30].

1.1.3 Types of paper-based biosensors

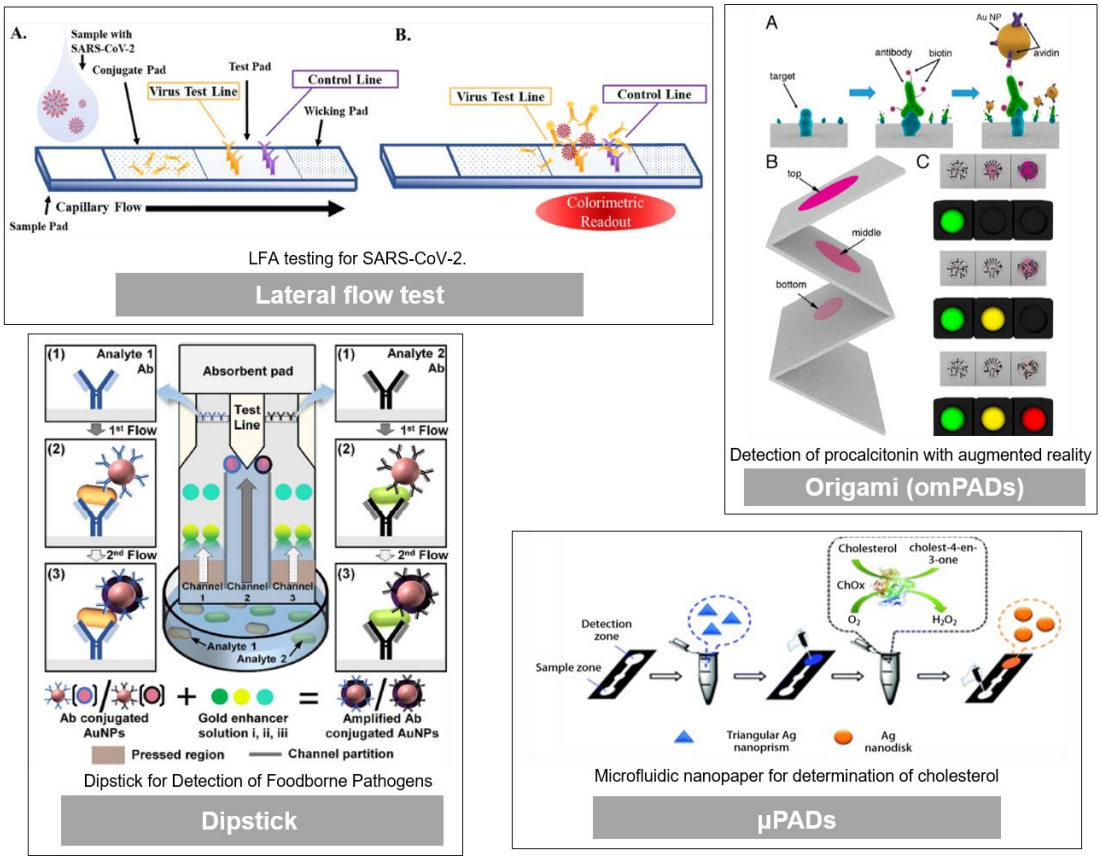

Fig. 1.2 *Applications of colorimetric paper-based biosensors. Dipstick* [33]*, Lateral flow test* [34]*, µPADs* [35]*, omPADs* [36]*.*

Paper-based biosensors can be found in different formats, from the simplest dipstick and lateral flow test, to the complex 3D microfluidic and origami analytical devices. All of them have proven to be useful to solve different issues by applying them in the diagnosis of several diseases, monitoring of health conditions (e.g. glucose and lactate levels [37, 38], cytokines increment) and detection of pathogens (virus, bacteria [39], fungi), as well as in the monitoring of environmental agents (e.g. pesticides in river water samples [40]) and controlling water and food safety and quality [27].

Dipsticks: these devices contain pre-deposited dry reagents within the paper substrate. Those reagents are rehydrated when are in contact with the sample solution. Then, they react with the analyte producing a detectable signal (colorimetric or electrochemical) [28, 29]. Dipsticks tests are simple to fabricate and provide rapid results. However, they are not suitable for quantitative analysis [28–30].

A scheme of paper-based dipstick that enables detection of foodborne pathogens can be seen in **Fig. 1.2**. In this approach, all the reagents required for assay are dried on the

nitrocellulose membrane (at different positions) and then they are sequentially rehydrated when the device is dipped into sample solution. Using this sensor *Escherichia coli* O157:H7 and *Salmonella typhimurium,* two fatal foodborne pathogens, were detected [33].

Lateral flow tests (LFTs): in this format, the flow of the liquid sample is controlled by using a narrow rectangle design and the combination of different materials [29, 30].

Four zones make up this strategy. First, the sample pad, a cellulose matrix for filtering the impurities and storing the dried buffer. Second, the conjugation pad, which is made of glass fibers for the storage of dried reagents. Third, the detection pad, a nitrocellulose matrix for capturing the reagents and for signal development. Finally, the adsorbent pad, made of a loose mass of cellulose fibers that provide a driving force to the sample, to flow through the 4 areas during the sensing process [28–30]. Usually, LFTs show two visible (colorimetric signal) bands when the analyte is in the sample [28–30].

A schematic representation of LFT for SARS-CoV-2 from the sample application and to test the results is observed in **Fig. 1.2**. Some antigen tests based on the detection of the SARS-CoV-2 spike and nucleocapsid proteins have been developed to increase population testing accessibility and to combat the enduring and dangerous spread of COVID-19 [34].

Microfluidic paper-based analytical devices (μPADs): they integrate hydrophobic barriers to construct microchannels that guide the flow of the sample. The required sample volume is minimal (microlitters). This format allows a more complex design which can branch out and in some cases can lead to a three dimensional (3D) device. These new designs favor multiplexing and quantitative analysis [28–30].

A simple enzyme-based biosensor that detects cholesterol by means of a colorimetric reaction is shown in **Fig. 1.2**. In this approach, triangular silver nanoprisms (T-AgNPrs) are etched by H_2O_2 produced when cholesterol oxidase (ChOx) is in the presence of cholesterol. As a result, after the etching process, a blue shift occurred and a color change from blue to light orange was observed [35].

Origami paper-based analytical devices (oPADs): these devices are fabricated using a single sheet of flat paper that is assembled by simple paper folding [41]. Origami-based techniques are used to stack different layers/reagents of the test in a vertical manner. The different reagents are dried at the designated areas of the device and then they are released by adding buffer or sample to the paper. Liquid flows through the cellulose fibers via capillary action, carrying reagents along the process through the different folded layers making

possible multi-step reaction assays into a single device [42]. The signal generated by these origami biosensors is then detected with electrochemical or optical methods [20].

A diagram of a new method for detecting different concentrations of proteins as well as light artifacts with origami immunosensors and digital logic is presented in **Fig. 1.2**. With this method, three colorimetric signals are produced due to the recognition of the analyte by AuNPs decorated with specific antibodies. The sample containing the analyte is dried on three different zones of a paper strip which is then folded like an accordion [20] allowing the vertical flow of the reagents. The signals are evaluated with an augmented reality app that generates a virtual semaphore that sequentially turns on its green, yellow and red lights depending on the concentration of analyte. The sepsis biomarker procalcitonin (PCT) was detected at clinically relevant concentrations by using this approach [36].

In this PhD thesis an origami design was chosen due to its advantages over the other formats that makes it ideal for our approaches. Some of them are:

- ✓ Compared with some 3D microfluidic systems, origami PADs do not require sequential layer-by-layer fabrication. In this case, the entire device is fabricated on one piece of paper [28–30, 41].
- ✓ Unlike LFTs that use at least 3 different materials (cellulose, nitrocellulose and glass fiber) for their fabrication, increasing the complexity in the fabrication process as well as their cost, origami PADs only use a sheet of paper. The speed of the fabrication process increase and its cost is reduced [41].
- ✓ The device can perform parallel tests by using a multilayer fluidic network to split a single fluidic sample into several detection regions for multiple biomarker detection, and the PAD can then be easily unfolded to observe the results in parallel. [42]
- ✓ The incorporation of additional layers should not result in much additional fabrication overhead, since increase the paper size could be enough [41]**.**
- ✓ Some origami PADs can be used for quantitative or semiquantitative analysis [28–30, 41].
- ✓ Origami PADs are highly suitable for use in public health, diagnostics, veterinary medicine, and environmental monitoring as point of care or point of need devices [42].

1.2 Gold nanoparticles

Gold nanoparticles (AuNPs) are nanomaterials currently used in many applications in different fields, due to their size and shape-dependent chemical, electronic and optical properties. For example, AuNPs present large surface-to-volume ratio, excellent electrical and heat conductivity, high chemical stability and inertness under physiological conditions. They possess excellent electrocatalytic properties, excellent biocompatibility, and low toxicity, as well as a strong absorption in the visible and near infrared wavelength region (380–750 nm) [11, 43, 44]. Their strong absorption in the visible region make them ideal to be used in optical biosensors, especially for the label-based sensing mode.

Michael Faraday's work began modern scientific evaluation of colloidal Au in the 1850s. He recognized that the color observed in the colloidal suspension was due to the nanoscale size of the Au particles [43, 45]. Then, in 1971, Faulk and Taylor first reported the use of AuNPs as labels for immunoelectron microscopy [46]. Nowadays AuNPs exhibit different sizes ranging from 1 nm to 400 nm and they are synthesized with various shapes and structures divided into three parts: [47–49]

1) one-dimensional: nanorods, nanowires, nanotubes, nanobelts.
2) two dimensional: gold nanoplates such as pentagons, squares/rectangles, dimpled nanoplates, hexagons, truncated triangles.
3) three dimensions: gold nanospheres, nanotadpoles, nanodumbbells (AuNDs), branched AuNPs such as nanopods, nanostars and gold nanodendrites [47–49].

Suspensions of gold nanospheres exhibit a brown, orange, red or purple color as their core size increases from 1 to 100 nm, and show a size-relative absorption peak from 500 to 550 nm. This absorption band (absent in both small nanoparticles (d < 2 nm) and the bulk material) is due to the collective oscillation of 6s electrons in the conduction band induced by the interacting electromagnetic field. This phenomenon is known as localized surface plasmon resonance (LSPR) and occurs when the incident photon frequency is resonant with the collective oscillation of the conduction band electrons. As a result, the radiation is absorbed and an absorption band can be observed [43, 44, 50]. LSPR is influenced not only by size and shape, but also by the solvent, the surface ligand, the core charge, the temperature and is highly sensitive to the distance among neighboring nanoparticles[44].

Surface plasmons of AuNPs, specially the large ones, have high molar extinction coefficients 3 to 5 orders of magnitude higher than those of organic dye molecules turning AuNPs in

ideal probes for colorimetric transduction [11, 43]. Furthermore, aggregation of the AuNPs can result in color changes, from pink to violet to pale blue. This aggregation can be produced by the presence of an analyte and the color change can be seen by eye. Aggregation can induce the coupling of the AuNPs plasmon modes, producing a red shift and broadening of the LSPR band followed by a gradual decrease of the plasmon peak at 520 nm and the appearance of a new peak between ~600-700 [43]. Normally, colloidal particles at the nanoscale present very short interparticle distances, consequently, they are attracted to each other by van der Waals, electrostatic or magnetic forces. This results in an unstable suspension of particles which tend to agglomerate [47].

Stabilization of colloidal Au is achieved either electrostatically or sterically by the use of various surface ligands or by a combination of both electrostatic and steric repulsion forces. Common colloidal stabilizers include charged small molecules, polymers and polyelectrolytes [37]. On the one hand, for electrostatically stabilized nanoparticles, aggregation is prevented when the electrostatic repulsion is sufficiently high [47]. However, if the ionic strength of the colloidal suspension increases due to the addition of electrolytes (high salt concentration), the charges on the surface of the gold nanoparticles become more screened, favoring interactions among AuNPs and triggering their subsequent aggregation [51].

On the other hand, in steric stabilization processes, colloidal particles are prevented from aggregation by adsorption of large molecules (e.g. polymers or surfactants) at the particle surface [47]. These substances provide a protective layer which works as a mechanical barrier against aggregation and whose efficiency will depend on the physico-chemical parameters of the polymer, its concentration and its solubility [48].

1.2.1 Synthesis methods

Synthesis can be:

- physical, such as laser ablation, sputter deposition, ion implantation, g-irradiation, optical lithography, microwave irradiation, ultrasound irradiation, and ultraviolet (UV) irradiation [47–49].
- chemical by the reduction of metal ions in solutions. Some chemical agents and stabilizing agents introduced are: sodium hydroxide, sodium borohydride, cetyl-trimethylammonium bromide, lithium aluminum hydride, sodium dodecyl sulfate, ethylene glycol and sodium citrate [47–49].

- biological, in which the solvent medium, reducing and stabilizer agents should be nontoxic and safe so that, hazardous generated wastes are reduced. Intra or extracellular extracts of prokaryotic cells (bacteria and actinomycetes) or eukaryotic cells (algae, fungi, and yeast), and extracts from various plants (leaves, stem, flower, fruits, peel, bark, and root) are used for this purpose [47–49].

Specifically, in the chemical synthesis of AuNPs, the reduction agent provides electrons to reduce the gold ions, Au^{3+} or Au^{+} to Au^{0} [50]. In other words, reducing agents turn the gold salts into their reduced form, producing insoluble atoms whose aggregation generates clusters that will grow to reach a nanoscale size and a characteristic morphology [52]. In this case, the greater the power and concentration of the reducing agent, the smaller the resultant particles will be [53]. Moreover, some reductants can act as stabilizing and reducing agent at the same time [52].

The most widely used chemical method for synthesizing AuNPs is the Turkevich method. Developed in 1951, in this method, hydrogen tetrachloroaurate (HAuCl4) is treated with sodium citrate in boiling water (**Fig. 1.3**) [54]. This method consists of two reactions, the initial redox reaction where trivalent gold gets reduced to monovalent gold by citrate which in turn gets oxidized to acetone dicarboxylate (DC^{2-}). Second, the disproportionation reaction takes place, and then, metallic gold (nanoparticles) and trivalent gold ions are produced [55]. Here, citrate acts as both reducing and stabilizing agent. Obtaining different particle sizes is possible by changing the gold-to-citrate ratio and controlling the pH and temperature of the reaction [44, 47, 50]. The resulting AuNPs have negatively charged citrate ions adsorbed on their surface and therefore they are stabilized against aggregation by electrostatic repulsion in solutions with low salt content [45, 49, 50].

R_1: initial redox reaction

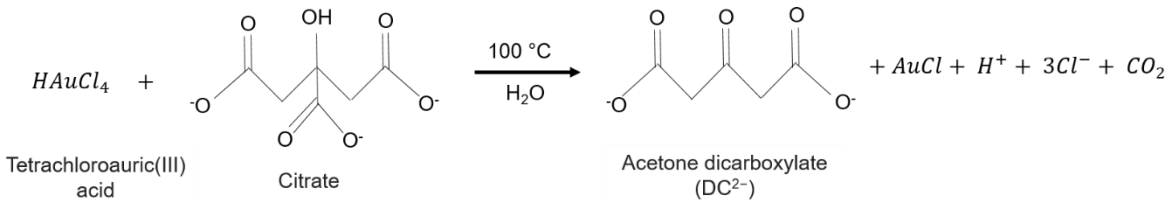

R_2: disproportionation reaction

$$3AuCl + Cl^- \longrightarrow 2Au^0 + AuCl_4^-$$

***Fig. 1.3**. AuNP synthesized by the Turkevich method. Adapted from*[55].

1.2.2 Functionalization methods

AuNPs can be functionalized with biomolecules such as proteins, antibodies, nucleic acids, enzymes etc., by covalent or non-covalent conjugation.

Non-covalent conjugation is widely utilized because it is easy (few steps and reagents are required) and sometimes reversible. In this approach biomolecules bind to AuNPs by different interactions such as through specific binding affinity, electrostatic interactions, and hydrophobic interactions [44]. For example, positively charged proteins bind to AuNPs surrounded by a layer of negative charges through electrostatic interactions [46]. Finally, since AuNPs present high affinity to thiol groups, molecules which possess these groups can attache to their surface through chemisorption [44, 46, 48].

To avoid flocculation of AuNPs during the functionalization process some parameters must be taken in count. First, the pH of the reaction must be controlled. Ideally, the reaction should occur at a pH within the range of the isoelectric point of the protein that is going to be attached or at slightly higher pH [46]. At this pH the net charge of the protein is zero, so that, the protein is not attracted or repelled by the particle. Aggregation can occur when both, the nanoparticle and the protein, have different surface charge. Then, they are electrostatically attracted, leading to aggregation and flocculation. On the other hand, repulsion between the protein and the particle is achieved when they have the same charge, thus resulting in a low yield of functionalization [56]. Second, a suitable concentration of the biomolecule must be added. The amount of biomolecule added to the gold particles should be slightly more (by about 10%) than the one needed to maintain colloidal stability upon addition of NaCl [46]. High overloads of protein should be avoided because this may promote aggregation [53].

Third, an evaluation of the degree of adsorption of the biomolecule and the relative coagulation of the gold particles must be done. This evaluation may be made for example by obtaining the extinction spectrum to observe if there are changes in the LSPR [53].

On the other hand, when more stable constructs are required, **covalent** conjugation of molecules to AuNPs is more appropriate. In this strategy, the reaction usually happens between free biomolecules in suspension and pre-grafted ligands (containing functional groups) on the AuNP surface [44]. Polyethylene glycol (PEG) is a polymer that usually is used for surface modification of AuNPs. PEG provides colloidal stability since PEGylated AuNPs repel each other for steric reasons [48, 49].

PEG is attached to AuNPs by thiol groups at one end. The other end may have another functional group such as carboxylate. This group can react with amines via an EDC (1-ethyl-3- (3-dimethylaminopropyl)carbodiimide)-mediated amidation reaction [53]. EDC activates the carboxylate particles to create intermediate EDC esters. These esters are reactive directly with amines on proteins or other molecules to create amide bond linkages [53]. More stable intermediates can be achieved by adding sulfo-NHS (N-hydroxysulfosuccinimide) to the reaction and in this way the immobilization course is better controlled (**Fig. 1.4**). Furthermore, since intermediate esters from sulfo-NHS are strongly negatively charged, they maintain the repulsive force between particles, keeping them from aggregation [53]. The same reaction may be used for covalent immobilization of proteins over primary amine particles. In this case, it is done by activation of a carboxylate group on the biomolecule and subsequent amide bond formation with the amines on the particles [53]. Also, the surface of an amine particle can be activated by coupling with an amine-containing ligand. For example, one can use a homobifunctional amine-reactive crosslinker such as glutaraldehyde or polyglutaraldehyde [53].

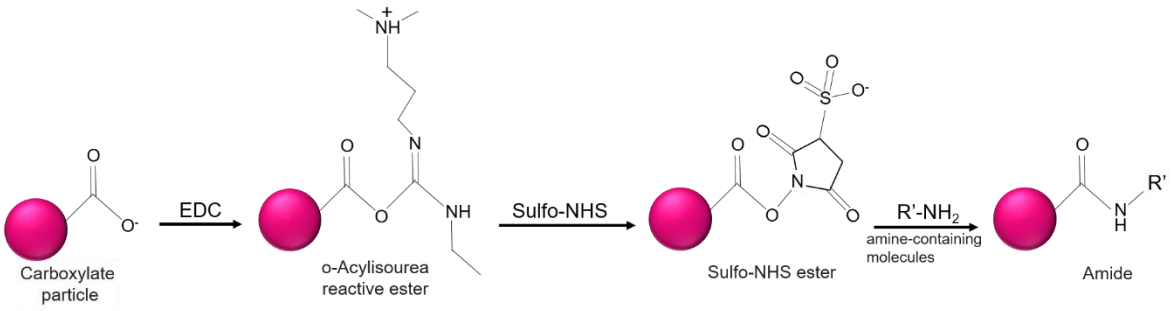

Fig. 1.4 .Functionalization of carboxylate particles by amidation reaction using EDC and sulfo-NHS (adapted from *[53]*).The role of biosensors in infections and sepsis diagnosis.

1.2.3 Infections

Infectious diseases (caused by bacteria, viruses, parasites or fungi) can rapidly spread among the population through air, contaminated food, water, body fluids or physical contact between person to person [57].

Virus have many characteristics that make them one of the major threats for mankind. For example, they have the ability to disseminate rapidly and their frequent mutations, reassortment and recombination give rise to the emergence of new and diverse viral populations [57]. Furthermore, there is a lack of specific vaccines and safe drugs for treatment of viral infections, as well as difficulties to develop efficient and sensible diagnostic techniques when the virus causing the infection is new or unknown [58]. Some diseases caused by viruses that must be prioritized for research and development in emergency contexts, according to WHO are: zika, ebola, Marburg, Crimean-Congo haemorrhagic fever, MERS-CoV and recently COVID-19 [58, 59].

Pathogenic bacteria possess characteristics that allow them to evade the body's protective mechanisms. When the body get in contact with pathogenic bacteria, a disease can be produced, either by the immune system response or by the pathogen which consumes the body resources to survive and reproduce [60]. Prompt diagnosis and timely treatment of bacterial infections caused mainly by Gram-negative microorganisms represent a particular challenge in human health worldwide [58]. Some pathogenic bacteria that can cause different kinds of diseases in humans, animals, and plants are: *Escherichia coli*, *Salmonella typhi*, *Clostridium perfringens*, *Shigella spp*., *Staphylococcus aureus and Pseudomonas spp.* [58]. The appearance of multidrug resistant variants of bacteria through the years has been favored by their indiscriminate exposure to antibiotics discharged in water or added to food. Although the principal factor is the improper use of these drugs in hospitals (excessive use, unfinished treatments, unnecessary use for viral infections) [57, 58]. The six pathogens responsible for the majority of nosocomial infections are: *Enterococcus faecium*, *Staphylococcus aureus, Klebsiella pneumoniae, Acinetobacter baumannii, Pseudomonas aeruginosa*, and *Enterobacter spp*.[61]. These microorganisms also exhibit multidrug resistance and virulence, and they are commonly known as ESKAPE pathogens [62].

Virus and bacteria detection is usually accomplished by molecular techniques such as the reverse transcription-polymerase chain reaction (RT-PCR), or traditional culture, which remains the gold standard for pathogen detection [58]. Body fluids used frequently for culture are: 1) blood, which is a red fluid composed by proteins such as fibrinogen, albumin

and immunoglobulins; electrolytes (e.g. sodium, potassium, bicarbonate, chloride, and calcium); cells (erythrocytes, leukocytes, and thrombocytes) and other small amounts of enzymes, hormones, and vitamins [63]. Removing the cells from blood a light-yellowish or straw-colored fluid called plasma is obtained, while plasma without fibrinogen is called serum [63]. 2) Respiratory samples such as sputum are made of highly cross-linked mucins with a highly viscous or even semisolid consistency samples so that, these samples require liquefaction and homogenization to be analyzed. The routine method for the liquefaction of respiratory samples involves the addition of dithiothreitol (DTT), which reduces disulfide bonds that cross-link mucins in the matrix. DTT is usually added for at least 30 min in a temperature controlled bath, followed by sample dispersion with a vortex [64]. 3) Urine, a yellowish fluid composed mainly by water, urea, creatinine, uric acid, and ions [65].

Identifying pathogens with these techniques requires a long time, and because of that, physicians frequently initiate empirical broad-spectrum antibiotic treatment in order to avoid poor outcomes. However the overuse of broad spectrum antibiotics, contributes to the emergence of resistant pathogens mentioned before [66]. The absence of rapid and accurate diagnostic information to direct treatment decisions at the point of care (POC) is one of the key barriers towards improving the management of infectious diseases [66]. Consequently, it is necessary to develop new strategies that allow the faster detection of these pathogens to effectively contain and control their impact on human health [58].

New approaches based on nanotechnological advances have emerged as suitable, easier, cost-efficient, and powerful diagnostic platforms for detecting pathogens. This helps healthcare professionals making informed clinical decisions based on the early detection of infectious viral/bacterial diseases [57, 58]. Many of these platforms have been developed utilizing nanomaterials because of their extraordinary optical, electrical and magnetic properties with highly active functional surfaces [57]. Some strategies to detect virus or bacteria in blood from infected patients can be seen in **Table 1.2**.

Table 1.2*. Biosensors for the detection pathogens in clinical samples. Adapted from* [67]

Pathogen	Technique	Support	LOD	Dynamic range	Analysis Time (min)	Ref
E. coli	Immunosensor + optical interferometry	Gold	10^2 cell mL^{-1}	10^2 - 10^5 cell mL^{-1}	40	[68]

E. coli *P. aeruginosa* *S. aureus*	antimicrobial peptide + SERS	Magnetic particles + Au coated Ag decorated graphene oxide nanocomposites	10 CFU mL^{-1}	10 - 10^6 CFU mL^{-1}	> 60	[69]
E. coli *P. aeruginosa* *S. aureus* *S. pyogenes*	Protein Aggregation assay + Fluorescence	Au and Cu Nanoclusters on paper	26 - 63 CFU mL^{-1}	10^2 - 10^8 CFU mL^{-1}	1	[70]
Antigen of Hepatitis C Virus	Aptasensor + conductivity mesurements	silicon-on-insulator nanowire structures	2 x 10^{-15} M	2 x 10^{-15} - 2 x 10^{-13} M	17	[71]
Hepatitis B Virus	Electrochemical immunosensor	graphene electrodes modified with gold nanoparticles	0.17 µg mL^{-1}	10 - 200 µg mL^{-1}	>60	[72]
IgGs, IgMs, and IgAs against SARS-CoV-2	recombinant protein + interferometric optical detection	Fabry-Perot interferometers: one layer of SiO2 and a thin SU-8 polymeric film	same as ELISA	---	>180	[73]
human immunodeficiency virus and co-infection with hepatitis C virus	DNA + electroluminescence	Ag electrode and ITO electrode	2 pM	1 nM – 1000 nM	>150	[74]

1.2.4 Sepsis

When the body responds in a dysregulated way to infection it can lead to life-threatening organ dysfunction [75–77]. This response is known as sepsis and the clinical criteria for identifying it includes suspected or documented infection and an acute increase of two or more Sequential Organ Failure Assessment (SOFA) points as a proxy for organ dysfunction. A subset of sepsis in which underlying circulatory and cellular/metabolic abnormalities are profound enough to increase mortality substantially is called septic shock [77]. Both, sepsis and septic shock can result from an infection anywhere in the body, such as pneumonia, influenza, or urinary tract infections. Bacterial infections are the most common cause of sepsis [78]. Worldwide, the incidence rate for sepsis is about 20.7 million and it is expected to increase gradually [75]. Sepsis is more frequent in

immunocompromised individuals such as cancer patients or the elderly, who often present confounding factors such as chronic inflammation and dysregulated body temperature [67]. It is estimated that one-third of people who develop sepsis die and those who survive are left with life-changing effects, such as post-traumatic stress disorder (PTSD), chronic pain and fatigue, organ dysfunction and/or amputations [78]. Sepsis is strongly time dependent since it usually starts as a non-lethal systemic inflammatory response syndrome (SIRS) and then it progresses to multiorgan dysfunction [67].

Early recognition and diagnosis of sepsis together with providing the proper medication at the right time is required to prevent the transition into septic shock and to reduce the mortality rate [75, 77]. Measuring the alterations of the host response to an infection is a faster alternative to the SOFA score for guiding the diagnosis of an infection that can lead sepsis. In fact, many diagnosing algorithms include measurements of serum biomarkers, which in addition to vital constants and epidemiological data, can be used to predict sepsis cases [67]. Biomarkers are the biological molecules or features that can be measured objectively and act as indicators of physiological or pathological process or response to a therapeutic intervention [75, 76, 79]. Four broad classes of biomarkers are known: [79]

1. Diagnostic biomarkers which serve to establish the presence or absence of a disease or clinical condition.
2. Monitoring biomarkers which provide information regarding the effectiveness of a given therapy for the purpose of titration.
3. Surrogate biomarkers which provide information regarding the effectiveness of a given therapy, but for the purpose of predicting a clinical outcome.
4. Stratification biomarkers which serve to stage or subclassify diseases based on outcome risk, severity, or biological mechanism.

Sepsis biomarkers include the acute-phase proteins such as cytokines and chemokines, the damage-associated molecular patterns (DAMPs), endothelial cell markers, leukocyte surface markers, micro RNA (miRNAs) and soluble receptors, as well as metabolites and alterations in gene expression (transcriptomics) [67, 76]. For example: c-reactive protein (CRP) has a prognosis value as high CRP levels can be linked to the severity of the infection and lower CRP values might indicate a favorable response to the antibiotic treatment [67]. In a different way, procalcitonin (PCT) is a diagnosis biomarker of sepsis which has been incorporated into clinical decision algorithms to guide both initiation and discontinuation of antibiotics [67, 79] while Interleukin-6 (IL-6) is a good biomarker for both, prognosis and

diagnosis. On the other hand, lactate is a useful biomarker for monitoring tissue oxygenation and also an excellent prognosis biomarker of sepsis [67]. Some others useful biomarkers are: mid-regional proadrenomedulin (MR-proADM), the neutrophil surface receptor expression (CD64), the tumor necrosis factor-alpha (TNF-α),Interleukin-27 (IL-27), CD14 (sCD14-ST or presepsin) and Interleukin-8 [67, 75].

Identifying, developing, evaluating, and validating sepsis-related biomarkers is an arduous process since novel sepsis biomarkers are useful only if they improve upon existing tools or provide new information [79].

Time-dependent variations in concentration of biomarkers are observed as sepsis progresses. For that reason, to correctly reflect the patient status, biomarker measurements must be rapid. Additionally, as they fluctuate over time, more than one biomarker should be measured in order to identify sepsis independently of disease stage [67]. Decentralized measurements are also important because sepsis is managed in a wide variety of healthcare settings, from ambulances to the emergency room, medical and surgical wards or the ICU [67].

The above mentioned issues could be overcome by using simple and sensitive biosensors implementing nanotechnological components for the frequent and rapid testing of multiple sepsis biomarkers at very low concentrations in biological fluids [67, 75]. These tools should be compact devices that are widely available and whose results at each step of the healthcare chain can be collated and shared with other healthcare workers. Also, biosensor readers must be portable and inexpensive, in order to ensure their widespread implementation [67].

A large number of biosensors has been developed for the diagnosis of sepsis using different biomarkers. **Table 1.3** shows the main characteristics of new biosensors developed to detect the most common sepsis biomarkers in real clinical samples. According to the table most of the strategies to detect lactate use amperometry as transduction method, employing electrodes made of different materials and functionalized with lactate oxidase (LOX) or lactate dehydrogenase (LDH) enzymes. Furthermore, the analysis time is the shortest since the signal can be read just in seconds. In case of IL-6, CRP and PCT most of the applications described in the table use antibodies as recognition element but different transduction methods to obtain the signals.

Table 1.3 *Biosensors for the detections of the sepsis biomarkers PCT, IL-6, CRP and lactated in clinical samples. Adapted from*[67]

Analyte	Technique	Support	Instrumental		Real matrix		Analysis time	Ref
			LOD	Dynamic range	Matrix	LOD		
PCT	Electrochemical	Antibody + ZnNPs-Functionalized carbon-silica nano-composites graphene oxide	13 fg mL^{-1}	50 pg mL^{-1} - 80 ng mL^{-1}	Serum	0.01 ng mL^{-1}	>40 min	[80]
		Antibody + Magnetic beads and carbon electrodes	90 pg mL^{-1}	0.25 - 100 ng mL^{-1}	Plasma	0.6 ng mL^{-1}	<20 min	[81]
		Antibody + Magnetic beads + gold electrodes	20 pg mL^{-1}	0.05 -100 ng mL^{-1}	Serum Plasma	---	< 15 min	[82]
	Chemiluminiscence	Antibody + Polydimethylsiloxane (PDMS)	250 pg mL^{-1}	250 pg mL^{-1} - 128 µg mL^{-1}	Serum	---	90 min	[83]
		Antibody + Optical fiber	11 pg mL^{-1}	0.05 - 200 ng mL^{-1}	Serum	---	>75 min	[84]
	Fluorescence	Antibody + Polypyrrole microtubes with a magnetic layer of nickel.	70 pg mL^{-1}	0.5−150 ng mL^{-1}	Plasma	1.1 ng mL^{-1}	>30 min	[85]

	luminescence	Antibody + core-shell mesoporous silica nanoparticles + polyvinyl chloride	0.5 ng mL^{-1}	1-200 ng mL^{-1}	plasma	---	>10 min	[86]
	Bioluminescence	Antibody + Magnetic nanoparticles Polystyrene nanospheres	45 ng mL^{-1}	1-10^4 pg mL^{-1}	Serum	0.25 ng mL^{-1}	1 h	[87]
IL-6	Electrochemical	Antibody + Gold electrode	0.1 pg mL^{-1}	0.01 pg mL^{-1} - 10 ng mL^{-1}	Human plasma	0.1 pg mL^{-1}	5 min	[88]
		Antibody + Nitrocellulose PVC Glass fiber	0.37 pg mL^{-1}	2–500 pg mL^{-1}	Human serum	-	15 min	[89]
	Chemiluminescence	Antibody + Polydimethylsiloxane (PDMS)	1.0 pg mL^{-1}	5 - 1280 pg mL^{-1}	Human serum	-	90 min	[83]
		Antibody + Optical fiber	1.05 pg mL^{-1}	5 to 10 000 pg mL^{-1}	Human serum	-	>75 min	[84]
	Colorimetric	Antibody + Paper + gold nanoparticles	10^{-3} pg mL^{-1}	10^{-3} - 10^2 pg mL^{-1}	Blood and bronchial aspirate	1.3 pg mL^{-1}	10 min	[90]
	Naked eye Optical spectroscopy	Antibody + Magnetic nanoparticles (MNPs) Polystyrene (PS) microparticles	11 pg mL^{-1} eye 1.2 pg mL^{-1} instr	3.7 - 900 pg mL^{-1}	Human serum	4.15 pg mL^{-1}	60 min	[91]
CRP	Electrochemical Micromotor	Carbon electrodes PtNPs	0.8 µg mL^{-1}	2-100 µg mL^{-1}	Plasma	0.80 µg mL^{-1}	5 min	[92]

	immunoassay	Polycarbonate	0.54 µg mL^{-1}	1-100 µg mL^{-1}	Serum Plasma	0.54 µg mL^{-1}	8 min	[93]
	Electrochemical Magneto immunosensor	Carbon electrodes	8 ng mL^{-1}	10-500 ng mL^{-1}	Plasma	8 ng mL^{-1}	<20 min	[81]
			1.5 ng mL^{-1}	5-1000 ng mL^{-1}	Blood Plasma		<15 min	[94]
	Electrochemical impedance device (EID)	Paper	-	5 ng mL^{-1} - 500 µg mL^{-1}	Serum	1 ng mL^{-1}	30 min	[95]
Lactate*	Amperometry	LOX + Screen-printed carbon electrodes with platinum nanoparticles decorated carbon nanofibers		25 µM - 1.5 mM	Blood	11 µM	60 s	[96]
		LOX + Reduced Graphene oxide, carbon nanotubes and AuNPs nanocomposite		0.05-100 mM	Blood	2.3 µM	80 s	[97]
		Graphene oxide nanoparticles modified pencil graphite electrode		5-50 mM	Serum	0.1 µM	5 s	[98]
		LDH + LDH NPs modified Au electrode		0.01 µM – 55 mM	Serum	0.01 µM	2.5 s	[99]
		LDH + Inkjet printed AuNPs/NiO NPs electrode		0.6-2.2 mM	Plasma	380 mM	60 s	[100]
		LDH + Pt-microneedle electrode- AuNPs-Polydopamine nanospheres		0.38-12 mM	Serum	50 µM	-	[101]

*only applications with a dynamic range within the ranges of physiological levels of lactate (> 0 mM) were included.

2. TECHNIQUES

2.1 Characterization of AuNPs

Characterizing a material requires to study its composition, structure, and properties (physical, chemical, electrical, and magnetic). Characteristics such as size, shape, composition, and surface properties of nanomaterials affect their activity and performance. Consequently, it is important to be able to measure those characteristics using reliable and advanced techniques, sensitive down to nanoscale dimensions [102, 103].

There are many techniques available for AuNPs characterization. For example, extinction spectroscopy can be used to characterize the LSPR of AuNPs. Through this technique, it is possible to monitor LSPR changes such as variations of peak intensity (LSPR dampening), a blue or red-shift or a broadening of the LSPR band, as well as the emergence of new ones. All of these parameters are related with to state of aggregation, colloidal dispersity, size, and shape of AuNPs [48]. Other techniques are: [48]

- Dynamic light scattering (DLS) to observe and measure the hydrodynamic diameter of AuNPs and their size distribution in suspension.
- X-ray diffraction (XRD) to confirm the purity and crystalline nature of AuNPs.
- Energy-dispersive X-ray spectroscopy (EDX) to confirm the chemical composition of AuNPs.
- Small-angle X-ray scattering (SAXS) analysis can be used to measure the interparticle distance in nanoparticle assemblies.
- Fourier transform infrared spectroscopy (FT-IR) to analyze the surface chemistry of AuNPs, and determine the composition of functional groups around them.
- Scanning electron microscopy (SEM), transmission electron microscopy (TEM), high-resolution transmission electron microscopy (HRTEM), and atomic force microscopy (AFM), are commonly employed to determine and characterize size, shape, and surface morphology of AuNPs.

The principle of the techniques used in this thesis to characterize AuNPs is described below.

2.2 Extinction spectroscopy

Spectroscopy is the study of the interaction between electromagnetic radiation and matter. Extinction refers to the attenuation of an electromagnetic wave by scattering and absorption when it passes through a particulate medium (e.g. a colloidal solution of gold nanoparticles) [104]. Briefly, light absorption results when the photon energy is dissipated due to inelastic processes, while light scattering occurs when the photon energy causes electron oscillations in the matter. The irradiated matter then emits photons in the form of dispersed light either at the same frequency as one from the incident light (Rayleigh scattering) or at a different one (Raman scattering) [105]. Since extinction is the result of both absorption and scattering, is described as follows:

$$\alpha_{ext} = \mathcal{N}(C_{abs} + C_{sca})$$

Eq 2.1Extinction equation [104]

In the last equation, extinction coefficient α_{ext} are related with the number of particles per unit volume $\mathcal{N}$, and with the absorption and scattering cross sections, C_{abs} and C_{sca} respectively. Cross sections refer to measure of the probability that a process will occur (in this case, the absorption or the scattering process) [104].

In regards to AuNPs, their capability of absorbing and scattering of light, is around 5 orders of magnitude stronger than most absorbing organic dye molecules and most strongly fluorescent molecules [105]. Although absorption and scattering occur simultaneously, there are instances where one or the other dominates [104]. For instance, absorption dominates over scattering when particles are small enough, while scattering dominates when the particle size is the same as or larger than the wavelength of the incident light [104].

As in this PhD thesis small spherical AuNPs (around 45 nm) were used, most of their extinction is due to absorption. Therefore, UV-visible spectroscopy was employed to analyzed them.

The Lambert-Beer's law establishes that, under certain fixed experimental conditions (radiation wavelength, optical path, temperature, among others), the absorbance of the chemical species varies directly proportional to their concentration. The following equation represents this law:

$$A = \varepsilon(\lambda)bc$$

Eq 2.2. Lambert-Beer's Law

Where A is the absorbance (without units associated), $\varepsilon(\lambda)$ is the molar extinction coefficient of the sample at a certain wavelength, b is the length in cm of the cuvette containing the sample, and c is the concentration of the sample. If the length of the cuvette is equal to 1 cm, the slope of the equation will be a constant equal to $\varepsilon(\lambda)*b$ so that, the absorbance will change depending on the concentration [102, 106].

In practice, the liquid sample to be analyzed is contained in a cuvette and then is placed in the radiation path where it is irradiated at a selected wavelength. When the light beam passes through the sample, a part of it will be absorbed, while the rest will pass through the solution to the detector [103]. This process also happens with a reference sample, so that, the amount of light passing through the reference is subtracted from that of the sample and then, this relative value is used to estimate the analyte concentration [106]. The ratio between the intensity of the relative transmitted light and the intensity of the incident light from the light source at a fixed wavelength is called transmittance, while the negative logarithm of transmittance is the absorbance [102].

A spectrophotometer is the instrument used for measuring the transmittance or absorbance of a sample. It is composed of six essential components: the light source which normally is a deuterium and tungsten lamp, the monochromator which focuses the polychromatic light generated from the source and selectively transmits only a narrow band of this light, a sample cell, a reference cell, the radiation detector, and a readout device. Additionally, a power supply is required for instrument operation [102, 106].

As commented above, UV-visible spectroscopy is used as a tool for identifying, characterizing, and studying nanomaterials. Specially, in characterizing metal nanoparticles, this strategy is a great tool for analyzing the size, shape, and surface properties of the nanoparticles when they are in a colloidal suspension [103]. Spherical gold nanoparticles present a characteristic absorption spectrum which falls in the 500–550 nm range depending on their size, shape, and dispersity (an example can be seen in **Fig. 2.1**). Alterations in these properties can be detected by observing their plasmon (bandwidth, variation on the intensity or a shift on the wavelength of the peak). For example, when the nanoparticle size increases, the absorption spectra shifts toward longer wavelengths. Also, when the nanoparticles are aggregated, the original extinction peak is reduced in intensity and often the band will broaden and a secondary band may appear at longer wavelengths [102].

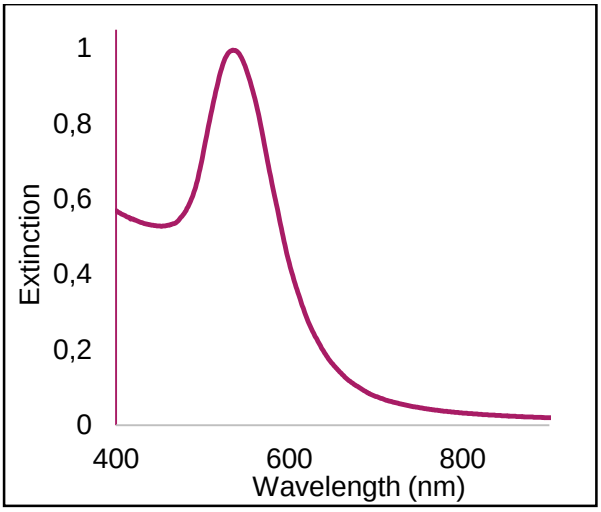

***Fig. 2.1**. Extinction spectra of 45 nm AuNPs.*

2.3 Transmission Electron Microscopy (TEM)

Nanomaterials can be imaged with atomic resolution with TEM when an incident high-energy electron beam is transmitted through an ultra-thin sample. Specifically, the electron beam is emitted by the electron gun (by thermionic, Schottky, or field emission with an electron energy normally of 80-300 keV, to be able to pass through material [107]) and then is focused by using a three- or four-stage condenser-lens system which permits variation of the illumination aperture and the area illuminated. When the focused electrons beam enters the thin specimen, it strongly interacts with the atoms of the sample and is transformed into unscattered, elastically scattered, or inelastically scattered electrons. Then, these scattered or unscattered electrons are focused on a series of electromagnetic lenses and then they are projected on a screen [102, 103, 107, 108]. The image of the material can be recorded by: 1) direct exposure of a photographic emulsion or an image plate inside the vacuum; 2) a fluorescent screen coupled by a fiber-optic plate to a CCD camera to obtain a digital image [108]. Elements with high atomic number have greater electron densities showing the greatest contrast in TEM images [102].

This technique is carried out under a high vacuum to avoid the deflection or attenuation of the electron beam by gas molecules in the air. Additionally, ultrathin sample sections (generally less than 1 μm) are required. Nevertheless, materials that have small enough dimensions such as powders, nanoparticles, and nanotubes do not need to be sectioned to be analyzed. Instead of that, they can be easily prepared by the deposition of a diluted sample containing the particles onto supported grids [102].

TEM has contributed significantly to nanotechnology development since it allows the evaluation of nanostructures including nanoparticles, carbon nanotubes, graphene, and thin films and fibers. A TEM analysis provides information about the number of material layers, composition, polymer tethering, and physical properties of nanomaterials such as shape, size and degree of aggregation and dispersion [48, 53, 102, 103, 107]. Even though AuNPs are 3D, in conventional TEM they are imaged mainly in two-dimensions. In practice, they are visible as dense, dark objects due to their high electron density [36, 39] as can be seen in **Fig. 2.2**.

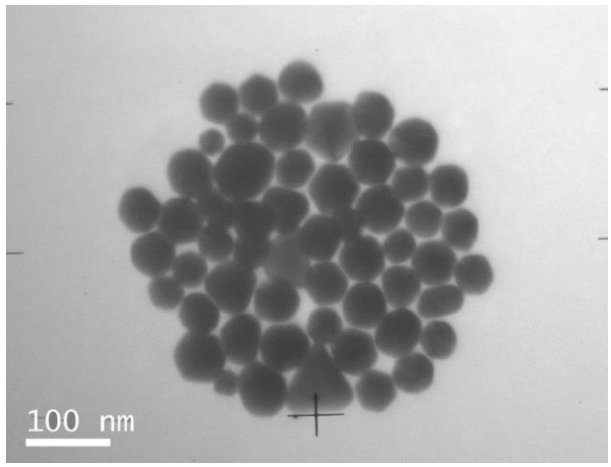

***Fig. 2.2**. TEM image of 45 nm AuNPs.*

2.4 Dynamic light scattering (DLS)

In DLS (also called photon correlation spectroscopy or quasielastic light scattering [103]), fluctuations of the Rayleigh scattering of light are measured. This elastic scattering is generated by the Brownian (random) motion of the nanoparticles with smaller size than the wavelength of the incident light, at a fixed scattering angle. Brownian movement is a result of the random collisions of the particles with the solvent molecules causing the particles to diffuse through the medium. Therefore, when a monochromatic light beam, such as a laser, irradiates in the visible light range a randomly moving suspension of nanoparticles, the light is scattered with a different frequency depending on the size of the particles [102, 109]. The following equation represent the intensity of the light scattered by an individual particle:

$$I = I_0 \frac{1 + \cos^2 \theta}{2r^2} \left(\frac{2\pi}{\lambda}\right) \left(\frac{n^2 - 1}{n^2 + 2}\right) \left(\frac{d}{2}\right)^6$$

Eq 2.3. Intensity of light scattered by a single particle.

I_o refers to the intensity of the incident light while λ is its wavelength, r is the distance of the scattering center, θ is the angle at which the light is scattered, n is the refractive index, and d is the particle diameter.[102, 109]

Large particles diffuse slower than smaller particles, so that, measuring this movement it is possible to acquire information regarding the average size, size distribution, and polydispersity in solution [102, 103]. The particle size obtained by DLS depends also on any surface coating, the medium in which the nanoparticles are suspended in, the type of electrolytes and the concentration of the medium. For example, nanoparticles covered with a polymer layer will have a lower diffusion speed, and therefore the size obtained by DLS will increase [48, 102]. The stability of the particles can be also studied by DLS since nanoparticle aggregates will give a larger particle size and the polydispersity index (PI) will increase (PI>1 is associated with aggregated nanoparticles). In this approach, the spherical nature of the particles is assumed so that, DLS is not appropriate to determine the precise size of nanoparticles of nonspherical geometries [102].

2.5 Electrophoretic light scattering to measure Z potential

Zeta potential also termed as shear surface electric potential or electrokinetic potential, is the potential at the slipping/shear plane of a colloid particle moving under an electric field [110]. It is usually determined by electrophoretic light scattering, measuring the velocity of charged species toward the electrode with an external electric field in a sample solution [103].

In other words, measuring the zeta potential of colloidal nanoparticles it is possible to know their surface charge. Nanoparticles with a net surface charge, either positive or negative, attract a thin layer of counterions that remain strongly bound on their surface (Stern layer). An electrical double layer is generated when the stern layer is surrounded by an outer diffuse layer made of lightly associated ions. As mentioned before, nanoparticles in solution move due to Brownian diffusion, this movement creates a gradient between the ions in the diffuse layer that move with the nanoparticle and those that remain within the dispersion medium [102]. The electrical potential produced by this gradient is called zeta potential (ζ) and is calculated from the Henry equation: [102]

$$\mu_\varepsilon = \frac{2\varepsilon\zeta}{3n} f(ka)$$

***Eq 2.4**. Henry equation.*

In **Eq 2.4** the electrophoretic mobility (μ_ε) is inversely proportional to the absolute zero-shear viscosity of the medium (n) and directly related to the dielectric constant (ε), the zeta potential (ζ), and the Henry function ($f(ka)$) where ka is a measure of the ratio of the particle [102].

The positive or negative dimensions of zeta potential are determined by identifying which electrode the particles are moving towards during electrophoresis [110]. The stability and aggregation state of the nanomaterials depend in part on their surface charge. For example, particles with high positive or negative surface charge tend to repel each other resulting in a stable colloidal solution. On the other hand, nanoparticles with low surface charge tend to agglomerate and precipitate. Usually, zeta potential takes values in the range of +100 to -100 mV. In practice, high degrees of colloidal stability in nanoparticles applications are linked to zeta potential values greater than +30mV or less than -30mV (strongly cationic or anionic). Alternatively, zeta potential values below +25mV or greater than -25mV tend to agglomerate the nanoparticles due to interparticle interactions, including van der Waals, hydrophobic and hydrogen bonding interactions. Finally, nanoparticles with zeta potential values close to 0mV (between -10 and +10mV) are considered neutral [102].

Changing the pH of the solution will result in an alteration of the zeta potential value as follows: zeta potential becomes more positive in magnitude with an acidic pH and more negative with a basic pH [110]. On the other hand, when the pH is close to the isoelectric point, nanoparticles loss of stability because of lack of charges leading to agglomeration or flocculation.

2.6 ELISA

The enzyme-linked immunosorbent assay (ELISA) is a biochemical assay that makes use of antibodies to specifically capture an analyte (e.g. proteins, peptides, hormones, antibodies), and enzymes for generating measurable signals (colorimetric, fluorescent or quimioluminescent) [111]. ELISA is derived from the radioimmunoassay (RIA), which was used to detect and measure biological molecules present in very small quantities by integrating a signal generation mechanism that made use of radioisotopes. Because of the safety concern regarding the use of radioactivity, RIA assays were modified by replacing the radioisotope with an enzyme [111]. Other advantage of this change was the improvement in the signal levels in two to three orders of magnitude greater than those obtained using radionuclides [112].

ELISAs is a highly versatile and sensitive technique that can be used for qualitative or quantitative determinations of practically any antigen. Reagents used in this technique are stable, nonradioactive, and, in most cases, available commercially [113].

Enzymes are used in this technique because they are highly specific and have catalytic activity, which can boost the yield of a reaction up to a billion times. Furthermore, enzyme signals increase with time due to the continuous transformation of the enzyme substrate, which enables a time-dependent signal amplification [112]. There are several enzymes suitable for ELISA but, alkaline phosphatase (ALP) and horseradish peroxidase (HRP) are the most commonly used. To enhance the sensitivity of the assay, the amount of enzyme bound to the antibody can be increased using various methods, for example by using biotinylated antibodies and enzyme-conjugated streptavidin [113].

Antibodies are another essential component to perform an ELISA, since they provide the basis of analyte selection and detection. Antibodies are immunoglobulins produced by B lymphocytes of the adaptive immune system. They can bind only to one type of **antigen** or immunogen, which are any molecule capable to provoke a response from the immune system. A monoclonal antibody specifically binds to just one portion of the antigen. This zone is called the antigenic determinant or **epitope**. The interaction between the antibody and the epitope is made possible by multiple noncovalent interactions similar to the interactions that confer specificity to enzyme-substrate reactions [114, 115].

Antibodies can be classified in many ways. For example, depending on the type of molecule they recognize, antibodies can be classified as primary or secondary. A primary antibody attaches to specific sites of the immunogen while a secondary antibody, attaches to the primary antibody [116]. Another classification of antibodies is polyclonal or monoclonal antibody. **Polyclonal antibody** is an antiserum produced from many responding clones of cells against an antigen. It presents a heterogeneous composition that includes an unknown combination of immunoglobulins of different specificity, classes and subclasses, titers, and affinities. The response to individual epitopes may be clonally diverse and antibodies of different affinities may compete for the same epitope. Furthermore, there is a high probability of cross-reactivity with other antigen with similar characteristics to the one to be detected (e.g. homologous protein family members) [114, 115]. Usually, this kind of antibody is used to detect the analyte once it has been selectively removed from a sample. On the other hand, **monoclonal antibody**, derived from single type of antibody-producing cells, is monospecific in nature and, thus, has a single affinity for a defined epitope [115]. In other

words, is a homogenous pool of identical immunoglobulins which bind to a single antigenic epitope with a high degree of specificity [114]. Because of its properties, this antibody is often used as a capture antibody, since it selectively attaches the antigen of interest from a sample, allowing the elimination of interfering molecules and the subsequent detection of the immunogen.

Depending on the way that the analyte is capture, ELISA configuration can change. Two different immunoassays are explained below:

- **Sandwich ELISA**: this technique is used to identify a specific antigen in a liquid sample. The well surface is coated with a known amount of capture antibody specific for the antigen. After blocking, the antigen-containing sample is applied to the plate. Then, a specific primary antibody is added, forming a sandwich configuration together with the capture antibody and the analyte. As in the previous configuration, enzyme-linked secondary antibodies may be applied to bind the primary antibody. The enzyme substrate is added and the color is produced. When a purified specific monoclonal antibody is used as a capture antibody, there is no need to purify the sample previously. Due to this, the assay is simplified and its specificity and sensitivity is increased [111]. In this case, both polyclonal and monoclonal antibodies may be used. Furthermore, for this approach to work, the analyzed antigen needs to have at least two separate binding sites for antibodies, so that, the analysis of small molecules is not recommended when using a sandwich assay [113].

- **Competitive ELISA:** in this assay there is a competition between the antigen in the sample and the antigen bound to the wells of the plate to be recognized by the primary antibody. First, the plate is coated with a known concentration of the antigen while the primary antibody is incubated with the sample containing the antigen. Then, the resulting antibody–antigen complexes are added to the previously coated wells. After an incubation period, any unbound antibody is washed off. Therefore, the more antigen in the sample, the more primary antibody will be bound to the sample antigen and the smaller amount of primary antibody available to bind to the antigen coated on the well. Finally, the secondary enzyme-conjugated antibody is added, followed by the enzyme substrate to produce the color. Contrary to the last two configurations,

in this approach the absence of color indicates the presence of antigen in the sample [111].

This technique has been widely used as diagnostic tools in medicine and as quality control measures in various industries; as well as in biomedical research for the detection and quantification of specific antigens or antibodies in a given sample [111].

2.7 Quantification of colorimetric signals: Densitometry

Since the response of many biosensors is a colorimetric signal produced by the biospecific accumulation of colorimetric probes, measuring those signals and recording the results will provide quantitative information about the analyte. Reflective densitometry is the standard technique used in many laboratories for this purpose. In practice, the colorimetric test is imaged and the region of interest (ROI) within the colored spot is manually selected. Finally, the average pixel intensity is measured and the resulting value is associated with the concentration of the analyte [117–119].

For example, a commercial lateral flow test (LFT) generally produces two red lines when the test is positive and one line when is negative. These lines can be detected with the naked eye for a qualitative analysis. However, for quantitative analysis, the optical density of these lines must be measured. This can be achieved by using a dedicated reader, a smartphone app or by imaging the test and then manually processing it with software (ImageJ, Photoshop, ect.). Imaging is usually performed using a charge-coupled device (CCD) or a complementary metal-oxide-semiconductor (CMOS) camera [22, 120]. These devices are the most commonly used because of the advantages of their simple structure and small size. These readers usually work as follows: first, an image of the test line is acquired as a set of red, green, and blue (RGB) image channels, which must be processed to obtain a single output measurement. Then, the mean pixel intensity (MPI) of the RGB channels within a region of interest (ROI) in the image is computed [120]. Finally, the data are analyzed taking in account the relationship between RGB values and the concentration of an analyte. It has been proved that this method has a good agreement with the absorbance visible-light spectrophotometer measurements [121].

3 OBJETIVES AND WORK METHODOLOGY

3.1 General objective:

To develop a new sensing platform completely based on paper and nanomaterials, capable of rapidly detecting both pathogens and sepsis protein biomarkers, in real samples from patients.

3.2 Specific objectives:

a) To evaluate several gold nanoparticles synthesis methods as well as gold nanoparticles biofunctionalization reactions with proteins.
b) To develop a nanoparticle reservoir in a paper substrate that allows to store protein decorated nanoparticles and to release them when needed.
c) To integrate the nanoparticle reservoir in a paper biosensor for detecting the virus Cytomegalovirus in a complex matrix.
d) To optimize the biosensor design parameters, such as analyte capture system, total assay time, sample pre-conditioning and signal reading method.
e) To implement both the reservoir and the optimized parameters, in paper biosensors for the detection of sepsis biomarkers such as interleukin-6 and pathogens such as *Pseudomonas aeruginosa*.
f) To improve the diagnosis of sepsis by detecting rapidly the mentioned analytes in blood and respiratory real samples from patients.

3.3 Work methodology

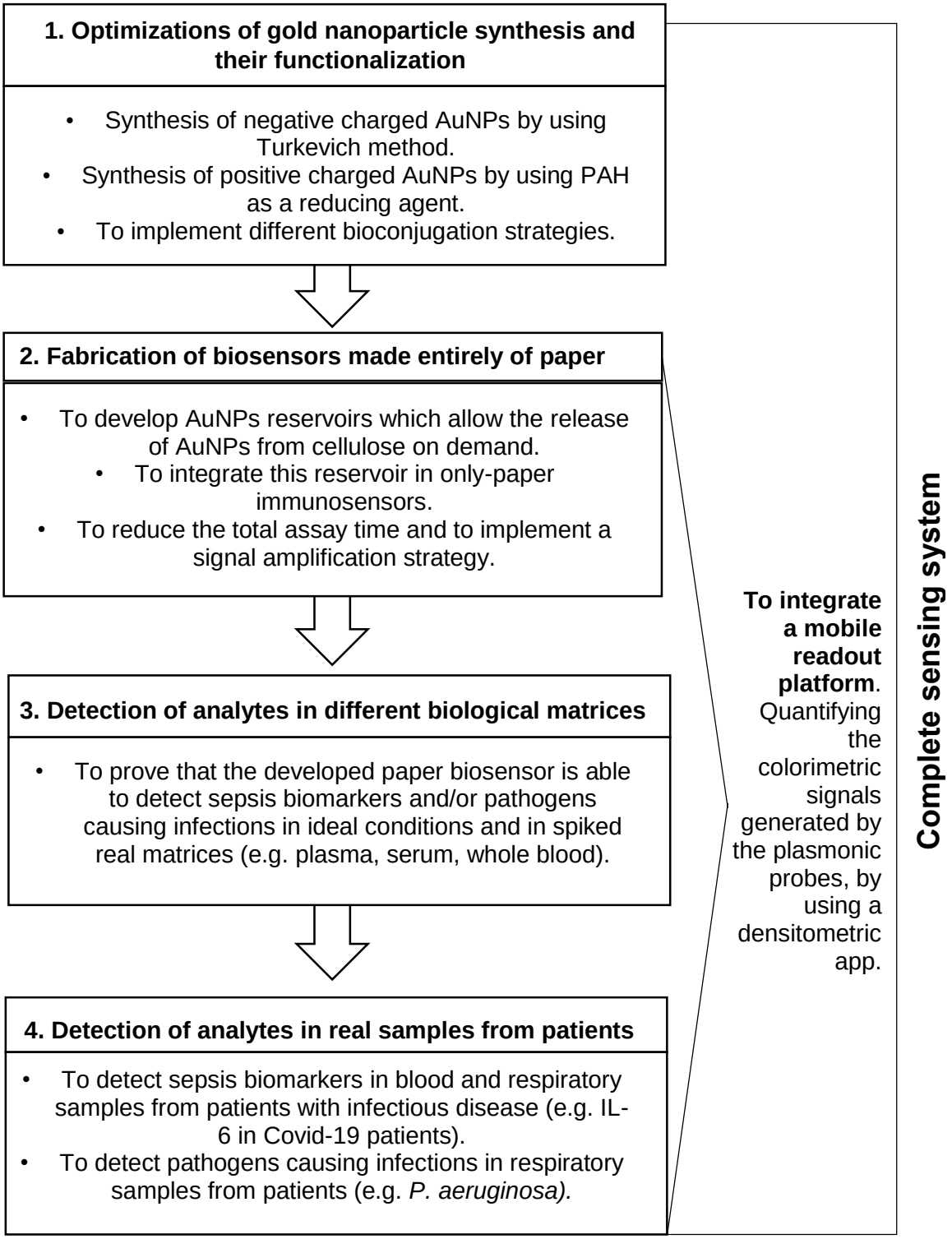

***Fig. 3.1**. Schematic representation of the work methodology.*

4 NANOPARTICLE-BASED MOBILE BIOSENSORS FOR THE RAPID DETECTION OF SEPSIS BIOMARKERS IN WHOLE BLOOD

4.1 Abstract

Detecting small variations in the levels of IL-6 is crucial for the early diagnosis of sepsis. To be useful in clinical decision-making, this requires detecting IL-6 rapidly in whole blood and with portable readers. Here we introduce immunosensors made of filter paper that use plasmonic nanoprobes to detect IL-6 rapidly in unprocessed blood with an unmodified smartphone. Key aspects of the biosensor fabrication were optimized in order to reduce the assay time without losing sensitivity. This included testing three bioconjugation routes for protein attachment to nanoprobes using gold nanoparticles covered with carboxylate or amine moieties, or polyvinylpyrrolidone (PVP), as starting materials, and using alternating layers of polyelectrolytes to bind the capture antibody to the paper substrate. Smartphone-based signal quantification was achieved with a custom-made app featuring a unique augmented reality guidance system that circumvents the need for smartphone attachments and automates all the steps involved in color quantification. The biosensors were able to detect IL-6 with a limit of detection of 0.1 $pg \cdot mL^{-1}$ and a total assay time within 17 min. They could also detect an increase in IL-6 of only 12.5 $pg \cdot mL^{-1}$ over basal levels in whole blood with 99% confidence. The high sensitivity and rapid turnaround time afforded by the optimized biosensors and the fully automated real-time densitometry app make our biosensors well suited for emergency healthcare situations such as the identification of potential sepsis cases.

4.1 Introduction

Sepsis, an overwhelming response to an infection leading to multiorgan shutdown, can cause death in a few hours if not treated straightaway [122]. It is also a major economic burden for healthcare providers, costing US$24 billion per year in the US alone [123]. Treating sepsis at a very early stage can improve patient outcomes and reduce associated costs [123]. Yet this requires identifying potentially septic patients rapidly, which is difficult when judging only from the presenting symptoms. Fortunately, the serum levels of some proteins such as procalcitonin (PCT), C-reactive protein (CRP) and interleukin 6 (IL-6)

fructuate as sepsis progresses, which can be used to identify at-risk patients.[124] Among them, IL-6 levels increase during the first hours of infection when PCT and CRP levels have not changed yet, making it a particularly useful biomarker for improving outcomes with an early diagnosis [125]. However, the detection of cytokines such as IL-6, which are found at average concentrations lower than 5.9 $pg \cdot mL^{-1}$ in healthy individuals, requires hour-long ELISA procedures that are too lengthy for early diagnosis schemes [126]. Automated immunoassay systems such as Elecsys® IL-6 can drastically reduce the assay time (18 min), but they are bulky, which makes them difficult to implement at some of the places where septic patients could be identified early on, such as the emergency room or an ambulance.

Biosensors are promising candidates for detecting IL-6 in the context of sepsis because they can potentially be deployed in a wide variety of clinical settings [127–129]. Indeed, several biosensors have already been proposed whose sensitivity is high enough for detecting clinically relevant concentrations of IL-6 under ideal conditions [130, 131]. Yet, many of these biosensors still require assay times longer than 30 min, and therefore they are not suitable for aiding clinical decision-making in emergency situations [91, 132]. Furthermore, the majority of these devices have only been tested in purified serum samples [133–136]. Remarkably, a lateral flow test has recently been proposed that can detect IL-6 in unprocessed blood with surface-enhanced Raman spectroscopy (SERS) [137]. Yet this test requires a microscope for detecting the biomarker at clinically relevant concentrations, which would be cumbersome to implement in bedside diagnosis. A commercial lateral flow immunoassay from Milenia Biotec can detect IL-6 in 20 min, but only at concentrations higher than 50 $pg \cdot mL^{-1}$. In the context of the current state of the art, a biosensor that could detect small variations in the blood levels of IL-6 in less than 20 minutes using portable, user-friendly instrumentation could have a great impact on sepsis care by enabling the identification of at-risk patients rapidly. Such a device could enable monitoring patients in many clinical settings where potential sepsis cases are managed, from primary care centers to ambulances and the emergency department, where it is imperative to identify signs of sepsis rapidly in order to prioritize patients effectively [138].

In this manuscript we describe a plasmonic mobile biosensor designed to meet the criteria for rapid IL-6 detection. Our biosensors reduce the assay time because they do not require purification or pretreatment of blood samples, and gold nanoparticles generate intense colorimetric signals with short incubation times. The device setup consists of a paper-based

biosensor paired with a smartphone app for colorimetric signal detection. Colorimetric signals are generated by gold nanoprobes modified with avidin and biotinylated antibodies (**Fig. 4.1** a). Since IL-6 is found at ultralow concentrations in healthy individuals, and its cut-off values indicating sepsis risk are not much higher (ca. 25 $pg \cdot mL^{-1}$ in newborns and 40-61 $pg \cdot mL^{-1}$ in adults),[139] great care was taken to optimize each step of the biosensor fabrication to detect the biomarker rapidly at clinically relevant concentrations in unprocessed blood. This included synthesizing nanoparticles through 3 different routes for obtaining nanoprobes using different bioconjugation strategies as well as testing several approaches for immobilizing biomolecules on paper substrates. The optimized nanoprobes and paper biosensors generated signals in the form of colored spots (**Fig. 4.1** a) whose pixel intensity was evaluated in real time with a custom designed companion app (**Fig. 4.1** b–d). Smartphone-based densitometry can be challenging for in-field measurements because it requires a specific positioning of the camera with respect to the assay while at the same time compensating for variations in the pixel intensity that did not originate from the biospecific recognition of the analyte [140, 141]. Our app uses an innovative augmented reality (AR) guidance system to guide the user to the correct positioning of the smartphone, while steps such as white balance calibration, light artifact detection, selection of a region of interest, measurement of pixel intensity, and data validation are automatically performed with real-time image processing and data processing. This means that the user only needs to hover the phone over the assay to obtain reliable densitometry readings within seconds. No cradles, light-tight boxes or special attachments are required to ensure robust measurements. The optimized plasmonic mobile biosensors were able to detect IL-6 with a limit of detection of 0.1 $pg \cdot mL^{-1}$ and a total assay time within 17 min. They were also able to detect IL-6 spiked into unprocessed blood with the same assay time at concentrations well below the cutoff values indicating sepsis. The rapid turnaround time, excellent sensitivity in blood matrices and high portability of the mobile detection scheme make our biosensors well suited for detecting IL-6 in decentralized healthcare schemes such as those involved in the management of potential sepsis cases.

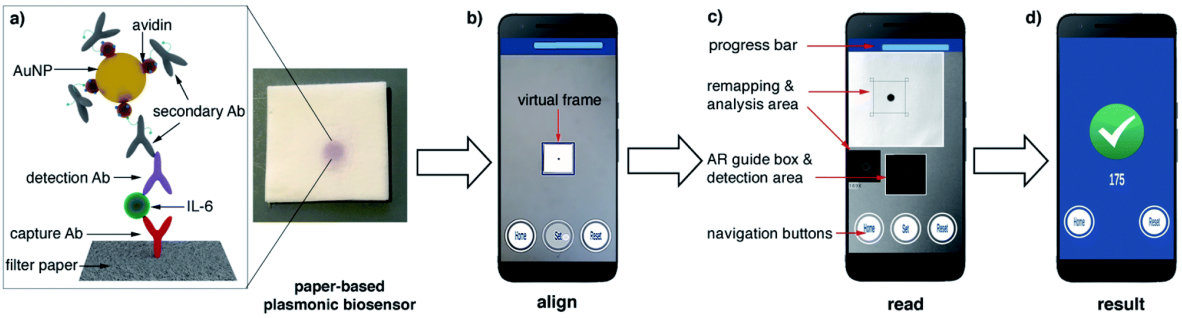

Fig. 4.1 *Schematic representation of the plasmonic mobile biosensors (a) antibody-decorated gold nanoparticles generate colored spots on paper substrates; (b) the color in the spots is quantified with an app that uses a virtual frame to control the angle and distance between the biosensor and the smartphone; (c) the detection screen appears after aligning the frame in the AR guidance system with the biosensor and pressing the Set button, and the app automatically detects the region of interest (ROI) while at the same time sampling background signals from 4 points around the ROI to avoid interference from uneven lighting* [142]. *(d) When the app has measured 50 valid points, the progress bar stops and the resulting increase in pixel intensity is displayed (see Video S4.1 in the supplementary information). Ab: antibody, IL-6: interleukin 6, AuNP: gold nanoparticle, and AR: augmented reality.*

4.2 Materials and methods

4.2.1 Materials

Poly(ethylene glycol) 2-mercaptoethyl ether acetic acid (SH-PEGCOOH, Mn 2100), poly(ethylene glycol) 2-mercaptoethyl ether ethylamine (SH-PEG-NH2, Mn 5000), avidin from egg white, 2- (N-morpholino)ethanesulfonic acid (MES), N-(3-dimethylaminopropyl)-N -ethylcarbodiimide hydrochloride (EDC), N-hydroxysulfosuccinimide sodium salt (sulfo-NHS), glutaraldehyde (25% in water), sodium cyanoborohydride (95%), poly(- sodium 4-styrenesulfonate) (PSS, 30% in water) and recombinant human interleukin 6 (IL-6) were purchased from Sigma. Poly(allylamine hydrochloride) (PAH) was obtained from Alfa Aesar and bovine serum albumin (BSA, protease free) was purchased from VWR. Phosphate buffered saline (PBS), PBS containing 5 mg·mL^{-1} BSA (PBS–BSA) and PBS containing 0.1% Tween-20 were prepared following standard procedures. Biotinylated proteins were obtained with an EZ-Link biotinylation kit from Thermo Fisher and purified with a PD-desalting column. Monoclonal anti-IL-6 developed in mice (ab11449), polyclonal anti-IL-6 developed in rabbits (ab6672) and antirabbit IgG (biotin) preadsorbed developed in donkeys (ab7082) were obtained from abcam.

4.2.2 Nanoprobe fabrication

Detailed protocols for obtaining nanoparticles with an initial coating of citrate, PAH or PVP molecules are available in appendix 1 Citrate-capped nanoparticles were modified with 0.1 mM SH-PEG-COOH overnight to obtain carboxylate-coated nanoparticles, whereas PAH-covered nanoparticles were modified with 0.1 mM SH-PEG-NH2 overnight in order to obtain

aminecoated nanoparticles [143]. PVP-coated nanoparticles were resuspended in water and used without further purification. Avidin attachment to carboxylate-coated nanoparticles proceeded as follows. Carboxylate-coated nanoparticles (250 mL) were concentrated to a final volume of 1 mL and washed 5 times with water with the aid of a centrifuge (9000 rpm, 8 min). Then carboxylate moieties were transformed into sulfo-NHS esters via addition of EDC (1 mg) and sulfo-NHS (2 mg) to the nanoparticle suspension in 0.5 M MES buffer of pH 6 (200 µL, [Au] =100 mM). After 30 min the nanoparticles were pelleted with a centrifuge and the supernatant was substituted with a solution containing avidin (200 µL, 0.1 $mg \cdot mL^{-1}$, overnight). The pH of the avidin solution was varied from 5.5 to 7.4 with phosphate buffer (0.1 M) to test the impact of this parameter on the reaction between the sulfo-NHS esters and amine groups in proteins. Then 400 µL of a blocking solution containing glycine (0.1 M) and BSA (10 $mg \cdot mL^{-1}$) in phosphate buffer (0.1 M, pH 7) was added for at least 30 min followed by washing 5 times with PBST.

Avidin was attached to amine-coated or PVP-coated nanoparticles using glutaraldehyde as a crosslinker with the following procedure [144]. First glutaraldehyde (334 µL, 7.5%) in 0.1 M bicarbonate buffer of pH 9 was added to the nanoparticle dispersion (166 µL, [Au]=100 mM) for different times. Excess reagents were removed with a PD-10 desalting column rather than by centrifugation in order to reduce covalent crosslinking between nanoparticles upon pellet formation. Nanoparticlerich fractions were identified by their characteristic reddish color. Then avidin (100 µL, 1 $mg \cdot mL^{-1}$) was added to the nanoparticles in the presence of NaCNBH3 (100 µL, 100 mM), which reduces the pH-sensitive imine bonds generated by the reaction between amines and aldehydes and yields stable amine bonds. After overnight incubation unreacted aldehydes were blocked with glutamic acid (0.1 M) in sodium bicarbonate (0.1 M, 100 µL) for 1 h. The resulting avidin-decorated nanoparticles were washed by centrifugation 5 times with PBST. Nanoparticle suspensions were characterized by transmission electronic microscopy (TEM) with a Hitachi H-600 ABS TEM (carboxylate- and anime-coated nanoparticles) and a JOEL 1011 TEM (PVP-coated nanoparticles) operating at 100 kV. Extinction spectra were taken with a DU 730 Beckman Coulter spectrophotometer. Zeta potential measurements were performed with a Nano Zetasizer (Malvern).

4.2.3 Nanoprobe performance

The performance of the avidin-decorated nanoprobes was tested with a model biosensor using paper substrates. The paper substrates were made of Whatman filter paper grade 41

cut into 2.5 x 10 cm pieces and folded like an accordion [20]. Biosensors were prepared with 3 different methods. The first method involved spotting biotin–BSA (5 µL, 0.1 mg·mL^{-1} in PBS) on the top paper layer at different concentrations for 5 min (direct adsorption). The second method involved spotting PAH (1% (w/v), 10 µL) and letting it dry (10 min) followed by spotting the protein at different concentrations, whereas the third method involved an additional PSS treatment (1%) after adding the protein followed by washing with water and letting the paper dry (10 min). Next the paper substrates were blocked with PBS–BSA (1 mL). Immediately afterwards avidin-decorated nanoparticles were spotted onto the substrate (2 µL, 4 min) followed by washing with PBST (1 mL, 3 times). Control experiments were performed in the same way but by using non-biotinylated BSA in order to assess the impact on non-specific interactions between the nanoparticles and the paper substrate. The biosensors were let to dry and the colorimetric signals were evaluated with ImageJ after scanning the samples with an MFC1910F Brother printer-scanner.

4.2.4 Development of an app for real-time densitometry

An Android app was developed on a Unity3D platform (version 2019.1.8) using OpenCV 4.0 APIs with a C# wrapper from Enox Software (OpenCVforUnity version 2.3.3) (see also **Table S1 appx 1**). It was tested on a Huawei POT-LX1 smartphone. The app was transferred to the smartphone via USB connection for debugging and final installation. An 18% standard neutral gray card from a JJC, model number GC-1II was used for camera calibration. Taking the laboratory-based scanner approach as a methodological starting point, we sought to approximate and automate the steps involved in image acquisition and subsequent image processing. A summary comparison of the procedural sequence of steps between these two methods can be found in **Table S2 appx 1** The source code showing the methods used to automate the image processing steps is available on Github (https://gist.github.com/SMR-83/ cdb16aaaf56a3b7c3ba7c02efd1a664b). A statistical analysis was programmed into the app to automatically evaluate the dataset based on a conditional statement in the code which caps the zscore of each data point at 1.5 standard deviations from the mean as the criteria for inclusion in the dataset. A data point with a z-score greater than 1.5 is considered an outlier, and the app is programmed to allow no more than 5 outliers out of 50 measurements for the dataset to be considered valid.

4.2.5 Detection of IL-6 with plasmonic paper-based biosensors

Biosensors for the detection of IL-6 were fabricated as follows. Avidin-nanoparticles (100 µL, [Au] 100 mM) were modified with biotinylated anti-rabbit IgG (10 µL) for 1 h followed by

washing 3 times with PBST with the aid of a centrifuge (7000 rpm, 5 min, final volume 25 µL). Capture antibodies (mouse monoclonal anti-IL-6) were immobilized by adding a drop on the paper substrate (2.5 µL, 10 mg·mL^{-1}) and letting it dry for at least 10 min. Then the biosensors were blocked with PBS–BSA (1 mL, let dry at room temperature for at least 10 min). To detect IL-6 the paper biosensors were rehydrated with 1 mL of PBS–BSA followed by the addition of IL-6 spiked at different concentrations in PBST, human serum or whole blood (2.5 µL). In order to ensure that the composition of the matrix was not noticeably altered by the spiking procedure, an IL-6 solution with a high concentration of 1 mg·mL^{-1} in PBS was serially diluted more than 10^4 times with whole serum or blood to yield samples in the concentration range between 50 and 3 pg·mL^{-1}. Blood samples were stored in tubes containing EDTA as the anticoagulant. After 5 min the biosensor was washed up to 4 times with PBST (1 mL). Then the detection antibody was added (2.5 µL, 10 mg·mL^{-1}) for 5 min and the biosensors were washed once with PBST. Finally, avidin-decorated nanoparticles modified with biotinylated anti-rabbit IgG were added (2 µL, [Au]=400 mM) for 5 min. Then the biosensors were washed 4 times with PBST (1 mL) and the colorimetric signals were evaluated with the mobile densitometry app.

4.3 Results and discussion

The gold nanoparticles used as starting materials for nanoprobe fabrication were obtained through the reduction of gold ions with either citrate, PAH or PVP molecules. Citrate- and PAH-covered nanoparticles were subsequently modified with SH-PEG-COOH and SH-PEG-NH2 in order to obtain stable carboxylate- and amine-coated nanoparticles, respectively. **Fig. 4.2** shows the extinction spectra and representative TEM images of the 3 types of nanoparticles. Nanoparticle sizes calculated from the TEM images were 45±5 (PVP-coated, (i)), 49±12 nm (carboxylate-coated, (ii)) and 46±10 nm (aminecoated, (iii)). PVP-coated nanoparticles show a narrower size distribution, as evidenced from TEM analysis and the narrower width of the extinction spectra in **Fig. 4.2**, because they were obtained with a seeded growth method. The LSPR of PVP-coated nanoparticles, which depends on their size as well as on the coating around them, is 528 nm, whereas nanoparticles coated with carboxylate and amine groups show LSPR centered around 530 and 533 nm, respectively.

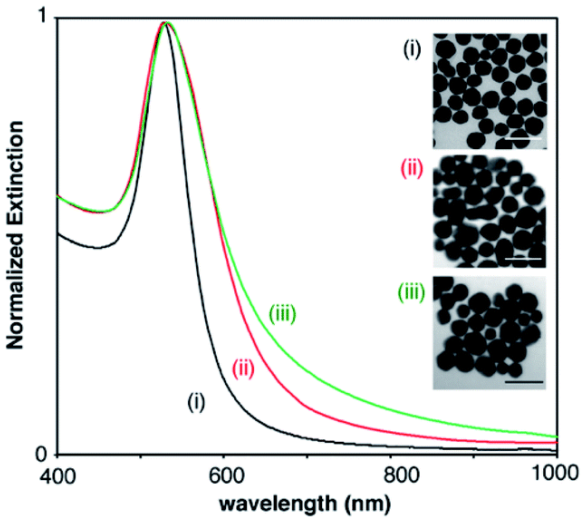

Fig. 4.2 *Extinction spectra and representative TEM images of the (i) PVP-coated, (ii) carboxylate-coated, and (iii) amine-coated nanoparticles used as starting materials for developing colorimetric nanoprobes. Scale bars: 100 nm.*

After characterizing the plasmonic nanoparticles we endeavored to optimize all the steps involved in the fabrication of the biosensor, from the covalent attachment of avidin to the nanoprobes to the immobilization of proteins on the paper substrate. Bioconjugation strategies involved amidation with carboxylate-coated nanoparticles or crosslinking with glutaraldehyde using amine- or PVP-coated nanoparticles (**Fig. 4.3**a). The amidation reaction involved transforming carboxylate groups into reactive sulfo-NHS esters followed by the addition of the protein. The key parameter to boost the yield of this reaction is the pH of the protein solution, since the reactivity of both the sulfo-NHS ester groups around the nanoparticles and the amines on the protein is pH-dependent [53]. Consequently, we prepared avidin-modified nanoparticles using protein solutions buffered at pH 5.5, 6.5 or 7.4 in order to discern the best conditions for obtaining nanoprobes. As shown in **Fig. 4.3**b, the resulting avidin-decorated nanoprobes were tested with a model biosensor for the detection of biotinylated proteins. As seen in this figure, the highest signals were obtained when the reaction between the sulfo-NHS ester and the protein was performed at pH 6.5. Lower signals for bioconjugation reactions at pH 5.5 and 7.4 are ascribed to lower reaction yields, either because protonated amines have poor reactivity (pH 5.5) or because the sulfo-NHS ester hydrolyzes before the reaction can take place (pH 7.4) [53]. Control biosensors containing non-biotinylated BSA always yield very low signals, which demonstrates that interactions with the paper substrates modified with biotinylated BSA are specific.

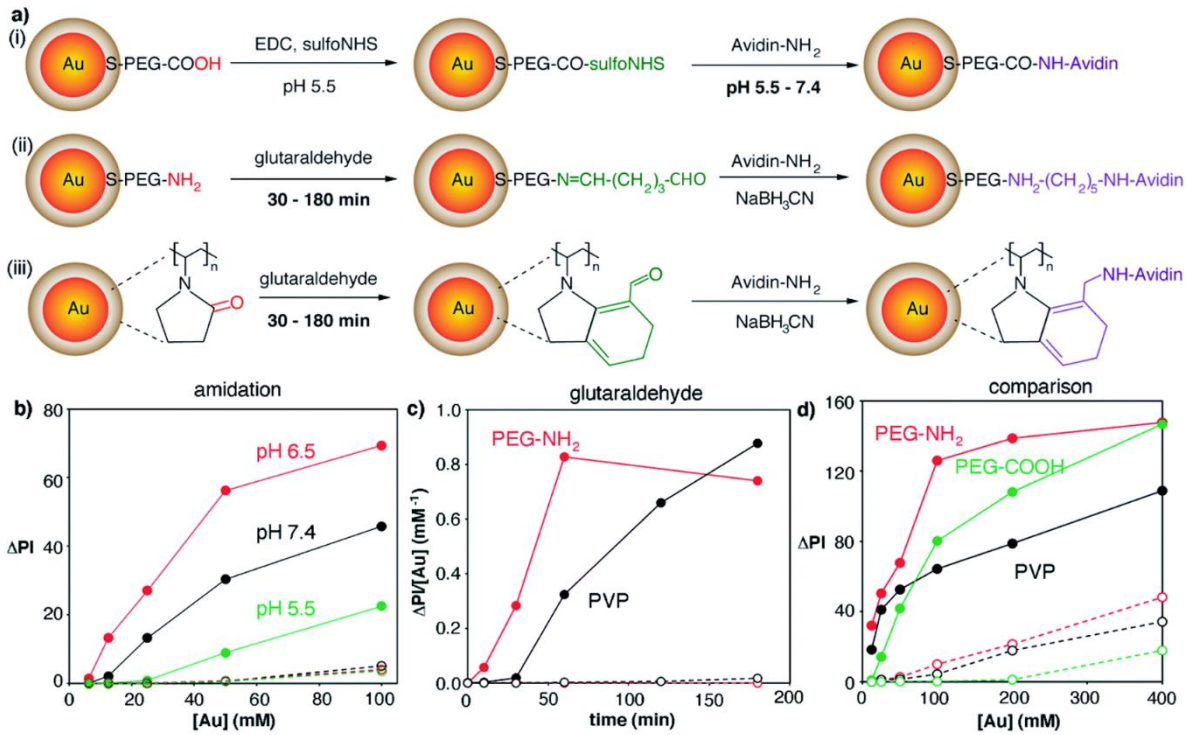

Fig. 4.3 *Bioconjugation reactions for binding avidin to gold nanoparticles; full dots indicate colorimetric signals generated by the biospecific reaction between avidin on the nanoparticles and biotin–BSA on paper substrates; open dots correspond to non-specific interactions with substrates modified with non-biotinylated BSA; (a) schematic representation of the reactions involved in the covalent attachment of avidin to nanoparticles; (b) effect of pH on amidation reactions (i); increase in pixel intensity (ΔPI) generated by avidin-decorated nanoparticles obtained by amidation in which avidin was added at pH 5.5 (green), 6.5 (red) or 7.4 (black); (c) effect of time on bioconjugation reactions using glutaraldehyde crosslinkers; ratio between ΔPI and nanoprobe concentration (ΔPI/[Au]) generated by avidin-decorated nanoparticles obtained after PVP-coated (black, (iii)) or amine-coated (red, (ii)) nanoparticles were reacted with glutaraldehyde for different times; (d) comparison of colorimetric signals (ΔPI) generated by the three types of gold nanoprobes as a function of the concentration ([Au]) of PVP-coated (black), carboxylate-coated (green) and amine-coated (red) gold nanoparticles.*

In the case of bioconjugation reactions using glutaraldehyde and amine- or PVP-coated nanoparticles (**Fig. 4.3**a), the reaction time with the cross-linker was deemed the most important parameter to be optimized. Since glutaraldehyde is a homobifunctional linker, extended incubation times could lead to nanoparticle agglomeration, whereas short incubation times could result in a low amount of proteins being bound to the nanoprobes. As shown in **Fig. 4.3**c (red dots), amine-coated nanoparticles yielded the highest signal per gold concentration when incubated with glutaraldehyde for 1 h, whereas PVP-coated nanoparticles required 3 h to yield the same result (black dots). Control experiments yielded very low signals which demonstrates that the color was mainly generated by biospecific biotin–avidin interactions.

After optimizing the bioconjugation reactions for the 3 proposed types of nanoparticles, the nanoprobes obtained under the best conditions were compared with each other in order to

determine which were most appropriate for fabricating our immunosensors. As shown in **Fig. 4.3**d, PVP-nanoparticles modified with avidin generated the least intense colorimetric signals (black dots). Amine-nanoparticles (red dots) generated higher signals than carboxylate-counterparts (green dots) when added at the same concentration. However, this increase in the signal originated from non-specific interactions, since higher signals were also observed in control experiments. We then hypothesized that the extent of both specific and non-specific interactions could change depending not only on the type of nanoprobe, but also on the strategy utilized to immobilize proteins on the paper substrate. To test this idea, we compared the signals generated via direct adsorption of biotinylated BSA on paper (**Fig. 4.3**d) with those obtained with biosensors fabricated with a modified cellulose matrix (**Fig. 4.4**).

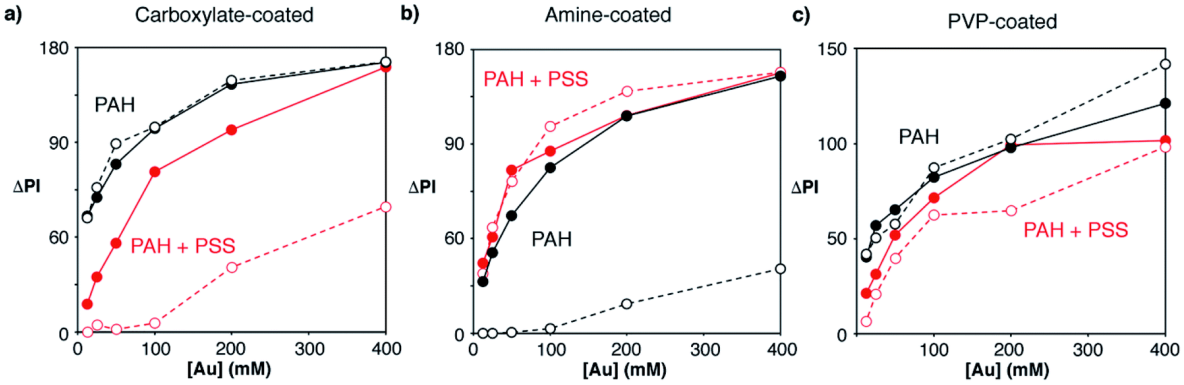

Fig. 4.4 *Colorimetric signals (ΔPI) generated by different concentrations of gold nanoprobes ([Au]) modified with avidin when the paper substrate was modified with PAH (black dots) or PAH and PSS (red dots), and biotinylated BSA (full dots) or non-biotinylated BSA (open dots). Nanoprobes modified with avidin were obtained using carboxylate-coated (a), amine-coated (b) or PVP-coated (c) nanoparticles.*

The paper modifications entailed adding a positively charged polymer PAH, either alone or followed by the addition of negatively charged PSS. These treatments were chosen to evaluate the role of the paper surface charge in both attaching capture biomolecules and establishing non-specific interactions with the nanoparticles, which have different surface charges according to their coatings (zeta potential -2.7, 1.7 and -1.5 mV for carboxylate-, amine-, and PVP-coated nanoparticles modified with avidin, respectively). Experiments with another positively charged polymer (chitosan) were also attempted, but they were discarded because it blocked the pores of the paper, making it difficult to perform washing steps. Similarly, attempts at modifying PAH-modified paper substrates with glutaraldehyde for covalent attachment of proteins were rejected because they resulted in yellow coloration of the filter paper that interfered with colorimetric measurements even after reducing imines with NaCNBH3. **Fig. 4.4** shows the colorimetric signals obtained when biotinylated-BSA was

physically adsorbed on PAH-modified paper (black dots) or PAH and PSS (red dots). As shown in **Fig. 4.4** a) carboxylate-coated nanoparticles modified with avidin generated high non-specific signals when the cellulose matrix was modified with PAH only, but the extent of non-specific interactions decreased upon addition of PSS. This is in agreement with the negative zeta potential value of the nanoparticles, which results in non-specific electrostatic interactions with the matrix covered with positively charged PAH. As seen in **Fig. 4.4** b) amine-coated nanoparticles show the opposite behavior, that is, high non-specific signals are generated when the matrix is negatively charged through the modification with PSS. PVP-coated nanoparticles yielded non-specific signals in all cases (**Fig. 4.4** c), and therefore were discarded from further appraisal. Comparison of the specific signals obtained under the best conditions revealed that biosensors combining carboxylate-coated nanoparticles and unmodified paper substrates, or amine-coated nanoparticles and cellulose modified with PAH, were best suited for colorimetric detection (**Fig S2 appx 1**). The first design was chosen for further studies to expedite the fabrication process and reduce manufacturing costs, since it does not require modification of the paper substrate.

After optimizing the fabrication of the biosensor we sought to determine the best conditions for detecting IL-6. This included optimizing the concentration of capture and detection antibodies, as well as the time required to capture IL-6 (**Fig S3 appx 1**). Antibody-decorated nanoparticles were obtained by adding biotinylated antibodies to the avidin-modified nanoparticles. From these optimization experiments it was determined that the best conditions for detecting IL-6 were to spot the capture antibody on the paper substrate at a concentration of 10 $\mu g \cdot mL^{-1}$, and to add the detection antibody at a concentration of 10 $\mu g \cdot mL^{-1}$ for 5 min (**Fig S3 appx 1**). The total assay time, including washing steps, was under 17 minutes. Under these conditions, recombinant human IL-6 was detected in buffered solutions in the concentration range between 0.001 and 10 $pg \cdot mL^{-1}$ (**Fig. 4.5**, $y=8x + 25$, $r^2=0.95$). Experiments performed with control biosensors without the capture antibody yielded lower signals, which indicates that the main contribution to the colorimetric output is the biospecific recognition of IL-6 by the antibodies. The limit of detection, expressed as the concentration of the first sample that yields a signal higher than 3 times the standard deviation of the blank, is 0.1 $pg \cdot mL^{-1}$. This limit of detection is much lower than the reported threshold value indicating sepsis, which makes the optimized biosensor a promising technology for the detection of elevated levels of IL-6 in real matrices as detailed below.

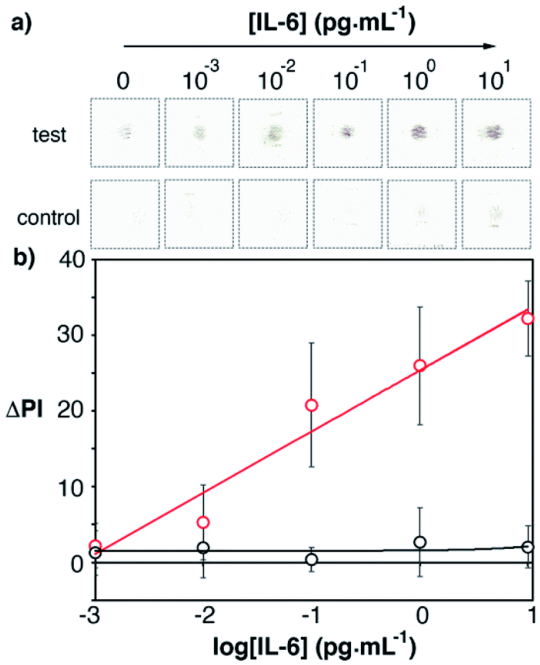

Fig. 4.5 *Scanned images (a) and the calibration plot (b) for detecting recombinant IL-6 in PBS with the proposed immunosensors (red dots) and control biosensors without the capture antibody (black dots). [Au] = 400 mM. The total assay time was under 17 min. Error bars are the standard deviation (n = 3).*

Detecting IL-6 in the context of sepsis at the point of care necessitates the use of unprocessed blood and a portable readout instrument capable of yielding robust results in different locations with varying environmental conditions. The latter was achieved here with a mobile app for performing reliable densitometry at the point of care that only requires hovering a smartphone over the assay in order to quantify colorimetric signals (Video S4.1). The app was calibrated using pieces of paper modified with nanoparticle drops at different concentrations, and therefore with different pixel intensities. The calibration was repeated under 3 different room illuminance conditions (200, 570 and 1070 lux) and compared with the same measurements obtained using a desktop scanner and manual image processing with Image J. As shown in **Fig. 4.6**, the room illuminance has very little effect on the app performance (coefficient of variation CV 1.7% for [Au]=12.5 mM). The main difference with the scanner method is that the app yields slightly lower signals when the nanoparticles are spotted at low concentrations. This is attributed to the shorter distance between the assay and the camera in the scanner compared to the smartphone-based approach. These results demonstrate that the proposed app can yield consistent results without using any hardware accessories attached to the smartphone to control imaging conditions, which makes it more economical, portable and hygienic for medical diagnostics [145].

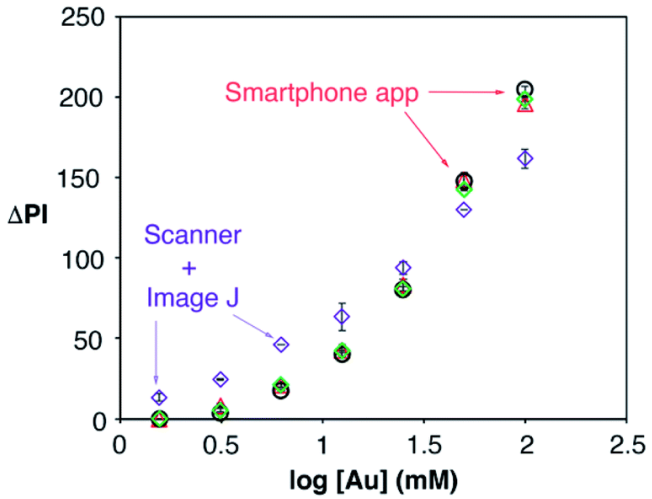

Fig. 4.6 *Calibration plot obtained by evaluating the colorimetric signal generated by gold nanoparticles at different concentrations with the densitometry app when the room illuminance was 200 (black dots), 570 (green diamonds) and 1070 lux (red triangles), and with a desktop scanner (purple diamonds); error bars are the standard deviation (n = 3).*

Next we tested whether we could detect elevated levels of IL-6 by combining the app with the optimized paper biosensors. Blood samples from a healthy donor were spiked with recombinant IL-6 and analyzed with our 17 min-long method and real-time densitometry with the mobile app. The characteristic red color of whole blood was efficiently removed with the proposed washing procedure and therefore was not an impediment to perform the assay (**Fig S4 appx 1**). Since healthy individuals have non-negligible levels of IL-6 (<5.9 pg·mL-1), we sought to determine which was the lowest added concentration of IL-6 that could be detected above basal levels with 99% confidence (i.e. above 3 times the standard deviation of the blank (s), which contains basal levels of IL-6). As can be seen in **Fig. 4.7**, control experiments yielded a residual signal due to a small contribution from the color of the sample (**Fig S4 appx 1**). and non-specific interactions with the whole blood matrix. Experiments with spiked samples yielded higher dose-dependent signals, which demonstrates that the nanoparticles are being anchored to the substrate through specific antibody–antigen interactions. Samples spiked with 12.5 pg·mL^{-1} yielded a signal higher than 3s. This number is lower than the threshold value indicating sepsis in newborns or adults, which means that our biosensors are suitable for detecting small variations in IL-6 observed in the early stages of sepsis. This, along with the short assay time and robust signal reading afforded by the smartphone app, makes the proposed mobile biosensors ideal for supporting a biomarker-based diagnosis of sepsis in each of the clinical contexts along the chain of care.

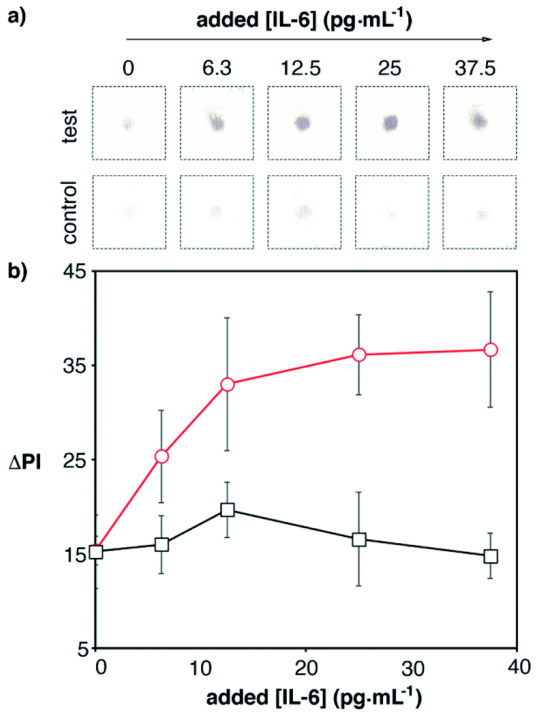

Fig. 4.7 *Detection of IL-6 spiked into human blood with plasmonic mobile biosensors; (a) images of colored spots; (b) signal quantification with the smartphone app. Control experiments were performed with biosensors that were not modified with capture antibodies (black squares). The total assay time was under 17 min (**Table S3 appx 1**). Error bars are the standard deviation (n = 3).*

4.4 Conclusions

In this manuscript we have reported the fabrication and performance of a plasmonic immunosensor for the rapid detection of IL-6 in the context of sepsis. Key aspects of the immunosensor fabrication, including the manufacture of plasmonic nanoprobes decorated with proteins and strategies for attaching capture molecules to the paper substrate, were optimized. We have also introduced a companion app that quantifies the colorimetric signal generated by the plasmonic probe in real time. Our app is unique in that it does not require hardware attachments added to the smartphone in order to stabilize angle and distance parameters; instead it makes use of a software-based AR guidance system. The optimized paper biosensors were able to detect IL-6 under ideal conditions with a low limit of detection of 0.1 pg·mL^{-1} within 17 min. When the biomarker was spiked into serum or blood, the biosensors were able to detect variations in the basal concentration of IL-6 as small as 12.5 pg·mL^{-1} with 99% confidence. The ability to detect small variations in cytokine levels in unprocessed blood using only a paper biosensor and an unmodified smartphone makes the proposed detection scheme ideal to support evidence-based clinical decision-making. In the context of sepsis, it would enable the measurement of biomarkers during triage, when

prioritizing high-risk patients is essential for improving sepsis outcomes [138],[146]. Moreover, the biosensors only require a tiny sample volume (2.5 µL), which makes them suitable for sepsis screening in neonates as well [81]. Furthermore, the same strategy could be used to detect other biomarkers [36] and pathogens [147] by using specific antibodies against them.

5 NANOPARTICLE RESERVOIRS FOR PAPER-ONLY IMMUNOSENSORS

5.1 Abstract

Biosensors made entirely of paper are becoming increasingly popular due to their low cost, facile fabrication, and lightweight portability for in-field measurements. However, it is difficult to store nanoparticles in paper substrates without irreversibly binding them to the cellulose matrix. This makes it challenging to fabricate biosensors incorporating nanoparticle probes in paper-based reservoirs. Here, we overcome this limitation with a new method for storing protein-decorated nanoparticles on paper substrates that also allows to release them on demand. It consists of spotting nanoparticles onto pieces of filter paper previously modified with polystyrene sulfonate. Gold nanoparticles modified with avidin or antibodies can be easily transferred from the dry reservoir to a receiving wet piece of paper by simply pressing with the finger or a clamp. Paper-based immunosensors incorporating the reservoir enabled the detection of glycoprotein B from human cytomegalovirus in serum with a limit of detection of 0.03 $ng \cdot mL^{-1}$ and a total assay time of only 12 min. The low limit of detection obtained with a short assay time along with the long shelf-life of the reservoirs make the proposed paper-only biosensors ideal of point-of-care diagnostics.

5.2 Introduction

Filter paper is becoming a popular substrate for developing disposable biosensors because of its lightweight, low price, and easy disposal [148–150]. It is commercially available in a wide array of pore sizes and can be easily modified with biomolecules following physical adsorption or covalent attachment methods [151, 152]. Its porous matrix can also be used to store reagents such as enzymes and their substrates in order to fabricate reservoirs integrated into paper-based analytical devices [153]. Such reservoirs must preserve the physicochemical properties of the constituent reagents over time while also ensuring an efficient release of their contents to other paper areas upon addition of liquid. Plasmonic nanoparticles are extremely useful building blocks for the fabrication of biosensors using a wide array of signal transduction mechanisms, from colorimetry [154] and surface-enhanced Raman spectroscopy [155] to fluorimetry [156] and electrochemistry. [157] However, plasmonic nanoparticles tend to adsorb irreversibly to paper substrates after drying, which makes it difficult to store them in reservoirs made of this material [158]. Traditionally, this

issue has been overcome by making reservoirs out of glass fiber rather than conventional paper. [159] However, this approach is not fully compatible with biosensor designs such as origami paper-based analytical devices. These biosensors are meant to be entirely made of paper with the purpose of simplifying their fabrication and facilitating the contact between the parts without the use of additional adhesives [41, 160, 161]. Therefore, it would be desirable to find a method for storing nanoparticles on paper substrates so that they could be implemented in paper-only 3D analytical devices.

In this manuscript, we introduce a new approach for fabricating nanoparticle reservoirs on filter paper. It consists of modifying the paper substrates with the negatively charged polymer polystyrene sulfonate (PSS) in order to avoid the irreversible binding of gold nanoparticles to the cellulose matrix (**Fig. 5.1**A). Reservoirs prepared this way can release nanoparticles with high efficiency. PSS has been previously used in order to avoid nanoparticle flocculation, usually in the form of alternating layers of PSS and a positively charged polymer such as polydiallyldimethylammonium chloride [162]. It has also been used as a support for growing nanoparticles [163] and for transferring them to a receiving substrate with soft lithography [164]. PSS blended with poly(3,4-ethylenedioxythiophene) is routinely used in order to modify cellulose and render it conductive [165]. In our approach we report a novel use for PSS to avoid the irreversible binding of nanoparticles to cellulose matrices. Besides enabling the release of nanoparticles from cellulose on demand, PSS also makes it possible to transfer nanoparticles from the dry reservoir to a receiving wet paper substrate by simply pressing the former against the latter (**Fig. 5.1**B). This makes the proposed reservoirs useful for developing biosensors with simplified liquid handling schemes because there is no need to add a controlled volume of buffer to the reservoir in order to transfer its contents to a detection area. Furthermore, nanoparticles modified with a protein (avidin, antibodies) retain their ability to specifically recognize their target ligand (biotin, antigens) immobilized on the receiving piece of paper in a dose-dependent manner, which demonstrates the suitability of our approach for developing biosensors (**Fig. 5.1**C). Vertical transfer between different layers of paper happens efficiently with limited horizontal diffusion without the requirement of hydrophobic barriers [166] or extra additives [151]. This generates intense colorimetric signals due to the biospecific binding of gold nanoparticles to the receiving paper substrate. Our method is an alternative to previously proposed paper-based reservoirs that contained nanoparticles suspended in sucrose-supplemented buffers. The release of nanoparticles from such reservoirs has not been characterized in full, [167] and in some cases, it has been reported to be highly inefficient [158]. The reservoirs proposed here are easy to fabricate,

have a long shelf life, and avoid common pitfalls associated to paper biosensors such as the generation of patchy colorimetric signals. The proposed nanoparticle reservoirs were incorporated into immunosensors for the detection of human cytomegalovirus (CMV) in order to demonstrate their suitability for developing biosensors made entirely of filter paper. Our biosensors were able to detect a key antigen of the virus [glycoprotein B (gB) antigen] spiked into serum with a limit of detection of 0.03 ng·mL^{-1} and a rapid assay time within 12 min. To the best of our knowledge this is the lowest limit of detection reported for this analyte thus far, and in a matrix as complex as human serum [168–170].

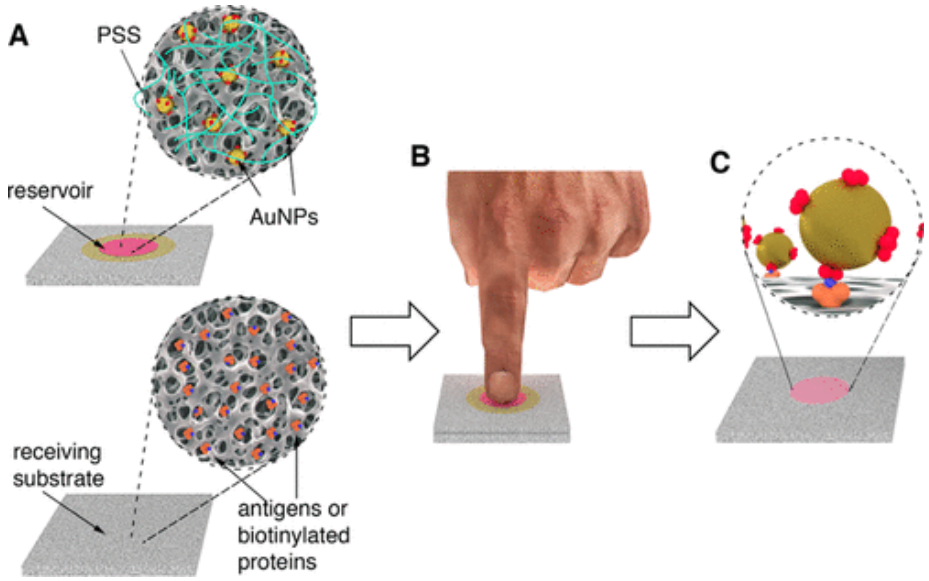

Fig. 5.1 *Schematic representation of the paper-based nanoparticle reservoirs and their utilization in biosensing; (A) reservoirs consist of pieces of filter paper modified with PSS and protein-decorated nanoparticles, the receiving paper substrate contains antigens or biotinylated proteins; (B) pressing the dry reservoir onto the wet receiving substrate triggers the transfer of nanoparticles from the former to the latter; (C) the nanoparticles establish biospecific interactions with antigens or biotinylated proteins bound to the receiving paper substrate.*

5.3 Materials and methods

5.3.1 Fabrication of Gold Nanoprobes

Citrate-capped gold nanoparticles with a diameter of ca. 40 nm were synthesized with the Turkevich method as previously described. [147] The nanoparticles were then modified with 0.1 mM thiolated polyethylene glycol (PEG) molecules ending in carboxylate moieties [poly(ethylene glycol) 2-mercaptoethyl ether acetic acid, Mn 2100, Sigma] overnight. The resulting pegylated nanoparticles were concentrated and washed with water five times via centrifugation at 8000 rpm for 6 min. The nanoparticles were finally suspended in 0.5 M 2-(*N*-morpholino)ethanesulfonic acid (Sigma) adjusted at pH 5.5. Carboxylate moieties around the nanoparticles were then transformed into sulfo-NHS esters by adding 1 mg of *N*-(3-dimethylaminopropyl)-*N′*-ethylcarbodiimide hydrochloride (Sigma) and 2 mg of *N*-

hydroxysulfosuccinimide sodium salt (sulfo-NHS, Sigma) for 20 min. Then, the nanoparticles were pelleted by centrifugation, and the supernatant was substituted for a solution containing 1 mg·mL^{-1} avidin in 0.1 M phosphate buffer pH 7.4. After 1 h, unreacted sulfo-NHS esters were capped with 0.1 M glycine and 10 mg·mL^{-1} bovine serum albumin (BSA) for 30 min. The nanoparticles were then washed five times with phosphate buffer saline (PBS) containing 0.1% Tween-20 (PBST). The resulting avidin-covered nanoparticles were kept at 4 °C until used.

5.3.2 Densitometry

Gold nanoparticles on paper substrates generate concentration-dependent colorimetric signals that can be evaluated with densitometry as follows. First, the paper substrates were scanned with an MFC-1910W scanner-printer (Brother). Pixel intensity (PI) profiles were obtained with ImageJ. In grayscale, pure white yields a 255-pixel intensity, whereas pure black yields a 0 pixel intensity. The colorimetric signal S was obtained as follows: First, the pixel intensity in grayscale was measured in a circular area within the area of interest with the Histogram function of ImageJ. The colorimetric signal S was taken as the integer value after subtracting the background signal. Please note that subtracting the background pixel intensity yields inverted signals compared to the raw data.

5.3.3 Fabrication of Nanoparticle Reservoirs

Whatman filter paper number 41, 1, and 6 (pore diameters of 20–25, 11, and 3 µm, respectively) was used. The paper was cut in squares and modified with 50 µL of PSS (30%, Sigma) diluted to different % (v/v) with water when required. After drying, 1 µL of pegylated gold nanoparticles modified with avidin was added and left to dry at room temperature. To study the release of nanoparticles from reservoirs, the nanoparticle-modified dry paper substrates were positioned on top of a folded piece of filter paper and 1 mL of PBST was added three times. The presence of nanoparticles after this step was evaluated by letting the paper dry and measuring any changes in the color of the nanoparticle reservoir with densitometry.

5.3.4 Nanoparticle Transfer and Biorecognition

The transfer of nanoparticles from the reservoir to a receiving paper substrate was studied with the following procedure. Receiving paper substrates were modified with 2 µL of biotinylated BSA (100 µg·mL^{-1} in PBS). Biotinylated BSA was obtained with an EZ-Link sulfo-NHS-biotinylation kit (Thermo Scientific). Control experiments with non-biotinylated BSA were performed in order to assess the contribution of nonspecific interactions to the

colorimetric signal. After drying, 1 mL of PBS-BSA (PBS supplemented with 5 mg·mL^{-1} BSA) was added. Then, the reservoir was placed on top of the wet receiving paper and nanoparticle transfer was facilitated by pressing in the center of the spot for 4 min. Subsequently, the reservoir was removed, and the receiving substrate was washed three times with PBST in order to remove nonspecific interactions. After drying, the colorimetric signal was evaluated with densitometry as detailed above.

5.3.5 Detection of gB from CMV

Monoclonal mouse anti-gB (Abcam, ab6499) was biotinylated with an EZ-Link sulfo-NHS-biotinylation kit (Thermo Scientific). Avidin-decorated nanoparticles (100 µL, 72 nM) were incubated with 10 µL of biotinlylated anti-gB for 1 h. After washing three times with PBST, 1 µL of the nanoparticle suspension (140 nM) was spotted on the paper reservoir modified with 30% PSS. The capture antibody (mouse monoclonal anti-gB Abcam ab54023) was spotted on the receiving paper substrate (2.5 µL, diluted 1:100 in PBS) and left to dry at room temperature. Control biosensors were prepared in the same way with anti-*Escherichia coli* (Invitrogen PA1-7213), which does not recognize gB specifically. The resulting paper biosensors were blocked by adding 1 mL of PBS–BSA and letting it dry. To calibrate the biosensors, recombinant gB was spiked into human serum at different final concentrations. After rehydrating the biosensors with 1 mL of PBS–BSA, 50 µL of the spiked serum samples was added to the receiving paper substrate for 5 min. After washing once with PBST, the reservoir containing nanoparticles decorated with anti-gB was pressed onto the receiving paper with a clamp for 5 min (a photograph of the clamp is available in **Fig S5 appx 2**. After 5 min, the reservoir was peeled off and the receiving paper was washed four times with PBST. The colorimetric signal was measured immediately afterward with densitometry as explained above.

5.4 Results and Discussion

In our hypothesis, the modification of paper substrates with PSS facilitates storing nanoparticles in the cellulose matrix while at the same time enabling their release with a high efficiency. This is based on previous studies using PSS to prevent the aggregation of gold nanoparticles via nonspecific interactions [162]. To study this, filter paper was cut in squares, and then, 50 µL of PSS at different % (v/v) was added and left to dry. Three types of paper with different pore sizes (22, 11, and 3 µm) were studied. After drying, substrates with a pore size of 11 and 3 µm were discarded because they were heavily warped and the PSS was unevenly distributed (**Fig S1 appx 2**). Paper substrates with a pore size of 22 µm

(Whatman #41) remained mostly flat at all PSS concentrations and therefore were subsequently used for the fabrication of nanoparticle reservoirs. They were obtained by pipetting 1 μL of gold nanoparticles in the center of the PSS-modified paper and letting it dry at room temperature. The most widely available gold nanoparticle suspensions are synthesized following the Turkevich method, which renders them capped with negatively charged citrate molecules. To avoid nanoparticle aggregation in solutions containing highly concentrated cations or proteins, citrate molecules are often substituted for thiolated PEG ligands [171]. This not only prevents nanoparticle aggregation but also enables introducing reactive groups such as carboxylate moieties for further covalent attachment with biomolecules. With this in mind, we studied the fabrication of reservoirs containing pegylated nanoparticle probes modified with avidin via amide bond formation.

Fig. 5.2 A (top row, “before”) shows pictures of nanoparticle reservoirs prepared with different % PSS and 72 nM gold nanoparticles modified with avidin. In these images, the spot diameter tends to decrease as the % PSS in the paper increases. Concomitantly, the color intensity increases as the % PSS increases. This can also be observed in the pixel intensity profiles obtained from these images in **Fig. 5.2** B. In grayscale, the pixel intensity is the highest when the color is white (255) and the lowest when the color is black (0). In **Fig. 5.2** B, the pixel intensity across the reservoir decreases as the % PSS increases. The spot diameter follows the same trend. This indicates that the nanoparticles are found at higher concentrations and within a smaller volume of the paper matrix as the % PSS increases. We propose that the formation of these smaller and more concentrated nanoparticle reservoirs is related to a slower diffusion of the nanoparticles within the cellulose matrix. It is well established that the viscosity of a solution increases as the concentration of PSS increases [172]. Because the diffusion coefficient is inversely proportional to the viscosity according to the Stokes–Einstein equation, highly concentrated PSS reduces radial diffusion and results in smaller spots containing nanoparticles at a higher concentration. Please note that, although PSS gives a yellowish color to the paper substrate, its contribution to the pixel intensity cannot fully account for the changes in color observed within the reservoir. For example, in **Fig. 5.2** B, the pixel intensity outside the nanoparticle area decreases from 254 to 234 due to the modification with 30% PSS, but it decreases much more in the center of the reservoir, where the nanoparticles are found (PI ≈ 62). This means that the main contribution to the observed changes in color is a higher concentration of nanoparticles in the reservoir and not the addition of the PSS. In **Fig. 5.2** B, it is also noticeable that the pixel intensity is lower at the edge of the reservoir than in the center. This is attributed to a higher

concentration of nanoparticles at the edge of the spots due to an uneven distribution of solutes during the drying procedure (the so-called “coffee-ring effect”) [173]. Finally, we sought to determine whether the nanoparticles could be released efficiently from the reservoir, which is an important requirement for integrating reservoirs in biosensors. To this end, 1 mL of PBST was added three times to the reservoirs.

Fig. 5.2 A (bottom row, after), the color does not change in reservoirs prepared in the absence of PSS, showing that without the polymer, the nanoparticles are irreversibly bound to the cellulose matrix. However, as the % PSS increases, the color within the spot progressively disappears, which indicates that the nanoparticles exit the reservoir more efficiently when the % PSS in the reservoir is higher. These experiments demonstrate that PSS prevents the formation of irreversible interactions between the nanoparticles and the paper matrix. In **Fig. 5.2** C, signal quantification with densitometry shows that no color remains in the reservoir when the % PSS utilized to fabricate the reservoir is 15% or higher, which suggests a complete release of avidin-modified nanoparticles under this condition. All in all, the results shown in **Fig. 5.2** demonstrate that it is possible to store pegylated nanoparticles modified with proteins in a dry piece of paper previously modified with PSS and that the nanoparticles can be released on demand by simply adding an aqueous solution.

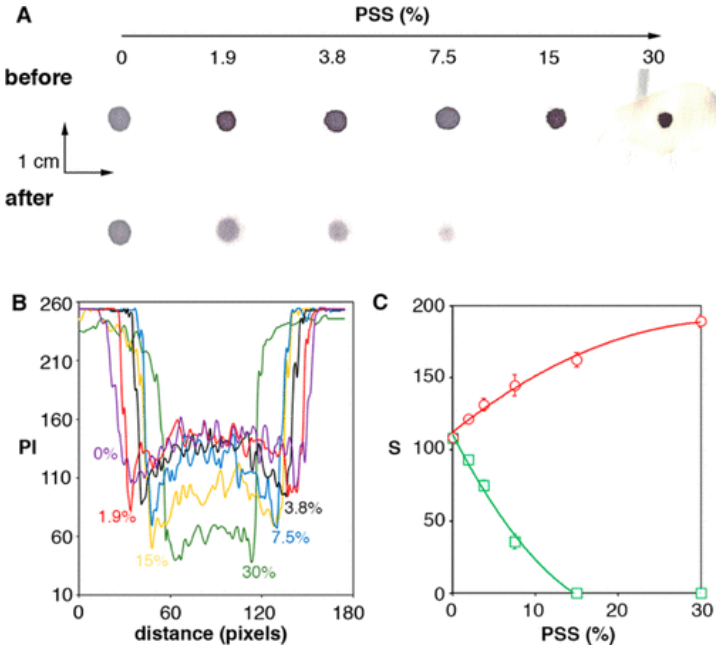

Fig. 5.2 *Fabrication of nanoparticle reservoirs with different % PSS; (A) scanned images of the reservoirs before (top row) and after (bottom row) washing three times with 1 mL PBST; (B) pixel intensity (PI) profiles across the reservoirs; (C) colorimetric signal (S) in the reservoir before (red circles) and after (green squares) washing three times with PBST. Error bars are the standard deviation (n = 3). Trend lines are a guide to the eye.*

Next, we investigated the impact of nanoparticle concentration in the fabrication of a paper-based reservoir containing avidin-modified gold nanoparticles. To this end, 1 μL of nanoparticles at different concentrations were pipetted onto paper substrates modified with 30% PSS (**Fig. 5.3** A). Profile analysis reveals that the formation of a “coffee ring” in the reservoir observed in **Fig. 5.2** can be prevented when nanoparticles are dispensed with a concentration of 140 nM or higher because under this condition, the pixel intensity is the same in the center and at the edge of the spot (**Fig. 5.3** B). It has been proposed that increasing the viscosity of the solution suppresses the formation of coffee rings [174]. In the case under study, the viscosity of the solution increases as the solid volume fraction increases in agreement with the Einstein **Eq 5.1**.

$$\eta = \eta_0 \left(1 + \frac{5}{2}\varphi\right)$$

Eq 5.1 *Einstein equation.*

where η is the viscosity of the suspension, η_0 is the viscosity of the dispersion medium, and φ is the solid volume fraction. Therefore, we propose that the increase in viscosity afforded by the higher nanoparticle concentration is a driving force to prevent coffee rings. To study the effect of nanoparticle concentration in the release of contents from the PSS-modified cellulose matrix, the reservoirs were washed with PBST as above and the remaining colorimetric signal was measured with densitometry. In **Fig. 5.3** A, low row (after) and **Fig. 5.3** C, the remaining colorimetric signal is very low at all the concentration assayed. Only a slight increase in color can be detected at the highest assayed concentration of nanoparticles. This indicates that 30% PSS is effective at preventing irreversible interactions with the paper even when the reservoirs contain a high concentration of gold nanoparticles. In summary, experiments in **Fig. 5.3** indicate that the best fabrication parameters for obtaining reservoirs with the proposed method are 30% PSS and gold nanoparticles with a concentration of 140–210 nM. Under these conditions, nanoparticles within the reservoir are evenly distributed (i.e., there is no coffee ring) and there is a complete release of colloids from the reservoir (no color remains in the paper reservoir).

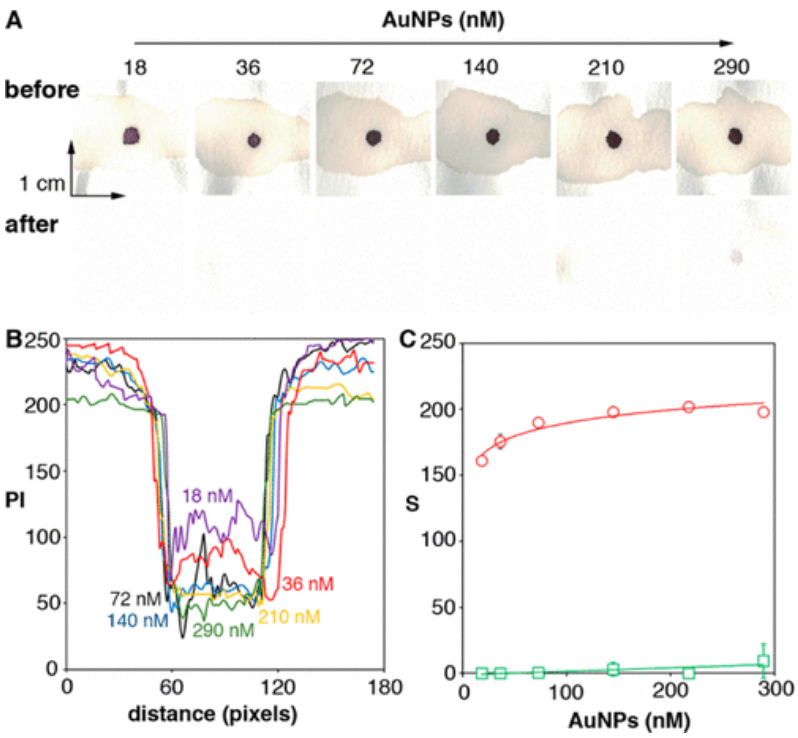

Fig. 5.3 *Fabrication of reservoirs with 30% PSS and avidin-decorated nanoparticles at different concentrations; (A) scanned images of the reservoirs before (top row) and after (bottom row) washing three times with 1 mL PBST; (B) pixel intensity (PI) profiles across the reservoirs; (C) colorimetric signal (S) in the reservoir before (red circles) and after (green squares) washing three times with PBST. Error bars are the standard deviation (n = 3). Trend lines are a guide to the eye.*

After studying the best conditions for storing and releasing nanoparticles in cellulose, we tested the ability of transferring the colloids in the dry reservoir to a receiving wet paper by pressing the former onto the latter (**Fig. 5.1**B). Simultaneously, we tested whether the avidin around the nanoparticles was still able to bind biotinylated molecules in the receiving substrate. In other words, we sought to investigate whether the presence of PSS interfered with our model biological interaction. To carry out this investigation, the dry reservoirs were pressed against a receiving paper substrate modified with biotinylated BSA and saturated with PBST. This transferred liquid from the wet receiving paper to the dry paper reservoir. The resulting rehydration of the reservoir allowed the nanoparticles to be transferred from the reservoir to the receiving substrate. After peeling off the reservoir, the presence of nanoparticles bound to the receiving paper substrate through avidin–biotin interactions was evaluated after washing it three times with PBST. **Fig. 5.4**A shows images of the receiving substrate when the reservoir was made with the same concentration of nanoparticles (72 nM) and different % PSS. In these images, the color in the spot is more homogenously distributed and intense as the % PSS increases. Indeed, at low % PSS, only a nanoparticle ring is generated, which progressively fills up to yield a colored spot at high % PSS. **Fig.**

5.4B also shows that avidin-decorated nanoparticles tend to accumulate in the periphery of the receiving spot when the concentration of PSS is low. As the % PSS increases, the diameter of the nanoparticle ring decreases and more nanoparticles are observed in the center of the spot. In **Fig. 5.4**C, the colorimetric signal increases as the % PSS increases because more nanoparticles are transferred within the region of interest. The formation of a ring made of biotin–BSA was ruled out it the experiment shown in **Fig S3 appx 2**, which indicates that the ring is originated by the transfer of the nanoparticles from the reservoir.

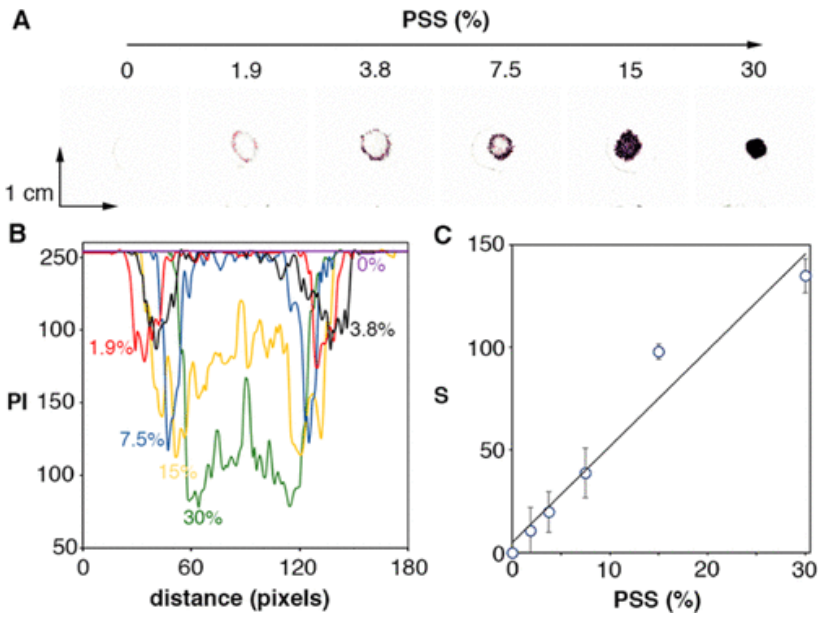

Fig. 5.4 *Transfer of avidin-decorated nanoparticles from the reservoirs with different % PSS to receiving substrates modified with biotinylated proteins; (A) scanned images of the receiving substrates after pressing the reservoirs for 4 min, removing them, and washing three times with 1 mL PBST; (B) pixel intensity (PI) profiles across the receiving substrate; (C) colorimetric signal (S) in the receiving paper substrate. Error bars are the standard deviation (n = 3). Trend lines are a guide to the eye.*

We propose two mechanisms for nanoparticle transfer that could result in the formation of a ring. The first mechanism implies that at a low % PSS, nanoparticles diffuse radially and accumulate at the edges upon being transferred, whereas at high % PSS, the nanoparticles diffuse radially to a lesser extent and are transferred homogenously to the receiving paper. This would result in more concentrated nanoparticles in the center of the spot as the % PSS increases, in agreement with the observations in **Fig. 5.4**. In the second hypothesis, nanoparticles are transferred preferentially from the edges of the reservoir to the receiving paper substrate, that is, a ring is first generated which subsequently fills up with more nanoparticles. To discern which mechanism governs nanoparticle transfer from the reservoir to the receiving paper, the same experiments were repeated with reservoirs made with the highest concentration of PSS (30%), but with different contact time between paper layers.

In **Fig. 5.5**A,B, the nanoparticles are transferred as a ring when short transfer times are applied even when the % PSS is high. In **Fig. 5.5**C, the colorimetric signal increases as the time increases. These results invalidate the first mechanism, since no nanoparticles are observed in the center of the reservoir during the first stages of the transfer process at high % PSS. Therefore, we propose that nanoparticles and PSS are preferentially transferred from the edges of the reservoir. This generates a diffusion barrier that results in the subsequent transfer of polymer and nanomaterials in the central area of the receiving paper, in agreement with the second hypothesis proposed above. Experiments showing the transfer of PSS can be found in **Fig S4 appx 2**. Below we study the impact of nanoparticle concentration and paper type in the generation of specific and nonspecific signals for biosensing applications.

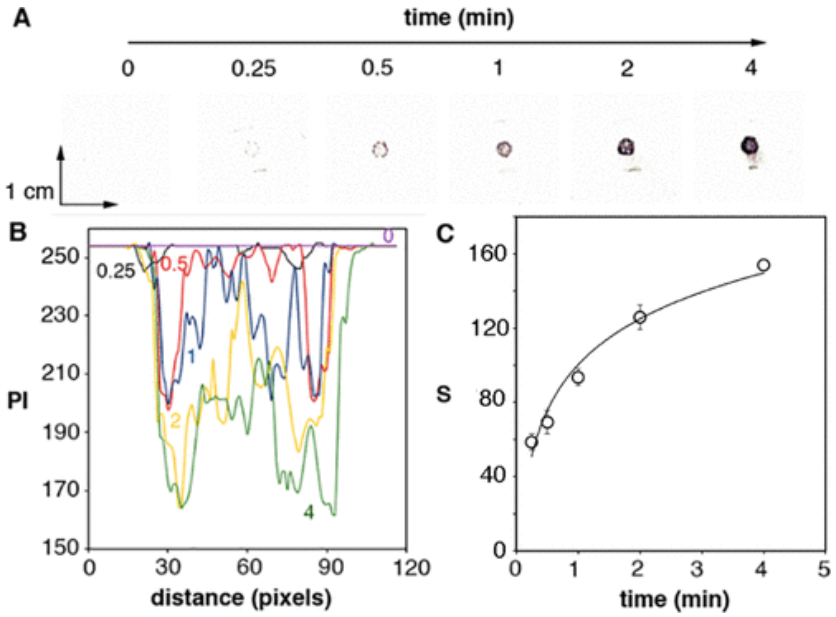

Fig. 5.5 *Time-dependent transfer of avidin-decorated nanoparticles from reservoirs containing 30% PSS to receiving substrates modified with biotinylated proteins; (A) scanned images of the receiving substrates after pressing the reservoirs for different times; (B) pixel intensity (PI) profiles and (C) colorimetric signal (S) in the receiving paper substrate. Trend lines are a guide to the eye. Error bars are the standard deviation (n = 3).*

Fig. 5.6 shows the effect of the receiving paper pore size in the generation of colorimetric signals when the reservoirs are loaded with 30% PSS and different concentrations of avidin-grafted gold nanoparticles. Nonspecific interactions were evaluated with non-biotinylated (BSA) (control lanes in **Fig. 5.6**A). Qualitative assessment of **Fig. 5.6**A shows that using Whatman paper #6 and #1 results in higher colored spots in control experiments compared to Whatman paper #41. This is ascribed to the higher specific area of paper types 6 and 1 because of their smaller pore sizes (3 and 11 µm, respectively), which favors nonspecific

interactions between nanoparticles and the receiving substrate. Analysis of the specific signals obtained after subtracting the control experiments shows that paper # 41 produces the highest specific signals when using nanoparticles in the concentration range between 140 and 290 nM, whereas paper #1 yields higher specific signals when using nanoparticles in the concentration range between 36 and 72 nM (**Fig S7 appx 2**). In **Fig. 5.6**C, the pixel intensity within the colorimetric signal is homogenously distributed (i.e., no ring formation) when the concentration of nanoparticles in the reservoir is 140 nM or higher and the receiving substrate is Whatman paper #41. These results, in addition to those obtained in **Fig. 5.4**, indicate that paper-based reservoirs containing 30% PSS and 140 nM nanoparticle probes are the best candidates to generate homogenous and highly intense plasmonic signals in biosensors. The reservoirs were able to establish biospecific interactions even after being kept for a month in an envelope at room temperature (**Fig S2 appx 2**). No preservatives were added, and no additional measures such as lyophilization or co-storage with silica gel were taken in order to further preserve the probes, which shows that the proposed method is useful for fabricating biosensors with extended shelf-life without the need to impose strict temperature or humidity storage conditions.

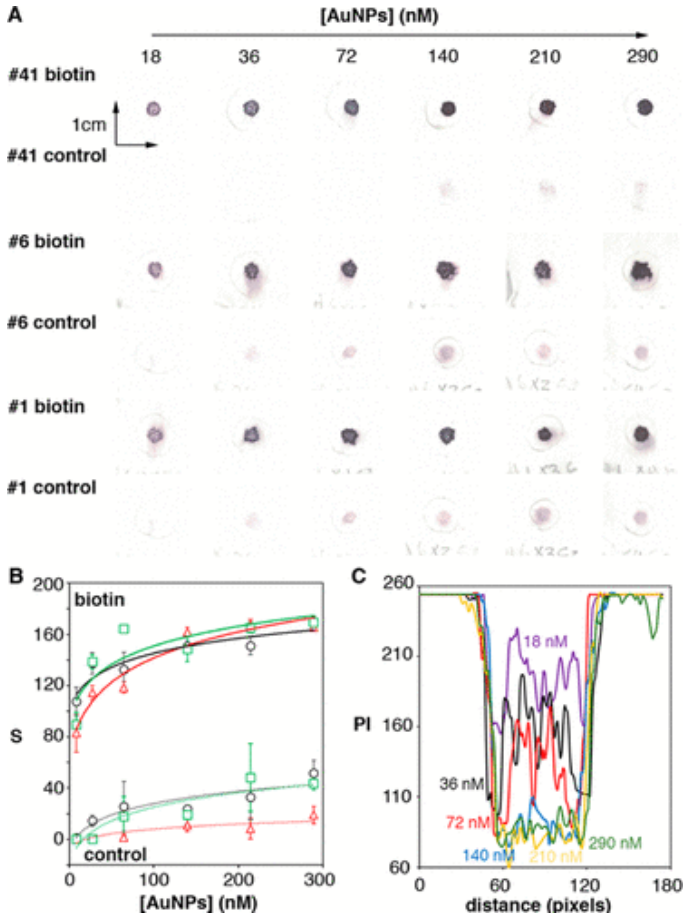

Fig. 5.6 *Transfer of avidin-decorated nanoparticles stored at different concentrations to receiving paper substrates with different pore sizes (22, 11, and 3 µm for Whatman Paper 41, 1, and 6, respectively) modified with biotinylated proteins; (A) scanned images of the receiving substrates modified with biotinylated BSA (biotin) or unmodified BSA (control); (B) colorimetric signals in receiving substrates made of Whatman paper #41 (red triangles), #6 (black circles), and #1 (green squares); control experiments with non-biotinylated BSA are indicated with dotted lines; (C) pixel intensity (PI) profiles across receiving substrates made of Whatman paper #41. Error bars are the standard deviation (n = 3). Trend lines are a guide to the eye.*

After optimizing the fabrication procedure of the nanoparticle reservoirs, we sought to apply them in sandwich immunoassay for the detection of the antigen gB from CMV. To this end, the avidin-decorated nanoparticles were modified with biotinylated detection antibodies and stored in the dry paper reservoir as explained above. The receiving paper substrate was modified with capture antibodies and blocked to prevent nonspecific interactions. The immunoassay consisted of adding the target analyte spiked into human serum to the receiving substrate and pressing the paper reservoir for 10 min. After washing away excess reagents, the colorimetric signal was recorded. The whole assay took less than 12 min to be completed. In **Fig. 5.7**, the proposed paper biosensors were able to detect gB with a limit of detection of 0.03 ng·mL^{-1} expressed as the first sample that yielded a signal higher than three times the standard deviation of the blank (green line in **Fig. 5.7**, 99% confidence). This

limit of detection is ca. 100 times lower than the one obtained with a disposable electrochemical biosensor for detecting CMV within 45 min [170] and three times lower than colorimetric ELISA that required several hours to be completed [169]. Control experiments performed with biosensors modified with anti-*E. coli* instead of anti-gB yielded lower nonspecific signals. These results demonstrate that the method for fabricating paper reservoirs containing protein-decorated nanoparticles can be extended to biomolecular interactions other than biotin–avidin interactions, for example, antibody–antigen interactions for developing paper-based immunoassays. It can also be used to store citrate-capped nanoparticles modified with antibodies (**Fig S6 appx 2**). Furthermore, the proposed method affords low limits of detection with very short incubation times, which makes it particularly useful for developing rapid diagnostic tests such as those required in decentralized healthcare schemes.

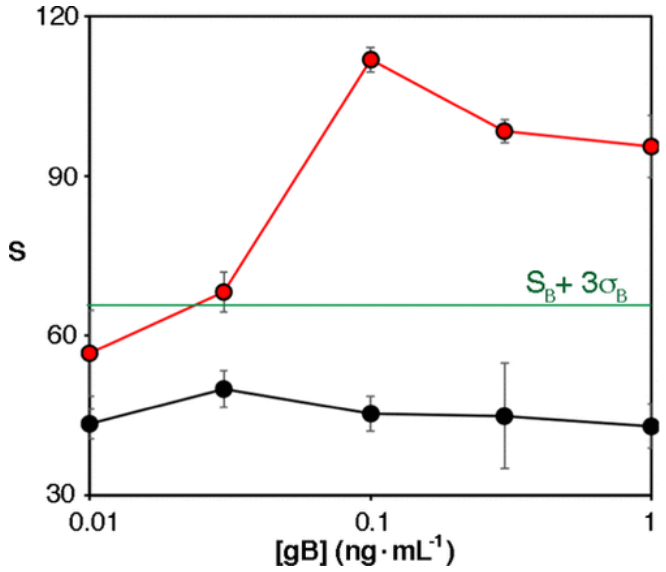

Fig. 5.7 *Detection of gB from human CMV in serum with reservoirs containing antibody-decorated nanoparticles and paper substrates modified with anti-gB (red dots) or anti-E. coli (black dots) (semilogarithmic scale). S is the colorimetric signal. Error bars are the standard deviation from three independent experiments (n = 3). The green line represents the limit of detection expressed as the blank signal (S_B) and three times the standard deviation of the blank ($3\sigma_B$).*

5.5 Conclusions

In conclusion, we have demonstrated that gold nanoparticles modified with PEG and proteins can be stored in filter paper when the substrate is previously treated with PSS. This avoids irreversible interactions with the paper, which enables a complete release of nanoparticles upon addition of an aqueous solution. It also enables transferring the nanoparticles from the reservoir to a receiving substrate by pressing one paper sheet

against the other with the finger. Fine-tuning the % PSS avoids the formation of “coffee rings” in both the reservoir and the receiving substrate. This leads to homogenously distributed colorimetric signals resulting from biomolecular interactions between the nanoprobes and substrate-bound molecules. The presence of PSS in the reservoir does not interfere with the generation of avidin–biotin or antibody–antigen interactions and preserves the nanoprobes for at least one month. The best paper types for receiving nanoparticles in paper-only biosensors are #41 when the nanoparticles are stored with a concentration between 140 and 210 nM or #1 when the nanoparticle concentration is 36–72 nM. Nanoparticles decorated with anti-gB were able to detect this analyte with a biosensor made entirely of paper rapidly and with a low limit of detection of 0.03 $ng \cdot mL^{-1}$ (99% confidence). These features make the proposed reservoirs ideal for fabricating paper-only biosensors for point-of-care diagnostics, especially when combined with wax-printed microfluidics.

6 PAPER BIOSENSORS FOR DETECTING ELEVATED IL-6 LEVELS IN BLOOD AND RESPIRATORY SAMPLES FROM COVID-19 PATIENTS

6.1 Abstract

Decentralizing COVID-19 care reduces contagions and affords a better use of hospital resources. We introduce biosensors aimed at detecting severe cases of COVID-19 in decentralized healthcare settings. They consist of a paper immunosensor interfaced with a smartphone. The immunosensors have been designed to generate intense colorimetric signals when the sample contains ultralow concentrations of IL-6, which has been proposed as a prognosis biomarker of COVID-19. This is achieved by combining a paper-based signal amplification mechanism with polymer-filled reservoirs for dispensing antibody-decorated nanoparticles and a bespoken app for color quantification. With this design we achieved a low limit of detection (LOD) of 10^{-3} pg·mL^{-1} and semi-quantitative measurements in a wide dynamic range between 10^{-3} and 10^{2} pg·mL^{-1} in PBS. The assay time is under 10 min. The low LOD allowed us to dilute blood samples and detect IL-6 with an LOD of 1.3 pg·mL^{-1} and a dynamic range up to 10^{2} pg·mL^{-1}. Following this protocol, we were able to stratify COVID-19 patients according to different blood levels of IL-6. We also report on the detection of IL-6 in respiratory samples (bronchial aspirate, BAS) from COVID-19 patients. The test could be easily adapted to detect other cytokines such as TNF-α and IL-8 by changing the antibodies decorating the nanoparticles accordingly. The ability of detecting cytokines in blood and respiratory samples paves the way for monitoring local inflammation in the lungs as well as systemic inflammation levels in the body

6.2 Introduction

The SARS-CoV-2 pandemic has rapidly spread worldwide with enormous social and economic repercussions [175]. Patients may be asymptomatic, have mild flu-like symptoms, or progress to severe pneumonia [176]. Previous studies on SARS-CoV and MERS-CoV show that infection of epithelial lung cells provokes a strong local inflammatory response characterized by high levels of cytokines and chemokines [177]. When these pro-inflammatory factors reach the bloodstream they stimulate the release of immature

granulocytes in the bone marrow, which exacerbates the inflammation [178]. The resulting hyperinflammatory syndrome or “cytokine storm” is believed to be responsible for many severe cases of COVID-19. IL-6 has been extensively used for prognosticating severe cases of COVID-19. Mild cases show serum IL-6 levels between 5.1 and 18.8 $pg \cdot mL^{-1}$, whereas in moderate/severe cases this value increases to 22.5–198 $pg \cdot mL^{-1}$ [179–184]. Stratifying patients according to severity is crucial in order to optimize COVID-19 management. During the first peak of the pandemic, saturation of hospitals forced healthcare providers to decentralize COVID-19 care. Even after “flattening the contagion curve” many mild cases of COVID-19 are cared for at home in order to reduce the risk of contagion [185]. Patients with severe symptoms are rapidly transferred to hospitals, where they receive specialized care to prevent poor outcomes. Biosensors for detecting elevated cytokine levels at the point of care could help physicians stratify patients according to their prognosis [186]. The challenge in designing such devices is that they would need to be highly portable, easy to manipulate, and require minimal infrastructure to ensure an easy implementation in a decentralized health care strategy [186, 187].

In this manuscript we meet this challenge with mobile biosensors that measure levels of IL-6 in blood and respiratory samples from COVID-19 patients in less than 10 min. In order to meet the urgent need for rapid testing we collated previous discoveries into a new design that meets the needs for decentralized COVID-19 diagnostics. It consists of devices that are entirely made of paper and comprised of two parts: a paper square containing a nanoparticle reservoir and a paper strip for target capture (**Fig. 6.1** A). The nanoparticle reservoir is made by adding polystyrene sulfonate (PSS) to a region of the paper. This prevents irreversible interactions between antibody-decorated nanoparticles and the cellulose substrate [188]. The reservoir dimensions are defined by a hydrophobic barrier made of paraffin. The paper strip has three capture sites (CS) for amplifying colorimetric signals without adding additional analytical steps [20]. To detect IL-6, a drop of sample is added to each capture site and quickly dried. The paper is then folded and soaked with a blocking solution. Subsequently, the reservoir is pressed on top of the folded strip with the aid of a clamp for 5 min (**Fig. 6.1** B). During this time, nanoparticles are transferred vertically from the reservoir to the three capture sites (**Fig. 6.1** E), where the antibodies recognize IL-6 specifically. After removing the reservoir, a colored spot appears whose pixel intensity is directly related to the concentration of IL-6 in the sample. Since filter paper is semi-transparent when wet, and the biosensors generated a colorimetric signal in each capture site, the colored spot on the folded paper is the sum of the three independent signals generated at each capture site [20].

This collective, amplified signal is then quantified with a previously developed smartphone app for densitometry at the point of need [189]. The origami-enabled signal amplification mechanism achieves a limit of detection of 10^{-3} pg·mL^{-1}, which is one of the lowest reported to date (**Table S1 appx 3**) [[130][131] [91][133] [135] [136] [137] [83, 84, 196–202, 89, 189–195]]. Thanks to this low limit of detection in PBS we were able to dilute patient samples for detecting elevated levels of IL-6 without performing any additional purification steps. This was accomplished in both blood and respiratory samples, thus paving the way for using the proposed biosensors for monitoring systemic and local inflammation. Being able to detect high levels of IL-6 in different biological matrices, along with the rapid turnaround time and highly portable detection system, makes our biosensors ideal for the decentralized monitoring of COVID-19 patients both at home and in hospitals.

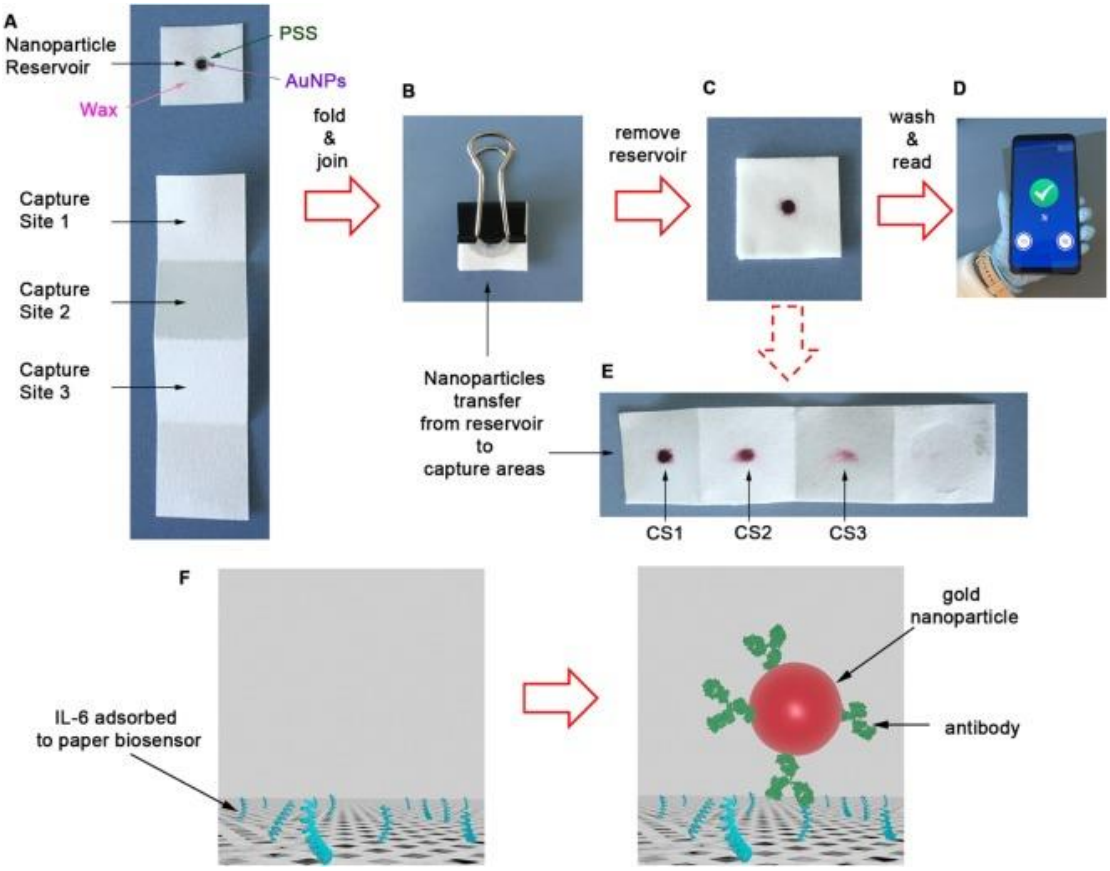

Fig. 6.1 *Photographs of the paper immunosensor and key analytical steps for detecting IL-6; (A) The biosensors consists of a piece of paper containing antibody-decorated nanoparticles, and a paper strip with three capture sites (CS); (B) After adding a drop of sample in each capture site and drying it, the paper is folded; (C) After removing the reservoir, a colored spot appears whose pixel intensity is the sum of the colorimetric signal generated in each capture site; (D) After washing away excess reagents the colorimetric signal is measured with a previously developed smartphone app within seconds; (E) Unfolding the paper strip in (C) reveals that nanoparticles are transferred vertically to the 3 binding sites; (F) Schematic representation of biomolecular interactions; IL-6 is adsorbed onto the paper substrate and subsequently detected by antibody-decorated gold nanoparticles.*

6.3 Materials and methods

6.3.1 Materials

Whatman filter paper #41 and #1 was obtained from GE Healthcare Life Sciences. Wax Paper Squares (6″) was purchased from NORPRO. Gold (III) chloride hydrate, sodium citrate tribasic dihydrate, poly (ethylene glycol) 2-mercaptoethyl ether acetic acid (thiol-PEG-acid) 2100, N-Hydroxysulfosuccinimide sodium salt (sulfo-NHS), N-(3-Dimethylaminopropyl)-N′-ethylcarbodiimide hydrochloride (EDAC; EDC), O-(2-biotinyl-aminoethyl) polyethylene glycol 3000 (biotin-PEG), poly (sodium 4-styrenesulfonate, average Mw ≈ 70.000) 30 % solution, Tween-20, 2-ethanesulfonic acid (MES) and recombinant human IL-6 (I2786) were obtained from Sigma Aldrich. Rabbit anti-IL-6 polyclonal antibody (ab6672) was purchased from Abcam. Albumin from bovine serum (BSA, protease free) was obtained from VWR Chemicals. PBS refers to phosphate buffered saline pH 7.4. PBST refers to PBS supplemented with 0.1 % Tween-20. RT refers to room temperature.

6.3.2 Antibody-decorated gold nanoparticles

Gold nanoparticles with a diameter of ca. 40 nm were obtained with the citrate-reducing method as previously described [189]. The nanoparticles were subsequently modified with antibodies adapting a published protocol. In brief, the citrate around the nanoparticles was substituted for thiol-PEG-acid. Then, the carboxylated moieties were transformed into reactive sulfo-NHS esters via the addition of EDC (1 mg) and sulfo-NHS (2 mg) in 0.5 M MES buffer pH 5.5 for 30 min. Then 200 µL of the nanoparticles were centrifuged at 8000 rpm for 6 min and rabbit anti-IL-6 polyclonal antibody (1 $mg \cdot mL^{-1}$) was added overnight. Then 200 µL of a blocking solution containing glycine (0.1 M) and BSA (10 $mg \cdot mL^{-1}$) in phosphate buffer (0.1 M, pH 7.0) was added for at least 30 min to cap any remaining sulfo-NHS ester groups. Subsequently, nanoprobes were washed 5 times with PBST (6000 rpm, 6 min). Finally, the pellet was resuspended in 100 µL of PBST ([Au] ≈ 250 mM).

6.3.3 Fabrication of origami biosensors

For the reservoir, Whatman paper #1 was cut into 2 × 2 cm squares, which were then printed with wax with the following procedure. First, wax paper was cut into 2 × 2 cm squares. A 5 × 5 mm circle was removed from the center with a hole puncher. The remaining wax was aligned with the Whatman paper and the paraffin was transferred by pressing a hot iron against it for 5 s. The procedure was repeated on the other side of the paper to completely seal it. Then, a nanoparticle-reservoir was fabricated in the unwaxed paper area by adding

3 µL of 30 % PSS and letting it dry at room temperature (RT) followed by adding 1 µL of antibody-decorated nanoparticles and letting it dry at RT. Paper strips for analyte capture consisted of pieces of Whatman paper #41 cut into 2 × 8 cm strips as shown in **Fig. 6.1** A.

6.3.4 Detection of IL-6

First, 10 µL of sample was added to the first three squares of the paper strip (CS1, 2, and 3 in **Fig. 6.1** A) and dried with a hair drier for 30 s. Then, the strip was folded and 1 mL of PBS-BSA was added. Immediately afterwards, the nanoparticle reservoir was placed onto the strip and held with the aid of a clamp for 5 min. The reservoir was then peeled off and the paper strip was washed five times with 1 mL of PBST. The resulting colorimetric signal was measured immediately afterwards with the mobile app [189] Details about the development of the mobile app have been published elsewhere [189]. The app guides the user to establish a controlled distance and angle between the camera of the Huawei POT-LX1smartphone and the assay by using a virtual frame on the screen that matches the shape of the paper biosensor. After pressing “Set” the app automatically finds the region of interest, calculates the pixel intensity and subtracts it from the background. Uneven light conditions are also automatically corrected. The app stops taking measurements if there are any changes in imaging conditions. This informs the user that the smartphone needs to be realigned, at which point the measurements resume. The data set is evaluated after 50 valid measurements have been acquired. The resulting colorimetric signal S is the highest for black (255) and the lowest for white (0).

Spiked blood samples and bronchial aspirate (BAS) samples were obtained and processed as follows. A blood sample from a healthy donor was spiked with IL-6 by adding 1 µL of a solution 10 times more concentrated to 9 µL of blood. The final concentration of added IL-6 was the one reported in **Fig. 6.3** B. The samples were then diluted 1000 times with PBS and tested as above. BAS samples were first liquefied by adding 100 µL of 0.3 M H_2O_2 to 10 mg of samples for 1 min. The IL-6 concentration of these samples was determined with an in-house ELISA (**Fig S1 appx 3**). A liquefied BAS sample containing less than 3 $pg \cdot mL^{-1}$ IL-6 (below the limit of detection of ELISA) was spiked with the same procedure detailed for blood samples. Samples were diluted 10 times with PBS before applying them to the paper biosensor.

Blood samples from COVID-19 patients were obtained from the Immunology Department at Son Espases University Hospital (Ethics Committee Protocol IB 4169/20 PI). The IL-6 concentration was determined with a DIASource Immunoassay ELISA kit. Informed consent

was obtained from all participants. BAS samples from patients included in this study were provided by Biobank IdISBa and CIBERES Pulmonary Biobank Consortium, a network currently formed by twelve tertiary Spanish hospitals integrated in the Spanish National Biobanks Network. They were processed following standard procedures with the appropriate approval of the Ethics and Scientific Committees and with the collaboration of the healthcare services of the Hospital Universitario Son Espases and Hospital Son Llàtzer.

6.4 Results and discussion

The biosensors shown in **Fig. 6.1** incorporate a signal amplification mechanism based on adding the colorimetric signals generated in multiple capture sites. This concept has already been tested for amplifying signals in paper immunosensors, although not for the detection of IL-6 [20]. To test the impact of implementing this design in the IL-6 biosensors, samples containing 0 or 10 $pg \cdot mL^{-1}$ IL-6 were tested with biosensors modified with nanoparticles at different concentrations. The colorimetric signal was measured with two methods. The first method calculated the pixel intensity only in the capture site CS1. The second method involved folding the paper to measure the collective signal from CS1, CS2 and CS3. **Fig. 6.2** A shows scanned images for the resulting assays. As the concentration of gold nanoprobes increased the color in the spot also increased. The color in the folded samples (highlighted in red) was more intense than in the unfolded ones. This is because in the folded sample, the signal from the three capture sites is cumulative [20]. Colored spots were more intense in samples containing IL-6, which indicated that the main contribution to the signal was the specific recognition of IL-6 by antibody-decorated nanoparticles. **Fig. 6.2** B summarizes the results obtained after quantifying the color intensity in 3 independent experiments. In this Figure, signals increase when the paper was folded in agreement with the observations in **Fig. 6.2** A. In **Fig. 6.2** C the specific signal obtained after subtracting the blank from the 10 $pg \cdot mL^{-1}$ sample was plotted as a function of the concentration of nanoprobes. In this plot, the specific signal was always higher when the paper was folded. Furthermore, the standard deviation of three independent experiments was smaller when the paper was folded than when measuring a single capture site. These results confirm that the proposed method enhances specific colorimetric signals in paper immunosensors without increasing variability. The method only required adding three drops of sample instead of one. No additional reagents or analytical steps were required, making it useful for amplifying signals in rapid diagnostic tests.

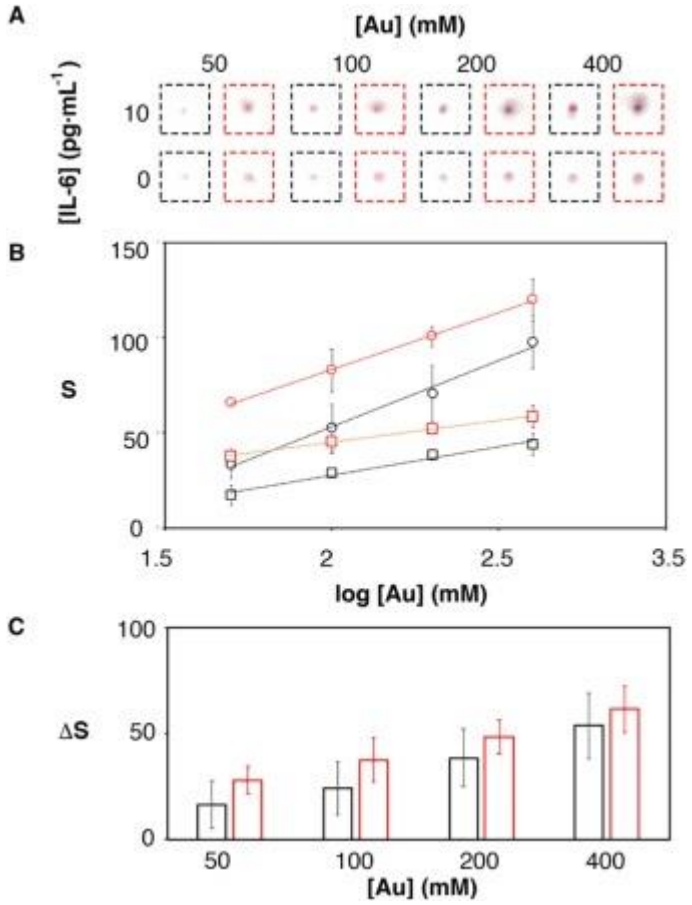

Fig. 6.2 *Colorimetric signal obtained from samples containing 0 or 10 pg·mL^{-1} when using 3 capture sites (CS) and the paper is folded so that the 3 signals add up (red), or unfolded and measuring only CS1 (black); (A) Photographs of the assays; (B) colorimetric signal for 10 (dots) and 0 (squares) pg·mL^{-1}; (C) Specific signal after subtracting 0 from 10 pg·mL^{-1}; Error bars are the standard deviation (n = 3).*

After testing the signal amplification mechanism, we calibrated the biosensors with solutions containing different concentrations of recombinant human IL-6 in PBS. In **Fig. 6.3** A, the biosensors generated dose-dependent signals that increased linearly with the logarithm of the concentration of IL-6 in the range between 10^{-3} and 100 pg·mL^{-1}. The limit of detection, expressed as the assayed sample that yields a signal above three times the standard deviation of the blank (99 % confidence), was 10^{-3} pg·mL^{-1}. This is one of the lowest limits of detection reported for IL-6, and it was achieved with a fast turnaround time under 10 min (**Table S1 appx 3**).

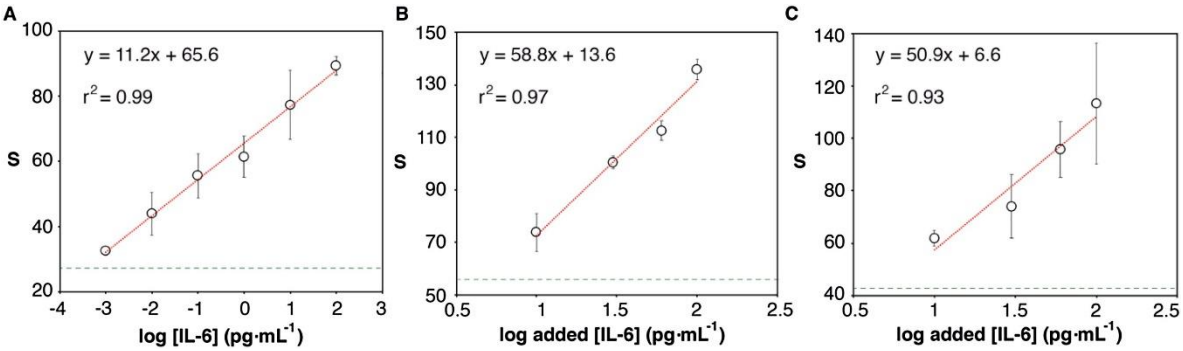

Fig. 6.3 *Detection of IL-6 in PBS (A), or spiked into blood (B), or bronchial aspirate (BAS, (C)). Horizontal green dotted lines represent the signal above 3 times the standard deviation of the blank. Error bars are the standard deviation (n = 3).*

However, the proposed biosensors may have a drawback when detecting IL-6 in real matrices. With our device, the analyte is captured by drying the sample in the paper. While this expedites the detection of IL-6, biomolecules such as proteins and mucins present in real matrices may also physically adsorb to the paper and hinder the capture of IL-6. They may also interact non-specifically with the antibody-nanoparticles, interfering with the detection of IL-6. Blood samples are also highly colored, which can be problematic for colorimetric signal generation methods. Fortunately, the biosensors have an exceptionally low limit of detection that allows for the dilution of samples prior to testing, therefore diluting color interferents from the matrix as well. It has been proposed that healthy individuals have IL-6 levels between 0.5 and 6 pg·mL^{-1} [203]. Diluting samples 10^3 times should still enable detecting IL-6 above 6 pg·mL^{-1} (0.006 pg·mL^{-1} in the diluted sample), while reducing matrix effects. With this in mind, we spiked blood samples from a healthy donor with IL-6 in the concentration range between 10 and 100 pg·mL^{-1}. Then we diluted these samples 1000 times with PBS and tested them with our biosensors. In **Fig. 6.3** B, the biosensor yielded a linear response with the logarithm of the concentration of added IL-6 in the concentration range proposed. These experiments demonstrate that the biosensors can detect IL-6 in blood in the relevant range for COVID-19 care [204]. According to the standard addition method, the basal IL-6 concentration can be estimated in **Fig. 6.3** B when Y = 0. This yields a value of 0.6 pg·mL^{-1}, which fits well with the IL-6 levels in a healthy individual. The limit of detection obtained by substituting $S_{blank} + 3\sigma$ in the linear fitting yields a value of 0.7 pg·mL^{-1}. Since this this has been added to basal levels in the sample, the final limit of detection in blood is 1.3 pg·mL^{-1}. Taking into consideration that the sample was diluted 10^3 times, this limit of detection in blood agrees well with the value obtained in PBS (10^{-3} pg·mL^{-1}, **Fig. 6.3** A), which validates our biosensors for detecting abnormal levels of IL-6 (above 6 pg·mL^{-1},

highest value for healthy individuals) in blood samples. Finally, we tested whether our biosensors could detect IL-6 in spiked respiratory samples (bronchial aspirate, BAS). To this end, liquefied BAS samples were diluted 10 times with PBS and tested with the same procedure shown above. In **Fig. 6.3** C, all samples yield a dose-dependent signal above three times the standard deviation of the matrix signal. These results indicate that our biosensors could be used for monitoring variations in cytokine levels in respiratory samples from COVID-19 patients as well.

Comparison of calibration plots in **Fig. 6.3** reveals that experiments performed in real matrices yield higher sensitivity (higher slope of the calibration plot). That is, the presence of a diluted biologic matrix facilitates the detection of IL-6 compared to the same experiments performed in PBS. The basal concentration of IL-6 in the samples is a constant value added to the concentration spiked into the sample, and therefore cannot be responsible for this increase in sensitivity. We hypothesized that biological components in the matrix that remain in the paper after drying could facilitate antibody-antigen interactions, for example by providing a native environment that preserves IL-6 conformation. The most abundant protein in blood is human serum albumin (HSA), which is a present at a concentration of around 40 $mg \cdot mL^{-1}$. To test whether the presence of albumin in the sample could increase the sensitivity of our biosensors, we repeated the calibration experiments, but instead of diluting recombinant IL-6 with PBS we diluted it with PBS supplemented with 40 $\mu g \cdot mL^{-1}$ bovine serum albumin (BSA). BSA is very similar to HSA in its amino acid composition (76 % homology, [205]), and 40 $\mu g \cdot mL^{-1}$ is the approximate concentration after diluting the sample 10^3 times. In **Fig S2 appx 3**, the slope of the calibration plot increases from 11.2 in PBS to 22.4 in PBS-BSA. These experiments demonstrate that the presence of excess proteins in the sample increases the sensitivity of the proposed biosensors. Furthermore, comparison of the same tests measured with the mobile app or via image analysis with ImageJ yielded a higher slope with the app (22.4 vs 16.3), which shows that the quantification method also helps increase the sensitivity of the assay (**Fig S2 appx 3**). To summarize, the high sensitivity and low limit of detection of our tests originate from the paper-based signal amplification mechanism (**Fig. 6.2**), the composition of diluted biological matrices (**Fig. 6.3** and **Fig S2 appx 3**), and the utilization of a bespoken app for color quantification (**Fig S2 appx 3**). While our tests are semi-quantitative compared to ELISA (**Fig S2 appx 3**) their sensitivity in real matrices may be high enough for detecting high levels of IL-6 in patient samples at the point of care. This is explored below.

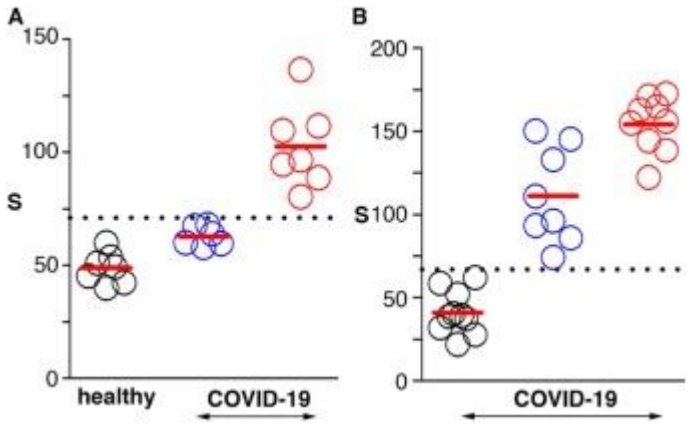

Fig. 6.4 *Detection of IL-6 in real samples; (A) blood samples from healthy donors (black) or COVID-19 patients with IL-6 levels below (blue) or above (red) 17 pg·mL^{-1}; (B) Bronchial aspirate (BAS) samples from COVID-19 patients with IL-6 levels below 10 pg·mL^{-1} (black), between 10 and 100 pg·mL^{-1} (blue), or above 100 pg·mL^{-1}(red). Dotted lines show the average signal plus 2 times the standard deviation of healthy donors (A) or patients with IL-6 below 3 pg·mL^{-1} (B).*

Next we tested whether the proposed biosensors could be used for detecting high levels of IL-6 in a panel of blood and BAS samples from patients, which were also analyzed with the gold standard (ELISA) in order to quantify IL-6. In **Fig. 6.4** A, patient samples containing IL-6 above 17 pg·mL^{-1} yielded signals statistically different when compared to blood samples from healthy donors (Kruskall-Wallis test, $p < 0.001$). This threshold value was in agreement with the cut-off value proposed in the literature to prognosticate severe COVID-19 as well as to guide specific anti-inflammatory treatments [206, 207]. **Fig. 6.4** B summarizes the results obtained from analyzing BAS samples. BAS is usually obtained from intubated patients, and therefore we were not able to compare our results with healthy donors. Instead, we used samples containing IL-6 below 10 pg·mL^{-1} in order to establish a cut-off value. In **Fig. 6.4** B, samples containing IL-6 with a concentration of 10 pg·mL^{-1} or higher can be differentiated from those containing undetectable levels by ELISA (Kruskall-Wallis test, $p < 0.001$). However, it was not possible to distinguish among samples containing intermediate (10−100 pg·mL^{-1}) and high (above 100 pg·mL^{-1}) levels of IL-6 with the proposed biosensors. To the best of our knowledge no clinical study correlating the levels of IL-6 in respiratory samples with patient severity has yet been published in the context of COVID-19. It should be noted that the decentralized detection of IL-6 in respiratory samples would require sputum rather than BAS, since BAS is usually obtained from intubated patients. While the experiments shown here demonstrate the possibility of measuring IL-6 in samples from the lower respiratory tract, further studies should be performed for determining appropriate cut-off values in sputum samples.

6.5 Conclusions

In conclusion we have introduced paper immunosensors with a mobile readout platform for the detection of IL-6 in blood and respiratory samples from COVID-19 patients. The immunosensors have a low limit of detection at 10^{-3} pg·mL^{-1} in PBS. Semi-quantitative measurements can be performed in a wide dynamic range over 5 orders of magnitude due to their paper-based signal generation design. This excellent performance enables diluting real samples to reduce matrix interference. Thanks to this procedure, we were able to correctly classify blood samples from COVID-19 patients with an IL-6 content higher than 17 pg·mL^{-1}, and BAS samples above 10 pg·mL^{-1}. Higher cut-off values could be set by diluting samples to a larger extent. The biosensors could be adapted to detect other cytokines such as TNF-α and IL-8 by substituting the antibodies around the nanoparticles for others that can recognize these targets specifically. The tests are entirely made of filter paper, which makes them lightweight, easy to transport and distribute, and easy to dispose of by incineration. Our app does not require any lightbox or accessory to control photographic conditions, making it particularly useful for home testing. These features, along with the ability to identify patients with elevated IL-6 levels at low cut-off values, makes the proposed biosensors a promising tool for the decentralized management of COVID-19 patients at home or in hospitals.

7 RAPID DETECTION OF *PSEUDOMONAS AERUGINOSA* BIOFILMS VIA ENZYMATIC LIQUEFACTION OF RESPIRATORY SAMPLES

7.1 Abstract

Respiratory infections caused by multi-drug-resistant *Pseudomonas aeruginosa* often yield poor outcomes if not detected right away. However, detecting this pathogen in respiratory samples with a rapid diagnostic test is challenging because the protective biofilms created by the pathogen are themselves surrounded by a high-viscosity sputum matrix. Here, we introduce a method for liquefying respiratory samples and disrupting bacterial biofilms on the spot within a minute. It relies on the generation of oxygen bubbles by bacterial catalase through the addition of hydrogen peroxide. When coupled with a mobile biosensor made of paper, the resulting diagnostic kit was able to detect *P. aeruginosa* infections in sputa from patients with excellent sensitivity and specificity within 8 min. The quick turnaround time along with few infrastructure requirements make this method ideal for the rapid screening of *P. aeruginosa* infections at the point of care.

7.2 Introduction

Unattended infections can progress to systemic inflammation and multiorgan dysfunction (i.e., sepsis), leading to a poor prognosis and potential long-term sequelae [81]. It is known that sepsis survival rates decrease when the antimicrobial treatment is delayed.[208] Accordingly, protocols for sepsis management recommend an empiric antibiotic regime as soon as possible, and preferably within the first hour of suspecting sepsis [209]. Yet, infections caused by antibiotic resistant pathogens still yield poor outcomes even when antibiotics are administered in a timely manner [210]. This is particularly problematic in the context of sepsis caused by *Pseudomonas aeruginosa* infections because many strains are only treatable with one antibiotic: colistin. Colistin is rather toxic when administered intravenously and not routinely recommended within the first empirical antibiotic regime [211]. In this situation, patients can rapidly progress to deadly septic shock. Pathogen identification through bacteriological culture takes too long to guide the first antibiotic treatment. Multidrug-resistant *P. aeruginosa* is highly prevalent in hospital acquired pneumonia, and pneumonia is the underlying infection in 45% of sepsis cases in the US and

Europe [212]. Thus, there is a specific need to develop technologies for the rapid detection of *P. aeruginosa* in respiratory samples. Such a test would alert clinicians to infections by this hazardous pathogen, thus providing much-needed guidance during the administration of the first antibiotic regime.

Using a rapid biosensor could tackle this issue by revealing the presence of *P. aeruginosa* in respiratory samples at the point of care [155][213–218]. Paper-based immunosensors would be ideal candidates for this application since they can be disposed of by incineration, thus destroying any hazardous respiratory pathogens. However, detecting *P. aeruginosa* in respiratory samples such as sputum and bronchial aspirate with immunosensors is challenging due to the barriers surrounding the pathogen. First of all, the sample matrix is made of highly cross-linked mucins with a highly viscous or even semisolid consistency [219]. Pathogens trapped within this matrix are not readily available for detection. Second, within this matrix, *P.aeruginosa* further encases itself in a biofilm [220, 221]. Bacteria trapped within the biofilm are also not detectable. Thus, the detection of *P. aeruginosa* in these samples requires the liquefaction and homogenization of samples as well as the rupture of bacterial biofilms to avoid false negatives. Current approaches for processing respiratory samples are cumbersome and often require infrastructures such as a vortex, an incubator, or a particle manipulator [222–227]. Furthermore, it has not been proven that these methods disrupt biofilms. A method that instantly liquefies respiratory samples and also disrupts biofilms could enable the detection of respiratory pathogens at the point of care. This would enable a personalized approach for administering the first antibiotic regime since nosocomial infections by this pathogen require a different therapeutic approach than the rest.

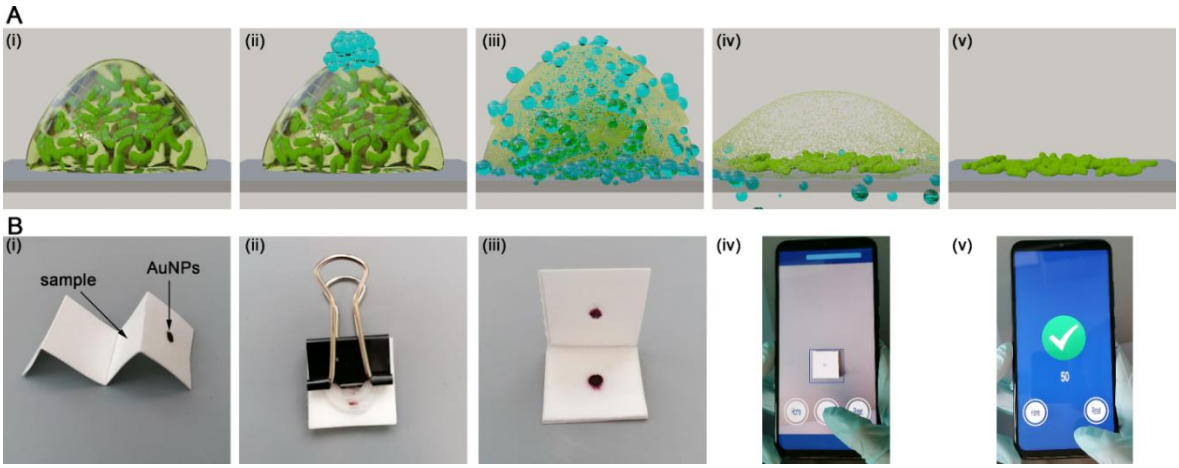

Fig. 7.1*Schematic representation of sample liquefaction (A) and P. aeruginosa detection (B) with the proposed method; (A) Bacteria are trapped in biofilms within respiratory samples (i); the addition of H_2O_2 (ii) causes catalase enzymes to generate oxygen bubbles (iii), which liquefy the sample and destroy biofilms in one step (iv and v); (B) The origami immunosensors consist of a piece of paper folded into four 2 x 2 cm squares (i); The top square contains a nanoparticle reservoir* [188]. *After adding the sample, the immunosensor is folded and the nanoparticles are transferred to the detection area (ii); After washing away excess reagents, the recognition of bacterial antigens by antibody-decorated gold nanoparticles generates a colored spot (iii); The spot is detected and quantified by aligning the paper biosensor with a smartphone app (iv) and pressing a button (v).*

In this paper, we describe a new approach for disrupting *P.aeruginosa* biofilms and liquefying sputum samples in one step. It only requires adding an aqueous solution of hydrogen peroxide to the sample. Bacterial catalase enzymes generate oxygen bubbles that break the biofilm and liquefy the sample matrix within a minute (**Fig. 7.1**A). No additional instrumentation or separation steps are required. Catalase has been previously used as an enzyme label or biorecognition element in biosensing,[228–230] and as a building block for micro/nanomotors,[142] [231, 232] biofuel cells,[233] and drugs [234]. Here, we introduce a novel use of this enzyme for liquefying respiratory samples prior to immunodetection. Catalase is produced by *P.aeruginosa*, as well as by staphylococci, and Enterobacteriaceae, which also generate biofilms and are highly prevalent in patients with hospital-acquired pneumonia [212]. It is also present in other bacterial and fungal species, making this approach useful for dissolving respiratory samples for a wide array of pathogens. Once the pathogens have been released from the matrix and their biofilms, they are available to be detected with a rapid diagnostic test at the point of care. Here, we demonstrate this concept using paper immunosensors with a mobile readout (**Fig. 7.1**B). In these devices, a drop of liquefied sample is applied to a paper substrate and dried for 30s (**Fig. 7.1**B(i)). This step traps bacterial antigens in the cellulose matrix. Next, the paper is folded to transfer antibodydecorated gold nanoparticles from a reservoir to the detection zone for 5 min (**Fig. 7.1**B(ii)). The specific recognition of *P. aeruginosa* antigens attached to the paper generates a colored spot (**Fig. 7.1**B(iii)), which is then quantified with a smartphone app in a matter of seconds (**Fig. 7.1**B(iv, v)) [189]. The whole process, including sample liquefaction and pathogen detection, can be performed in less than 8 min by a frontline healthcare worker. This quick turnaround time makes our detection kit suitable for guiding antibiotic prescriptions at the point of care, a much-needed development for improving sepsis management.

7.3 Materials and methods

7.3.1 Liquefaction of Sputum Samples

Sputum samples were collected by the Microbiology Unit at Son Espases University Hospital (Balearic Islands). Quantitative culture for bacterial pathogens was carried out by plate counting of bacterial colonies after seeding serial dilutions of sputum previously homogenized with Sputasol (6.5 mM dithiotreitol). Samples with a bacterial load ≥105 colony-forming units (cfu) were considered respiratory tract infections. Sputum samples negative for bacterial infection, determined using Gram's stain screening test, were included as controls.

Prior to liquefaction, raw samples containing *Pseudomonas aeruginosa* (PA+), Staphylococcus spp., or different species of the Enterobacteriaceae family (PA−) as infection-causing pathogens or a mixed flora (MF) were collected and kept at −20 °C until used. After thawing at room temperature (RT), 10 mg was collected in a 1.5 mL Eppendorf tube and liquefied by adding 0.3 M H_2O_2 in PBS at a constant 20:1 ratio (v/w) for 60 s. To demonstrate that sputum liquefaction is due to the oxygen bubbles produced by catalase, enzymes in the PA+ and MF sputum samples were inhibited by adding 100 µL NaN_3 at different concentrations for 2h at RT. Then, the solution was carefully removed and 0.3 M H_2O_2 was added. Videos and photographs were obtained using a LEICA MC170 HD digital camera coupled to a ZuZi stereo microscope with transmitted illumination.

7.3.2 In Vitro Disruption of *P. aeruginosa* Biofilms

Pseudomonas aeruginosa (PA) biofilms were obtained by a closed system in 96-well, round-bottom microtiter plates. Plates were filled with 100 µL sterile Luria−Bertani (LB) broth culture and inoculated with the PAO1 strain. After 24 h of incubation in a 5% CO2 atmosphere and at 37 °C, biofilm formation occurred as a ring around the well. To carry out studies of PA biofilms by confocal laser scanning microscopy (CLSM), we followed a previously published protocol, with some modifications [235]. Briefly, eight-well microslide ibiTreat chambers (ibidi) were filled with 300 µL LB, inoculated with the PAO1 strain, and incubated in a 5% CO2 atmosphere and at 37 °C for 24−48 h in a closed system.

To study the effect of H_2O_2 in the biofilm microstructure, the LB broth culture was carefully removed from plates after biofilm formation and then the wells were gently rinsed, keeping flocs untouched, by repeatedly filling and emptying with PBS (final volume of 100 µL per well). Finally, 50 µL PBS containing increasing amounts of H_2O_2 was added and incubated

for 5 min. Micrographs were obtained using a Cell Observer inverted microscope (Carl Zeiss). Images were obtained in the same coordinate of each microwell before and after H_2O_2 treatments using 5× objective lenses with bright-field illumination. Densitometric analysis was performed with Photoshop by calculating the pixel intensity (PI) of the whole image using the histogram function with the luminosity channel. The colorimetric signal S was taken as the integer value after subtracting the background signal. The increase in the colorimetric signal (ΔS) was obtained by subtracting S measured after H_2O_2 treatment from S before H_2O_2 treatment. To evaluate with higher resolution, the effect of H_2O_2 on the biofilm architecture, LB broth was carefully removed from microslides prepared for CLSM studies, and live cells and extracellular polymeric substances (EPS) were, respectively, stained with 17 μM SYTO9 (Invitrogen) and 100 $\mu g \cdot mL^{-1}$ concanavalin Atetramethylrhodamine isothiocyanate (ConA-TRIC, Invitrogen) in 0.1 M sodium bicarbonate (pH 8.3) [236]. CLSM images were obtained using an LSM 710 confocal microscope (Carl Zeiss) before and after H_2O_2 treatments using 63X oil immersion objective lenses. CLSM measurements were also made on biofilms grown under Fe starvation conditions to downmodulate catalase activity[237] (following the method shown in **Fig S5 appx 4** and **Fig S6 appx 4**).

Experiments to disrupt biofilms attached to the plates were performed as follows: first, the plates were decanted to remove all planktonic cells and flocs. They were then rinsed in three sequential steps by immersing the plate in sterile PBS, decanting, and tapping paper towels over them. Next, 175 μL PBS containing increasing concentrations of H_2O_2 was added for 60 s. To demonstrate the release of antigens from the biofilms attached to the plate, the supernatants after hydrogen peroxide treatment were analyzed with ELISA as explained in the Supporting Information.

The following experiments were performed to elucidate whether adding H_2O_2 for 60 s would kill cells and detach them from the biofilm. After following the above-mentioned biofilm disruption protocol, H_2O_2 was removed by immersing the plates in PBS once. Next, wells were decanted by inverting the plate and filled with 100 μL PBS. The remaining bacteria that adhered to the inner surface of the wells were gently detached by bath sonication (two cycles of 30 s at 160 W with 1 min intervals) and stained with 5 μL of 75 μM P-Io (propidium iodide, BD Pharmingen) for 15 min at RT. The plates were then centrifuged at 3000 rpm for 5 min, excess of P-Io was removed by discarding supernatants, and bacterial pellets were resuspended with 100 μL PBS. Finally, stained bacteria were pipetted into a 96-well black plate (Greiner Bio-One) and the P-Io fluorescence was measured in a Sinergy H1 microplate

reader (Biotek). After autofluorescence subtraction, the percentage increase of P-Io fluorescence intensity (FI) was expressed as [(FI after H_2O_2 treatment - FI without H_2O_2 treatment)/FI without H_2O_2 treatment] × 100.

7.3.3 Detection of *P. aeruginosa* with Origami Immunosensors

Gold nanoparticles (AuNPs) with a diameter of 40 nm were synthesized following the Turkevich method as described previously.[188] Trisodium citrate at a final concentration of 0.75 mM was added to a boiling gold chloride hydrate solution with a concentration of 0.50 mM for 10 min on a heated plate with vigorous stirring.Nanoparticle growth was confirmed by the appearance of a dark redwine color. When the solution reached RT, the AuNPs were consecutively pegylated, concentrated, and functionalized with avidin according to the procedure described previously [188]. Antibody-decorated nanoparticles were obtained by adding 10 µL polyclonal biotin anti-*Pseudomonas aeruginosa* developed in rabbit (Invitrogen) to 100 µL avidin-decorated nanoparticles for 1 h. Free biotin-binding sites were capped with 0.1 mM biotin−PEG (O−[2-(Biotinyl−amino)ethyl]−O′−(2-carboxyethyl)−polythylene glycol, Mw: 3.000, Sigma) for 30 min. Excess reagents were washed away by three consecutive centrifugation steps at 4 °C and 6000 rpm during 6 min using PBST as washing buffer. Origami immunosensors were fabricated as follows: Whatman paper #41 was cut into 2 cm × 8 cm strips, which were folded like an accordion to yield four 2 cm × 2 cm squares as shown in **Fig. 7.1**B. The top square was modified with wax. To accomplish this, waxed paper (PME) was cut into 2 cm × 2 cm squares. A 5 mm × 5 mm circle was cut in the center using a hole puncher. The wax was transferred to the Whatman paper by pressing with a hot iron, causing the melted wax to penetrate into the paper. The procedure was repeated on the other side of the paper to completely seal it. In the circle at the center of the paper that remained unwaxed, a nanoparticle reservoir was fabricated by adding 3 µL of 30% polystyrene sulfonate (PSS, MW 700.000, Sigma) and letting it dry at RT [188]. Then, 1 µL antibody-decorated nanoparticles were added and dried at RT.

To detect *P. aeruginosa*, 10 µL of sample was spotted onto the receiving paper substrate and dried with a hair drier for 30 s. Subsequently, the paper biosensors were blocked by adding 1 mL of PBS−BSA. The paper was immediately folded to transfer antibody nanoparticles from the reservoir to the detection zone by pressing with a clamp for 5 min. Next, the reservoir was peeled off and the receiving paper was washed five times with PBST. Finally, the colorimetric signal was measured immediately afterward with a densitometry app

as explained below. Bacterial suspensions in PBS containing *P. aeruginosa* (PAO1 strain) were used as samples for calibrating the immunosensors. The suitability of the proposed method for detecting pathogens in real patient samples was tested with a panel of sputum samples obtained from the Microbiology Unit at Son Espases University Hospital with approval from the local ethics committee (protocol IB 4005/19 PI).

7.3.4 Densitometry App

App development has been described elsewhere [188]. It was installed in a Huawei POT-LX1 smartphone. To quantify signals, the user aligns the square piece of paper with a virtual frame. This fixes the distance and angle of the smartphone with respect to the assay. After pressing "set," the app automatically finds the region of interest and quantifies the increase of pixel intensity with respect to the background. Compensation for different illuminance and uneven illumination conditions is calculated automatically. When the app has performed 50 valid measurements, the screen displays the average value. The process takes less than 10 s. **Fig S8 appx 4** shows a comparison between the app and a manual method for densitometric analysis using a scanner and image processing software ImageJ.

7.3.5 Data Analysis.

Statistical analysis was performed using GraphPad Prism software. Data are expressed as mean ± standard deviation (SD) or median with the 25th and 75th percentile. The Kruskal−Wallis test was used to compare values of biomass and bacterial membrane permeability among differently treated biofilms or values of immunosensor signals among different sputum samples. A P value<0.05 was considered statistically significant.

7.4 Results

Our method for the rapid detection of *P. aeruginosa* in respiratory samples is based on the generation of bubbles by the enzyme catalase, which liquefies the sample (**Fig. 7.1**A). Microparticles have been previously used for mechanically disrupting sputum samples.[227] We hypothesized that oxygen bubbles could have a similar effect without using mixers to stir the sample. Since the catalase is produced by *P. aeruginosa*, and bacteria are trapped within the biofilm, we envisioned that the bubbles would not only liquefy the sputum but also disrupt the biofilm simultaneously. To study whether oxygen bubbles could liquefy sputum, 10 mg of sputum samples containing *P.aeruginosa* (PA+) or a mixed flora (MF) were introduced in an Eppendorf tube and treated with 200 µL of 0.3 M H_2O_2. In Video S7.1 (Liquefaction of sputum containing *P. aeruginosa* by H2O2), PA+ samples generate bubbles

that liquefy the sample within 60 s. The sample looks transparent after dispersing the bubbles (**Fig. 7.2**A), which shows that it has been completely liquefied. Mixed flora samples also generate bubbles, although more slowly, which indicates that they contain fewer catalase enzymes (Video S7.2 Liquefaction of sputum containing mixed flora by H_2O_2). Samples still contain dark spots 60 s after the addition of hydrogen peroxide, which indicates that they are not fully liquefied. To demonstrate that the bubbles are generated by catalase, the sputum containing *P. aeruginosa* was pretreated with different concentrations of a catalase inhibitor (NaN_3). In Videos S7.3−S7.5, samples incubated with NaN_3 generate fewer bubbles as the concentration of inhibitor increases.

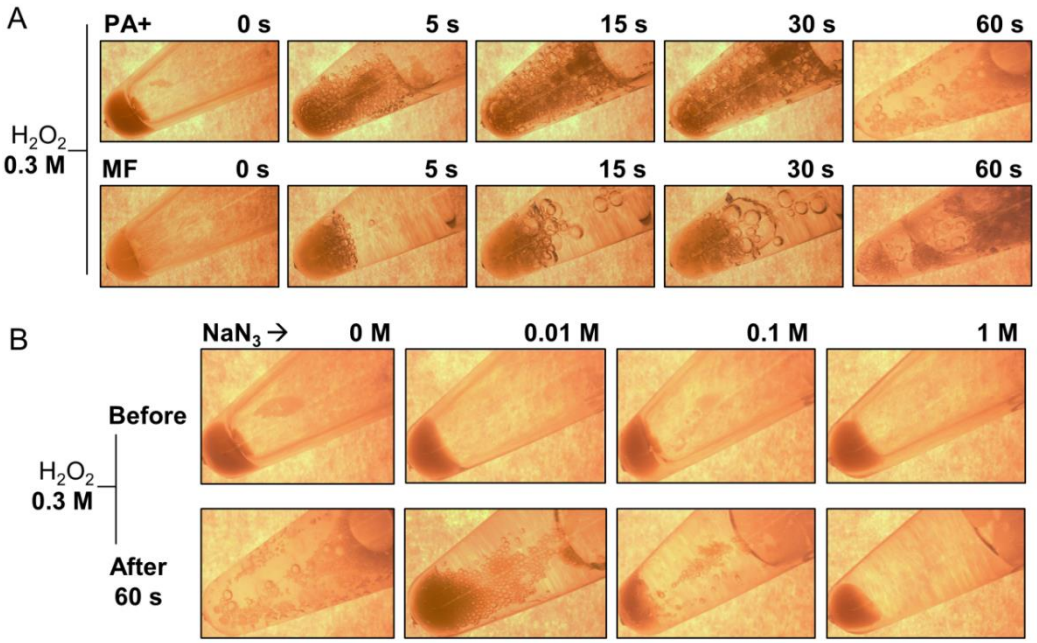

Fig. 7.2*Sputum liquefaction. (A) Photographs of sputum samples (10 mg) containing P. aeruginosa (PA+) or a mixed flora (MF) before (0 s) and after the addition of 0.3 M H_2O_2 for 5, 15, 30m, or 60 s. (B) Photographs of PA+ sputum samples pretreated with different concentrations of NaN_3 before and 60 s after the addition of 0.3 M H_2O_2.*

In **Fig. 7.2**B, samples appear opaque and unchanged by the addition of hydrogen peroxide when pretreated with NaN_3. These experiments demonstrate that the bubbles are generated by the catalase-mediated hydrolysis of H_2O_2. They also indicate that the main factor behind sample liquefaction is the enzymatic generation of bubbles since samples that do not generate these bubbles remain solid after the addition of hydrogen peroxide (**Fig. 7.2**B, 1 M NaN_3). Next, we studied whether the hydrogen peroxide treatment could disrupt the biofilms and liberate bacterial antigens. To this end, *P. aeruginosa* biofilms were grown at the bottom of a 96-well plate. After washing away excess planktonic cells while keeping the suspended aggregates or flocs untouched, H_2O_2 was added at different concentrations and the

generation of bubbles was recorded for 60 s (**Fig. 7.3**A). Biofilm disruption was documented by taking a photograph before and after the treatment (**Fig. 7.3**B). In **Fig. 7.3**A, samples without H_2O_2 did not generate any bubbles, and micrographs of the biofilms in **Fig. 7.3**B showed that they were mainly unaltered. When the concentration of H_2O_2 was higher than 0.01 M, samples started to effervesce. As the concentration of H_2O_2 increased, the amount and size of the generated bubbles also increased (**Fig. 7.3**A). In **Fig. 7.3**B, images look less opaque when the concentration of H_2O_2 increased because the biofilm flocs were being dissolved. Densitometric analysis of the images shown in **Fig. 7.3**B confirmed this trend (**Fig. 7.3**C).

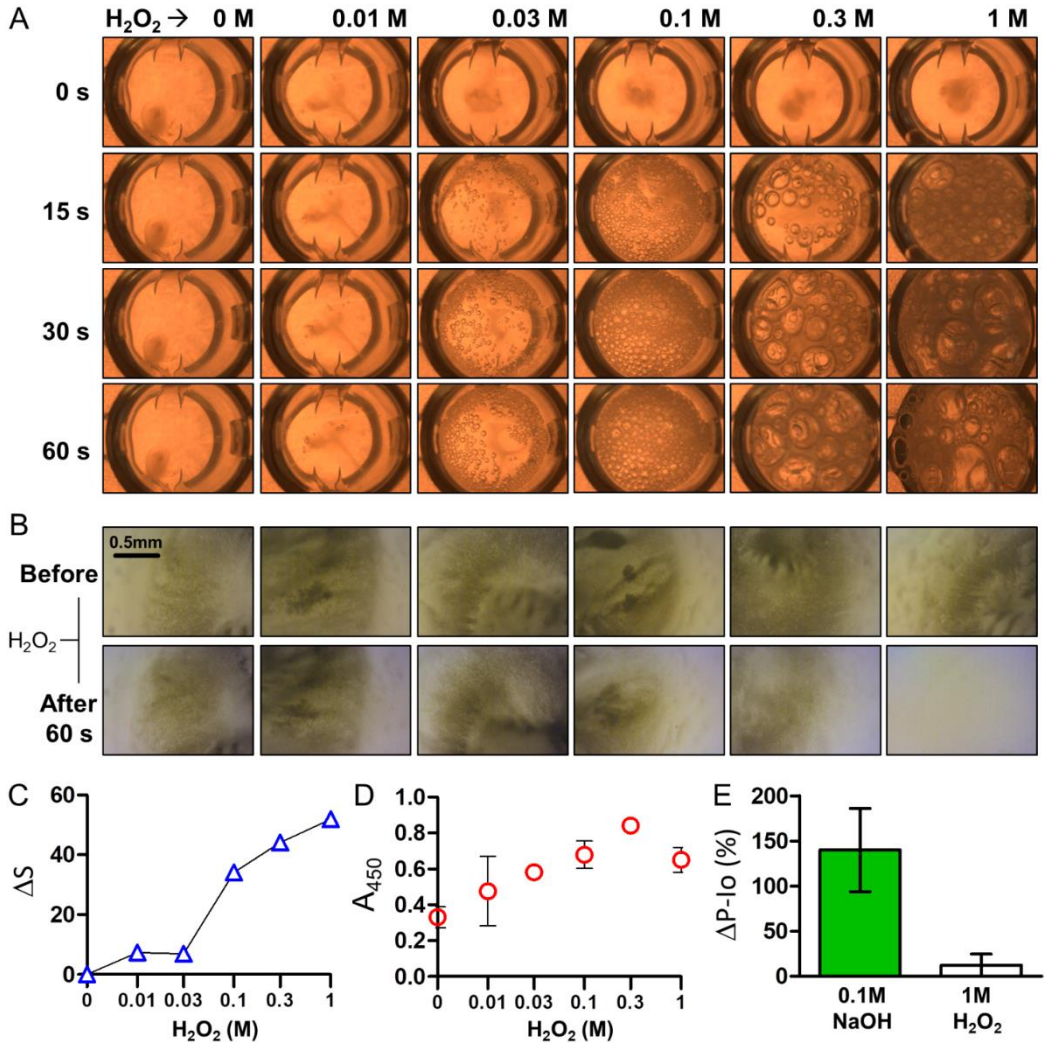

Fig. 7.3*Biofilm disruption. (A) Photographs of P. aeruginosa biofilms grown in a 96-well plate before and after adding H_2O_2 at different concentrations for 0, 15, 30, and 60 s. (B) Micrographs of the biofilms before and 60 s after adding H_2O_2 at the concentrations shown in (A). (C) Increase in the colorimetric signal (illuminance, ΔS) calculated from micrographs in (B). (D) Detection of bacterial antigens released from biofilms attached to the plate after adding H_2O_2 at different concentrations for 60 s; error bars are the standard deviation (n = 6). (E) Percentage increase of propidium iodide (P-Io) fluorescence intensity (cell death) after adding 1 M H_2O_2 (white*

bar) or 0.1 M NaOH (green bar) as a positive control for 60 s. Bars represent the mean value, and error bars are the standard deviation (n = 5).

In **Fig. 7.4**A, confocal 3D images of biofilms show intense fluorescent signals and accurate colocalization of SYTO9 (green) and ConA-TRIC (red) dyes (**Fig. 7.4**A(i,ii)), indicating a dense biomass encrusted in the EPS matrix. After addition of 0.3 M H_2O_2, both signals drastically decrease (**Fig. 7.4**A(iii,iv)), which demonstrates a deep disruption of the biofilm architecture (cells and substances surrounding them). In **Fig S4 appx 4**, confocal 3D images show that despite biofilm disruption the cell viability is conserved, confirming the fact that biofilm disruption is predominantly caused by the generation of bubbles and not by the biocide action of H_2O_2. To further demonstrate that the catalase-induced generation of bubbles is key for biofilm disruption, the same experiments were repeated with biofilms grown in the presence of an Fe chelator, which diminishes catalase activity and reduces the production of bubbles [237]. In **Fig. 7.4**B, confocal 3D images of Fe-starved biofilms show that both green and red signals (**Fig. 7.4**B(iii,iv)) are similar to those observed before the addition of H_2O_2 (**Fig. 7.4** (i,ii)). This means that the biofilm architecture is much less altered than that in **Fig. 7.4**A, even though the cells are less protected from the biocide action of H_2O_2 (catalase activity is lower) and generate less EPS (the red signal is less intense than that in **Fig. 7.4**A). These results demonstrate that the generation of bubbles is the main factor behind biofilm disruption induced by H_2O_2 (**Fig. 7.4**B(i,iii) and **Fig S4 appx 4**) regardless of the amount of protective EPS (**Fig. 7.4**B(ii−iv)).

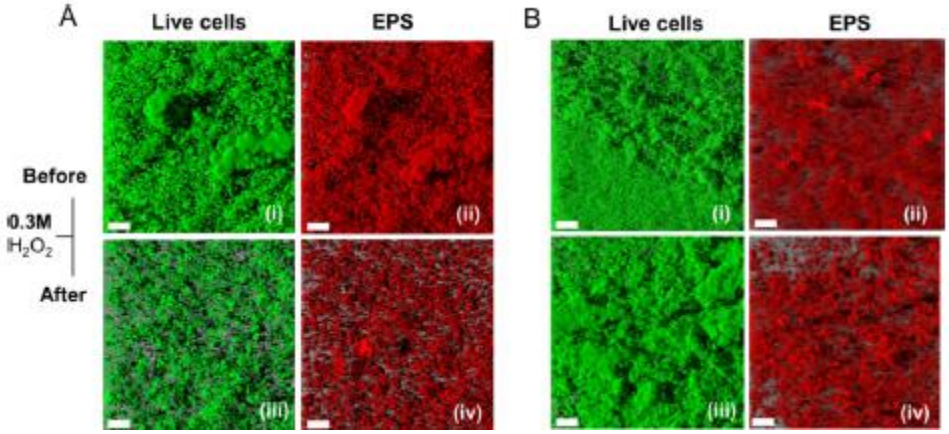

Fig. 7.4*Live cells and extracellular polymeric substances in P. aeruginosa biofilms after H_2O_2 treatment. (A) Three-dimensional confocal imaging before (i, ii) and after (iii, iv) 0.3 M H_2O_2 treatment in control biofilms or (B) biofilms with low catalase activity grown in the presence of an Fe chelator (0.25 mM 2-2'-bipyridyl) for 48 h. Green (SYTO9) and red (ConA-TRIC) colors indicate the presence of live cells and extracellular polymeric substances (EPS), respectively. Scale bar: 15 µm.*

To demonstrate that H_2O_2 can induce the release of bacteria from the biofilms attached to the plate, we first washed away excess planktonic cells and flocs and added H_2O_2 at different

concentrations. Then, supernatants were collected at different times and analyzed with ELISA using the method shown in **Fig S1 appx 4**. In **Fig. 7.3**D, the ELISA signal increased as the concentration of H_2O_2 increased, which indicates that bacterial antigens were found at higher concentrations in the supernatants after the treatment. This further supports the hypothesis that pathogens were liberated from the biofilm due to the generation of bubbles. The ELISA signal slightly decreased when the concentration of H_2O_2 was 1 M, even though the biofilms seem to be completely dissolved in **Fig. 7.3**B,C. Supplementary experiments showed that the addition of H_2O_2 interfered with antibody−antigen interactions when supplied at 1 M (**Fig S2 appx 4**), which explained the decrease in signal seen in **Fig. 7.1**D. Increasing the incubation time with H_2O_2 to 3 or 5 min resulted in more bacterial antigens being released from the biofilms at low concentrations of hydrogen peroxide, but the maximum signal at 0.3 M remained unaffected (**Fig S3 appx 4**). Consequently, a H_2O_2 concentration of 0.3 M and an incubation time of 60 s were chosen for subsequent experiments, since these conditions completely liquefied sputum samples (Figure 2) and liberated antigens from biofilms (**Fig. 7.3**D) without hampering immunodetection to a large extent (**Fig S2 appx 4**). Hydrogen peroxide can induce intracellular production of highly reactive hydroxyl free radicals that could compromise membrane permeability.[238] In **Fig. 7.3**E, a cell viability test showed that the membrane permeability of *P. aeruginosa* cells was not affected by the addition of H_2O_2 with a concentration as high as 1 M when it was added for only 60 s. This indicates that the ELISA signals recorded in Figure 3D originated from biofilm disruption, which was mainly caused by the generation of bubbles, and that the biocide action of H_2O_2 plays a less relevant role when added at 0.3 M for only 60 s. This was also confirmed by confocal 3D imaging of biofilms after live/dead staining (**Fig S4 appx 4**). Biofilms grown under Fe starvation conditions generated fewer bubbles and released fewer antigens upon treatment with hydrogen peroxide (**Fig S5 appx 4** and **Fig S6 appx 4**). This experiment corroborated the evidence that the production of catalase by the pathogens was the key factor behind the effervescence and antigen release shown in **Fig. 7.3**.

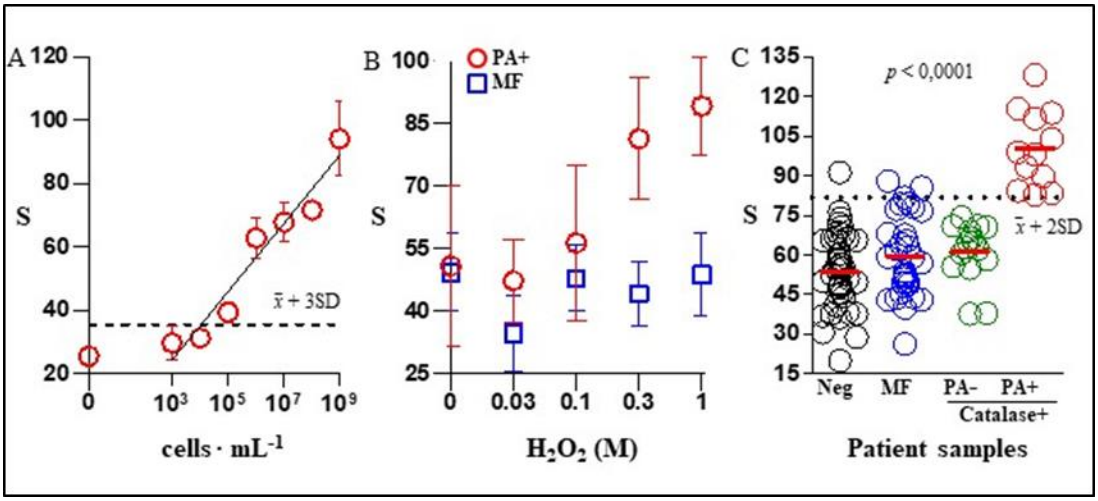

Fig. 7.5*Detection of P. aeruginosa with the mobile immunosensors shown in* ***Fig. 7.1****B in solutions containing bacteria at known concentrations (A), in sputum samples classified as infected by the pathogen (PA+) or containing a mixed flora (MF) after addition of H_2O_2 at different final concentrations (B), and in a panel of patient samples (C). Error bars are the standard deviation (n = 3). X is the average and SD is the standard deviation. In (A), the dotted line shows signals above three times the standard deviation of the blank. In (C), PA+ samples contain P. aeruginosa (>10^5 cells·mL^{-1}, red), PA− samples contain catalase+ bacteria different from P. aeruginosa (>10^5 cells·mL^{-1}, green), and MF contains a mixed flora (blue). Negative samples for bacterial infection were determined by a Gram's stain screening test (black). Horizontal bars represent the mean. The dotted line shows signals above two times the standard deviation of the negative samples. P-value was obtained using a Kruskall−Wallis test.*

After demonstrating the enzymatic rupture of biofilms and concomitant liquefaction of sputum samples, we sought to apply this method for the rapid detection of respiratory infection by *P. aeruginosa*. To accomplish this, we combined it with a mobile immunosensor for the rapid detection of bacteria developed in our laboratory and schematized in **Fig. 7.1**B. First, we calibrated the immunosensor with bacterial suspensions of known concentration. In **Fig. 7.5**A and **Fig S8 appx 4**, the signal S increased as the concentration of *P. aeruginosa* increased linearly in the concentration range between 10^4 and 10^9 cells·mL^{-1}. The limit of detection, expressed as the sample that yields a signal higher than three times the standard deviation of the blank, was 10^5 cells·mL^{-1}, which is the clinical threshold value for respiratory infections. Next, we studied whether the immunosensor was compatible with the sample liquefaction method and whether the matrix could interfere in the detection of *P. aeruginosa*. To test this, a sputum sample from a patient suffering from an infection by *P. aeruginosa* and a sample containing a mixed flora were fractioned and treated with different concentrations of hydrogen peroxide for 60 s. In **Fig. 7.5**B, samples that were treated only with PBS (0 M H_2O_2) could not be differentiated with the immunosensor because bacteria in the sample were still trapped in the matrix, in accordance with our initial hypothesis. As the concentration of H_2O_2 increased, the signal S also increased because more antigens were being released from the matrix and the biofilm, in accordance with the results shown in **Fig.**

7.2 and **Fig. 7.3**. These results also demonstrate the excellent specificity of our detection kit, which can differentiate an infection by *P. aeruginosa* from a sample containing a mixed flora in a biological matrix as complex as sputum.

To further support this point, a panel of sputum samples that were either positive or negative for infection by *P. aeruginosa*, as well as samples classified as mixed flora, was tested. The method here consisted of a 60 s liquefaction step, followed by immunodetection with mobile biosensors within 7 min. In **Fig. 7.5**C, all samples classified as a respiratory infection by *P. aeruginosa* yielded a signal two times above the standard deviation of the average value of negative samples. Using this criterion, only one negative sample out of 44 was incorrectly classified as positive. Furthermore, only two out of 32 mixed flora samples yielded a false-positive result. All 16 samples infected with other catalase-producing pathogens were also correctly classified as negative, which demonstrates that higher signals obtained in samples containing *P. aeruginosa* originated from the specific recognition of bacterial antigens, and not from differences in sample liquefaction. The test diagnostic sensitivity (true-positive rate) is 100%, and the specificity (true-negative rate) is 96.7%. While further experiments with a larger cohort of patient samples should be performed to establish the diagnostic sensitivity and specificity, our preliminary results indicate that the proposed method is suitable for the rapid identification of respiratory infections by *P. aeruginosa* at the point of care.

7.5 Discussion

The routine method for treating sputum samples prior to pathogen detection through bacteriological culture involves the addition of dithiothreitol (DTT), which reduces disulfide bonds that cross-link mucins in the matrix. This usually requires adding DTT for at least 30 min in a temperature controlled bath, followed by sample dispersion with a vortex.

In contrast, our enzymatic method generates bubbles that disrupt biofilms (**Fig. 7.3**, **Fig. 7.4**, and **Fig S4 appx 4**) and liquefy the sample (**Fig. 7.2** and **Fig S9 appx 4**) within 60 s. The bubbles are generated via the enzymatic conversion of hydrogen peroxide (**Fig. 7.2**B, **Fig S5 appx 4**, and **Fig S6 appx 4**), which does not reduce disulfide bonds to a large extent (**Fig S7 appx 4**). The proposed method for detecting bacterial biofilms has some notable strengths and limitations compared to the DTT method. For example, our method is more advantageous for point-of-care measurements because it is faster and requires less equipment than the DTT protocol. However, samples that do not contain catalase-producing cells may not be completely liquefied with the H_2O_2 method (**Fig S9 appx 4**). This is

advantageous in the context of *P. aeruginosa* detection because samples that are not liquefied will not release potential interferents. In other words, our method improves the selectivity toward *P. aeruginosa* detection because pathogens that do not produce catalase will remain trapped in the matrix. Another potential limitation is that adding hydrogen peroxide for extended periods of time will kill the cells and therefore these will not grow under standard bacterial culture procedures. However, it could expedite the detection of pathogens when coupled with methods that do not require viable cells, for example, for PCR analysis or immunodetection. Finally, it should be noted that polyclonal antibodies may not be able to distinguish between different bacteria from the Pseudomonas genus. However, the prevalence of infections due to bacteria other than *P. aeruginosa* is so low that its impact on clinical diagnosis would be minimum [239].

7.6 Conclusions

In this paper, we introduce a method for disrupting biofilms of *P. aeruginosa* and liquefying respiratory samples in one step. It only requires adding a solution of hydrogen peroxide. The formation of oxygen bubbles by catalase is the key factor for dispersing the matrix and the cells. The release of antigens from the sample allowed us to detect *P. aeruginosa* in sputum samples with a rapid diagnostic test made of paper that utilizes a smartphone as a reader. The whole process, including sample liquefaction and pathogen detection, took less than 8 min. This rapid turnaround time makes the detection kit an ideal method to screen for hospital-acquired respiratory infections that may lead to sepsis.

8 DISCUSSION

The combination of the findings presented in this thesis has resulted in the development of a new and versatile technology to produce paper biosensors based on nanomaterials that allows to overcome the limitations of traditional paper biosensors. As a first step, some key aspects of the biosensor design and fabrication were optimized. Several surface functionalization and bioconjugation strategies were tested to improve the manufacture of plasmonic nanoprobes decorated with proteins. On the one hand, an amidation reaction between avidin and carboxylate-coated AuNPs was carried out. Since this reaction is pH-dependent, avidin solutions at different pH were used. The resulting avidin-decorated nanoprobes were tested and the highest signals were obtained when the reaction was performed at pH 6.5. On the other hand, a crosslinking reaction between avidin and amine- or PVP-coated nanoparticles was carried out at different times, using glutaraldehyde as a crosslinker. The resulting nanoprobes were tested and amine-coated nanoparticles yielded the highest signal when the reaction occurred for 1 h, whereas PVP-coated nanoparticles required 3 h to yield the same result.

Next, in order to evaluate the role of the paper surface charge in attaching capture biomolecules, paper substrates were treated with a positive charged polymer PAH, either alone or followed by the addition of negatively charged PSS. Best results were obtained with biosensors combining carboxylate-coated nanoparticles biofunctionalized by amidation and unmodified paper substrates. Therefore, this design was used for the following applications. Once the best conditions were established, the device was implemented to detect the sepsis biomarker IL-6. IL-6 was detected in PBS with a limit of detection of 0.1 $pg \cdot mL^{-1}$. Then, an increase in IL-6 of only 12.5 $pg \cdot mL^{-1}$ over basal levels was detected with 99% confidence in a spiked blood sample from a healthy donor. The total assay time was 17 min.

A AuNPs reservoir made of filter paper modified with the polymer PSS was developed in order to overcome the difficulty of storing nanoparticles on plain paper substrates. To achieve this, several filter papers with 3 different pore sizes were treated with increasing concentrations of PSS. Using 22 µm pore size filter paper and PSS at 30% v/v, irreversible reactions between nanoparticles and the paper matrix were completely avoided. Nanoparticles in the reservoir could be transferred with high efficiency to a receiving wet paper. Once transferred, the AuNPs do not diffuse away and nanoprobes keep their color and their bio-recognition ability. This reservoir technology was implemented in each of the

next applications. For instance, glycoprotein B from human cytomegalovirus spiked in serum samples was detected utilizing a paper biosensor with a reservoir integrated in it. In this approach, a low limit of detection of 0.03 $ng \cdot mL^{-1}$ was obtained with a total assay time of only 12 minutes.

A signal amplification strategy developed in a previous project [20] was implemented in all applications described here. It does not require the use of labile reagents and/or additional steps. It consists of performing the assay on a folded piece of filter paper. As the analyte is on the 3 layers of the folded paper strip, a single drop of detection antibody will pass through the layers and will react with the analytes on them, generating a colorimetric signal on each layer. When the paper strip is wet and still folded, it is possible to see an intense signal made of those three signals stacked on top of each other.

In order to reduce assay steps and time without losing specificity, the sandwich format used in the last two applications was replaced by a reverse phase format [240]. In this format, the sample is added to the paper strip and dried with a hair drier for 30 s. Then, the analyte is detected by using specific antibodies decorated AuNPs. Replacing the capture antibody for the absorption and dry on paper substrate, reduces the assay time at least in 5 min. By implementing the reservoir and the new immunoassay format, the total assay time was reduced to 10 min.

Finally, by applying all optimized conditions explained above, a new paper biosensor design was developed and tested. The improved paper immunosensors were able to rapidly detect either pathogens such as *Pseudomonas aeruginosa* or sepsis biomarkers as interleukin-6 in real samples from patients. In the case of the IL-6 levels detected in blood and BAS samples from COVID-19 patients, the stratification of the patients according to severity was possible. Additionally, thanks to the amplification system employed, the limit of detection decreased down to 10^{-3} $pg \cdot mL^{-1}$, improving the one obtained on the first application mentioned at the beginning of the discussion. At the same time, the low limit of detection allows to detect IL-6 in diluted complex matrices. It was possible to apply respiratory samples such as sputum and BAS to the immunosensors, thanks to the fact that they were previously liquefied. The liquefaction method relied on using the endogenous catalase from respiratory samples. Catalase reacted with hydrogen peroxide to produce oxygen bubbles that mechanically disrupted the mucin network within respiratory samples. Once the sample is liquid, it can be analyzed by using the paper-based immunosensor developed here or ELISA [241]. Regarding the detection of *Pseudomonas aeruginosa* (PA), the limit of detection was

10^5 cells·mL^{-1}, which is the clinical threshold value for diagnosing an infection. Additionally, samples positive for PA were differentiated from negative samples, mixed flora samples and even from samples positive caused by other catalase-producing pathogens.

9 FINAL CONCLUSIONS

This thesis involves the development of a complete detection platform that includes a disposable biosensor made entirely of paper and a real time reader based on a smartphone app. Regarding the paper biosensor design, several of its components were optimized. Among them, the biofunctionalization reaction of the nanoprobes, the sample pre-conditioning, the storing of AuNPs on paper substrates and the total assay time were fine-tuned. Due to these optimizations, the final biosensor design is a versatile technology able to detect both pathogens and proteins in different real samples and within a few minutes. These properties make these biosensors excellent candidates for guiding medical decisions during the management of septic patients.

This platform could be easily adapted to detect other analytes by changing the antibodies decorating the nanoparticles accordingly. For example, with regards to cytokines, this platform can be adapted to detect TNF-α and IL-8, which are also common biomarkers of inflammation. The ability of detecting cytokines in blood and respiratory samples paves the way for monitoring local inflammation in the lungs as well as systemic inflammation levels in the body. On the other hand, adapting this platform, it is also possible to detect other pathogens causing infections. For example, in already liquid matrices like urine it is possible to detect urinary tract infections caused by *E. coli* [39] or by *Klebsiella pneumoniae* [242]. Having said that, this technology could be the basis for future biosensors able to detect several analytes at the same time in the same sample, since it is uncomplicated to increase the number of reservoirs within the same paper sensor.

REFERENCES

1. Mohanty SP, Koucianos E (2006) Biosensors: A tutorial review. IEEE Potentials 25:35–40. https://doi.org/10.1109/MP.2006.1649009

2. Monošík R, Streďanský M, Šturdík E (2012) Biosensors - classification, characterization and new trends. Acta Chim Slovaca 5:109–120. https://doi.org/10.2478/v10188-012-0017-z

3. Ravidra NM, Prodan C, Fnu S, et al (2007) Advances in the manufacturing types, and applications of biosensors. Jom 59:37–43. https://doi.org/10.1007/s11837-007-0150-0

4. Charoenkitamorn K, Yakoh A, Jampasa S, Chaiyo S (2020) Electrochemical and optical biosensors for biological sensing applications. 46:245–253

5. Karunakaran C, Rajkumar R, Bhargava K (2015) Introduction to Biosensors. Biosens Bioelectron 1–68. https://doi.org/10.1016/B978-0-12-803100-1.00001-3

6. Burcu E, Kemal M (2015) Applications of commercial biosensors in clinical , food , environmental , and biothreat / biowarfare analyses Commercial Biosensors. 478:107–120. https://doi.org/10.1016/j.ab.2015.03.011

7. Bahadır EB, Sezgintürk MK (2015) Applications of commercial biosensors in clinical, food, environmental, and biothreat/biowarfare analyses. Anal Biochem 478:107–120. https://doi.org/10.1016/j.ab.2015.03.011

8. Liu J, Mattiasson B (2002) Microbial BOD sensors for wastewater analysis. Water Res 36:3786–3802. https://doi.org/10.1016/S0043-1354(02)00101-X

9. Cabezas VGREGIORGLG (2005) Aplicaciones de los biosensores en la industría agroalimentaria

10. Madrid RE, Chehín R, Chen T-H, Guiseppi-Elie A (2017) Biosensors and Nanobiosensors. 391–462. https://doi.org/10.1142/9789813147263_0011

11. Yusoff N, Pandikumar A, Ramaraj R, et al (2015) Gold nanoparticle based optical and electrochemical sensing of dopamine. Microchim Acta 182:2091–2114. https://doi.org/10.1007/s00604-015-1609-2

12. Mehrotra P (2016) Biosensors and their applications - A review. J Oral Biol Craniofacial Res 6:153–159. https://doi.org/10.1016/j.jobcr.2015.12.002

13. Li J, Stachowski M, Zhang Z (2015) Application of responsive polymers in implantable medical devices and biosensors. In: Switchable and Responsive Surfaces and Materials for Biomedical Applications, 1st ed. Elsevier, pp 259–298

14. Cooper MA (2002) Optical biosensors in drug discovery. Nat Rev Drug Discov 1:515–528. https://doi.org/10.1038/nrd838

15. Pohanka M (2018) Overview of piezoelectric biosensors, immunosensors and DNA sensors and their applications. Materials (Basel) 11:. https://doi.org/10.3390/ma11030448

16. Manz A, Danielsson B, Danielsson B, et al 38 Thermal Biosensor and Microbiosensor Techniques Related papers Thermal Biosensor and Microbiosensor Techniques

17. Damborský P, Švitel J, Katrlík J (2016) Optical biosensors. Essays Biochem 60:91–100. https://doi.org/10.1042/EBC20150010

18. Chen C, Wang J (2020) Optical biosensors: An exhaustive and comprehensive review. Analyst 145:1605–1628. https://doi.org/10.1039/c9an01998g

19. Nguyen QH, Kim M Il (2020) Nanomaterial-mediated paper-based biosensors for colorimetric pathogen detection. TrAC - Trends Anal Chem 132:116038. https://doi.org/10.1016/j.trac.2020.116038

20. Alba-Patiño A, Russell SM, de la Rica R (2018) Origami-enabled signal amplification for paper-based colorimetric biosensors. Sensors Actuators B Chem 273:951–954. https://doi.org/https://doi.org/10.1016/j.snb.2018.07.019

21. Parolo C, Medina-Sánchez M, de la Escosura-Muñiz A, Merkoçi A (2013) Simple paper architecture modifications lead to enhanced sensitivity in nanoparticle based lateral flow immunoassays. Lab Chip 13:386–390. https://doi.org/10.1039/C2LC41144J

22. Parolo C, Sena-Torralba A, Bergua JF, et al (2020) Tutorial: design and fabrication of nanoparticle-based lateral-flow immunoassays. Nat Protoc 15:3788–3816. https://doi.org/10.1038/s41596-020-0357-x

23. Wei P, Ning Z, Ye S, et al (2018) Impact analysis of temperature and humidity conditions on electrochemical sensor response in ambient air quality monitoring. Sensors (Switzerland) 18:. https://doi.org/10.3390/s18020059

24. Madou MJ (2018) Fundamentals of Microfabrication and Nanotechnology, 3rd ed. CRC Press

25. Zhu D, Liu B, Wei G (2021) Two-dimensional material-based colorimetric biosensors: A review. Biosensors 11:. https://doi.org/10.3390/bios11080259

26. Choudhury S (2020) Molecular tools for the detection of waterborne pathogens. In: Waterborne Pathogens, 1st ed. Elsevier, pp 219–235

27. Singh AT, Lantigua D, Meka A, et al (2018) Paper-based sensors: Emerging themes and applications. Sensors (Switzerland) 18:1–22. https://doi.org/10.3390/s18092838

28. Mahato K, Purohit B, Kumar A (2020) Paper-based biosensors for clinical and biomedical applications : Emerging engineering concepts and challenges, 1st ed. Elsevier B.V.

29. Mahato K, Srivastava A, Chandra P (2017) Paper based diagnostics for personalized health care: Emerging technologies and commercial aspects. Biosens Bioelectron 96:246–259. https://doi.org/10.1016/j.bios.2017.05.001

30. Kuswandi B, Ensafi AA (2020) Perspective—Paper-Based Biosensors: Trending Topic in Clinical Diagnostics Developments and Commercialization. J Electrochem Soc 167:037509. https://doi.org/10.1149/2.0092003jes

31. Hristov DR, Rodriguez-Quijada C, Gomez-Marquez J, Hamad-Schifferli K (2019) Designing paper-based immunoassays for biomedical applications. Sensors (Switzerland) 19:. https://doi.org/10.3390/s19030554

32. Credou J SIMPLE, BIOCOMPATIBLE AND ROBUST MODIFICATION OF

CELLULOSE MEMBRANES FOR THE ECO 2-FRIENDLY PREPARATION OF IMMUNOASSAY DEVICES

33. Park J, Shin JH, Park JK (2016) Pressed Paper-Based Dipstick for Detection of Foodborne Pathogens with Multistep Reactions. Anal Chem 88:3781–3788. https://doi.org/10.1021/acs.analchem.5b04743

34. Mahmoudinobar F, Britton D, Montclare JK (2021) Protein-based lateral flow assays for COVID-19 detection. Protein Eng Des Sel 34:1–10. https://doi.org/10.1093/protein/gzab010

35. Shariati S, Khayatian G (2021) Microfluidic nanopaper based analytical device for colorimetric and naked eye determination of cholesterol using the color change of triangular silver nanoprisms. New J Chem 45:21788–21794. https://doi.org/10.1039/d1nj04458c

36. Russell SM, Alba-Patiño A, Borges M, de la Rica R (2018) A Robust and User-Friendly Alternative to Densitometry Using Origami Biosensors and Digital Logic. ACS sensors 3:1712–1718. https://doi.org/10.1021/acssensors.8b00452

37. Vaquer A, Barón E, de la Rica R (2021) Detection of low glucose levels in sweat with colorimetric wearable biosensors. Analyst 146:3273–3279. https://doi.org/10.1039/D1AN00283J

38. Vaquer A, Barón E, de la Rica R (2021) Wearable Analytical Platform with Enzyme-Modulated Dynamic Range for the Simultaneous Colorimetric Detection of Sweat Volume and Sweat Biomarkers. ACS sensors 6:130–136. https://doi.org/10.1021/acssensors.0c01980

39. Adrover-Jaume C, Rojo-Molinero E, Clemente A, et al (2020) Mobile origami immunosensors for the rapid detection of urinary tract infections. Analyst 145:7916–7921. https://doi.org/10.1039/d0an01218a

40. Arduini F, Cinti S, Caratelli V, et al (2019) Origami multiple paper-based electrochemical biosensors for pesticide detection. Biosens Bioelectron 126:346–354. https://doi.org/10.1016/j.bios.2018.10.014

41. Liu H, Crooks RM (2011) Three-Dimensional Paper Microfluidic Devices Assembled Using the Principles of Origami. J Am Chem Soc 133:17564–17566. https://doi.org/10.1021/ja2071779

42. Chen CA, Yeh WS, Tsai TT, et al (2019) Three-dimensional origami paper-based device for portable immunoassay applications. Lab Chip 19:598–607. https://doi.org/10.1039/C8LC01255E

43. Aldewachi H, Chalati T, Woodroofe MN, et al (2018) Gold nanoparticle-based colorimetric biosensors. Nanoscale 10:18–33. https://doi.org/10.1039/c7nr06367a

44. Yeh Y-C, Creran B, Rotello VM (2012) Gold nanoparticles: preparation, properties, and applications in bionanotechnology. Nanoscale 4:1871–1880. https://doi.org/10.1039/C1NR11188D

45. Glomm WR (2005) Functionalized gold nanoparticles for applications in bionanotechnology. J Dispers Sci Technol 26:389–414. https://doi.org/10.1081/DIS-200052457

46. Rivas L, de la Escosura-Muñiz A, Pons J, Merkoçi A (2014) Lateral Flow Biosensors Based on Gold Nanoparticles. In: Comprehensive Analytical Chemistry, 1st ed. Elsevier B.V., pp 569–605

47. Elahi N, Kamali M, Baghersad MH (2018) Recent biomedical applications of gold nanoparticles: A review. Talanta 184:537–556. https://doi.org/10.1016/j.talanta.2018.02.088

48. Hu X, Zhang Y, Ding T, et al (2020) Multifunctional Gold Nanoparticles: A Novel Nanomaterial for Various Medical Applications and Biological Activities. Front Bioeng Biotechnol 8:1–17. https://doi.org/10.3389/fbioe.2020.00990

49. Nejati K, Dadashpour M, Gharibi T, et al (2021) Biomedical Applications of Functionalized Gold Nanoparticles: A Review. J Clust Sci 33:1–16. https://doi.org/10.1007/s10876-020-01955-9

50. Daruich De Souza C, Ribeiro Nogueira B, Rostelato MECM (2019) Review of the methodologies used in the synthesis gold nanoparticles by chemical reduction. J Alloys Compd 798:714–740. https://doi.org/10.1016/j.jallcom.2019.05.153

51. Pamies R, Cifre JGH, Espín VF, et al (2014) Aggregation behaviour of gold nanoparticles in saline aqueous media. J Nanoparticle Res 16:. https://doi.org/10.1007/s11051-014-2376-4

52. Villaverde G, Laurenti M, Rubio J, Contreras R (2021) Reducing Agents in Colloidal Nanoparticle Synthesis – an Introduction. In: Reducing Agents in Colloidal Nanoparticle Synthesis, 1st ed. The Royal Society of Chemistry, pp 1–27

53. Hermanson GT (2013) 14. Microparticles and Nanoparticles. In: Bioconjugate Techniques, Third Edit. Elsevier Inc, pp 549–587

54. Zhao P, Li N, Astruc D (2013) State of the art in gold nanoparticle synthesis. Coord Chem Rev 257:638–665. https://doi.org/https://doi.org/10.1016/j.ccr.2012.09.002

55. Gao Y, Torrente-Murciano L (2020) Mechanistic insights of the reduction of gold salts in the Turkevich protocol. Nanoscale 12:2740–2751. https://doi.org/10.1039/c9nr08877f

56. Meissner J, Prause A, Bharti B, Findenegg GH (2015) Characterization of protein adsorption onto silica nanoparticles: influence of pH and ionic strength. Colloid Polym Sci 293:3381–3391. https://doi.org/10.1007/s00396-015-3754-x

57. Qureshi A, Niazi JH (2020) Biosensors for detecting viral and bacterial infections using host biomarkers: A review. Analyst 145:7825–7848. https://doi.org/10.1039/d0an00896f

58. Luis Castillo-Henriquez, Mariana Brenes -Acuna, Arianna Castro-Rojas, Rolando Cordero-Salmeron ML-C and JRV-B (2020) Clinical Pathogens. 20:1–26

59. WHO (2022) Prioritizing diseases for research and development in emergency contexts. https://www.who.int/activities/prioritizing-diseases-for-research-and-development-in-emergency-contexts. Accessed 7 Jul 2022

60. Doron S, Gorbach SL (2008) Bacterial Infections: Overview. Int Encycl Public Heal 273. https://doi.org/10.1016/B978-012373960-5.00596-7

61. Mulani MS, Kamble EE, Kumkar SN, et al (2019) Emerging strategies to combat ESKAPE pathogens in the era of antimicrobial resistance: A review. Front Microbiol 10:. https://doi.org/10.3389/fmicb.2019.00539

62. Rice LB (2008) Federal funding for the study of antimicrobial resistance in nosocomial pathogens: no ESKAPE. J. Infect. Dis. 197:1079–1081

63. Physiology, Blood Plasma - StatPearls - NCBI Bookshelf. https://www.ncbi.nlm.nih.gov/books/NBK531504/#_NBK531504_pubdet_. Accessed 24 Mar 2022

64. Clemente A, Alba-Patiño A, Rojo-Molinero E, et al (2020) Rapid Detection of Pseudomonas aeruginosa Biofilms via Enzymatic Liquefaction of Respiratory Samples. ACS sensors 5:3956–3963. https://doi.org/10.1021/acssensors.0c01618

65. Sarigul N, Korkmaz F, Kurultak İ (2019) A New Artificial Urine Protocol to Better Imitate Human Urine. Sci Rep 9:20159. https://doi.org/10.1038/s41598-019-56693-4

66. Mach KE, Wong PK, Liao JC (2011) Biosensor diagnosis of urinary tract infections: a path to better treatment? Trends Pharmacol Sci 32:330. https://doi.org/10.1016/J.TIPS.2011.03.001

67. Alba Patiño A, Vaquer A, Barón E, et al (2022) Micro - and nanosensors for detecting blood pathogens and biomarkers at different points of sepsis care. Microchim Acta. https://doi.org/10.1007/s00604-022-05171-2

68. Dey P, Fabri-Faja N, Calvo-Lozano O, et al (2019) Label-free Bacteria Quantification in Blood Plasma by a Bioprinted Microarray Based Interferometric Point-of-Care Device. ACS sensors 4:52–60. https://doi.org/10.1021/acssensors.8b00789

69. Yuan K, Mei Q, Guo X, et al (2018) Antimicrobial peptide based magnetic recognition elements and Au@Ag-GO SERS tags with stable internal standards: a three in one biosensor for isolation, discrimination and killing of multiple bacteria in whole blood. Chem Sci 9:8781–8795. https://doi.org/10.1039/C8SC04637A

70. Sheini A (2021) A point-of-care testing sensor based on fluorescent nanoclusters for rapid detection of septicemia in children. Sensors Actuators B Chem 328:129029. https://doi.org/https://doi.org/10.1016/j.snb.2020.129029

71. Malsagova KA, Pleshakova TO, Galiullin RA, et al (2020) Nanowire Aptamer-Sensitized Biosensor Chips with Gas Plasma-Treated Surface for the Detection of Hepatitis C Virus Core Antigen. Coatings 10

72. Teengam P, Siangproh W, Tontisirin S, et al (2021) NFC-enabling smartphone-based portable amperometric immunosensor for hepatitis B virus detection. Sensors Actuators, B Chem 326:128825. https://doi.org/10.1016/j.snb.2020.128825

73. Murillo AMM, Tomé-Amat J, Ramírez Y, et al (2021) Developing an Optical Interferometric Detection Method based biosensor for detecting specific SARS-CoV-2 immunoglobulins in Serum and Saliva, and their corresponding ELISA correlation. Sensors Actuators, B Chem 345:. https://doi.org/10.1016/j.snb.2021.130394

74. Srisomwat C, Yakoh A, Avihingsanon A, et al (2022) An alternative label-free DNA sensor based on the alternating-current electroluminescent device for simultaneous detection of human immunodeficiency virus and hepatitis C co-infection. Biosens Bioelectron 196:113719. https://doi.org/https://doi.org/10.1016/j.bios.2021.113719

75. Kumar S, Tripathy S, Jyoti A, Singh SG (2019) Recent advances in biosensors for diagnosis and detection of sepsis: A comprehensive review. Biosens Bioelectron 124–125:205–215. https://doi.org/10.1016/j.bios.2018.10.034

76. Barichello T, Generoso JS, Singer M, Dal-Pizzol F (2022) Biomarkers for sepsis: more than just fever and leukocytosis—a narrative review. BioMed Central

77. Napolitano LM (2018) Sepsis 2018: Definitions and Guideline Changes. Surg Infect (Larchmt) 19:117–125. https://doi.org/10.1089/sur.2017.278

78. Bacterial Infections - Sepsis Alliance. https://www.sepsis.org/sepsisand/bacterial-infections/. Accessed 28 Jan 2022

79. Kataria Y, Remick D (2021) Sepsis biomarkers. Methods Mol Biol 2321:177–189. https://doi.org/10.1007/978-1-0716-1488-4_16

80. Fang Y, Hu Q, Yu X, Wang L (2018) Ultrasensitive electrochemical immunosensor for procalcitonin with signal enhancement based on zinc nanoparticles functionalized ordered mesoporous carbon-silica nanocomposites. Sensors Actuators B Chem 258:238–245. https://doi.org/https://doi.org/10.1016/j.snb.2017.11.062

81. Molinero-Fernández Á, Moreno-Guzmán M, Arruza L, et al (2019) Toward Early Diagnosis of Late-Onset Sepsis in Preterm Neonates: Dual Magnetoimmunosensor for Simultaneous Procalcitonin and C-Reactive Protein Determination in Diagnosed Clinical Samples. ACS sensors 4:2117–2123. https://doi.org/10.1021/acssensors.9b00890

82. Molinero-Fernández Á, López MÁ, Escarpa A (2020) An on-chip microfluidic-based electrochemical magneto-immunoassay for the determination of procalcitonin in plasma obtained from sepsis diagnosed preterm neonates. Analyst 145:5004–5010. https://doi.org/10.1039/D0AN00624F

83. Wu J, Chen Y, Yang M, et al (2017) Streptavidin-biotin-peroxidase nanocomplex-amplified microfluidics immunoassays for simultaneous detection of inflammatory biomarkers. Anal Chim Acta 982:138–147. https://doi.org/https://doi.org/10.1016/j.aca.2017.05.031

84. Nie R, Huang J, Xu X, Yang L (2020) A portable pencil-like immunosensor for point-of-care testing of inflammatory biomarkers. Anal Bioanal Chem 412:3231–3239. https://doi.org/10.1007/s00216-020-02582-z

85. Molinero-Fernández Á, Moreno-Guzmán M, Arruza L, et al (2020) Polymer-Based Micromotor Fluorescence Immunoassay for On-the-Move Sensitive Procalcitonin Determination in Very Low Birth Weight Infants' Plasma. ACS sensors 5:1336–1344. https://doi.org/10.1021/acssensors.9b02515

86. Guo J, Zhang J, Tian S, et al (2021) An up Conversion Optical System Based on Mesoporous Silica Encapsulated Up-Converting Nanoparticles Labeled Lateral Flow Immunoassay for Procalcitonin Quantification in Plasma. IEEE J Sel Top Quantum Electron 27:1–7. https://doi.org/10.1109/JSTQE.2021.3060496

87. Chen Y, Xianyu Y, Wu J, et al (2017) Double-Enzymes-Mediated Bioluminescent Sensor for Quantitative and Ultrasensitive Point-of-Care Testing. Anal Chem 89:5422–5427. https://doi.org/10.1021/acs.analchem.7b00239

88. Tanak AS, Muthukumar S, Krishnan S, et al (2021) Multiplexed cytokine detection

using electrochemical point-of-care sensing device towards rapid sepsis endotyping. Biosens Bioelectron 171:112726. https://doi.org/https://doi.org/10.1016/j.bios.2020.112726

89. Huang D, Ying H, Jiang D, et al (2020) Rapid and sensitive detection of interleukin-6 in serum via time-resolved lateral flow immunoassay. Anal Biochem 588:113468. https://doi.org/https://doi.org/10.1016/j.ab.2019.113468

90. Adrover-Jaume C, Alba-Patiño A, Clemente A, et al (2021) Paper biosensors for detecting elevated IL-6 levels in blood and respiratory samples from COVID-19 patients. Sensors Actuators B Chem 330:129333. https://doi.org/https://doi.org/10.1016/j.snb.2020.129333

91. Yin B, Zheng W, Dong M, et al (2017) An enzyme-mediated competitive colorimetric sensor based on Au@Ag bimetallic nanoparticles for highly sensitive detection of disease biomarkers. Analyst 142:2954–2960. https://doi.org/10.1039/C7AN00779E

92. Molinero-Fernández Á, Arruza L, López MÁ, Escarpa A (2020) On-the-fly rapid immunoassay for neonatal sepsis diagnosis: C-reactive protein accurate determination using magnetic graphene-based micromotors. Biosens Bioelectron 158:112156. https://doi.org/https://doi.org/10.1016/j.bios.2020.112156

93. Molinero-Fernández Á, López MÁ, Escarpa A (2020) Electrochemical Microfluidic Micromotors-Based Immunoassay for C-Reactive Protein Determination in Preterm Neonatal Samples with Sepsis Suspicion. Anal Chem 92:5048–5054. https://doi.org/10.1021/acs.analchem.9b05384

94. Molinero-Fernández Á, Moreno-Guzmán M, López MÁ, Escarpa A (2020) An array-based electrochemical magneto-immunosensor for early neonatal sepsis diagnostic: Fast and accurate determination of C-reactive protein in whole blood and plasma samples. Microchem J 157:104913. https://doi.org/https://doi.org/10.1016/j.microc.2020.104913

95. Boonyasit Y, Chailapakul O, Laiwattanapaisal W (2019) A folding affinity paper-based electrochemical impedance device for cardiovascular risk assessment. Biosens Bioelectron 130:389–396. https://doi.org/https://doi.org/10.1016/j.bios.2018.09.031

96. Lamas-Ardisana PJ, Loaiza OA, Añorga L, et al (2014) Disposable amperometric biosensor based on lactate oxidase immobilised on platinum nanoparticle-decorated carbon nanofiber and poly(diallyldimethylammonium chloride) films. Biosens Bioelectron 56:345–351. https://doi.org/https://doi.org/10.1016/j.bios.2014.01.047

97. Hashemzadeh S, Omidi Y, Rafii-Tabar H (2019) Amperometric lactate nanobiosensor based on reduced graphene oxide, carbon nanotube and gold nanoparticle nanocomposite. Microchim Acta 186:680. https://doi.org/10.1007/s00604-019-3791-0

98. Batra B, Narwal V, Pundir CS (2016) An amperometric lactate biosensor based on lactate dehydrogenase immobilized onto graphene oxide nanoparticles-modified pencil graphite electrode. Eng Life Sci 16:786–794. https://doi.org/https://doi.org/10.1002/elsc.201600082

99. Narwal V, Sharma M, Rani S, Pundir CS (2018) An ultrasensitive amperometric determination of lactate by lactate dehydrogenase nanoparticles immobilized onto Au electrode. Int J Biol Macromol 115:767–775.

https://doi.org/https://doi.org/10.1016/j.ijbiomac.2018.04.114

100. Huang Y-S, Chen K-Y, Cheng Y-T, et al (2020) An Inkjet-Printed Flexible Non-Enzymatic Lactate Sensor for Clinical Blood Plasma Test. IEEE Electron Device Lett 41:597–600. https://doi.org/10.1109/LED.2020.2973343

101. Li Q, Zhang Y, Fan H, et al (2021) In vitro and in vivo detection of lactate with nanohybrid-functionalized Pt microelectrode facilitating assessment of tumor development. Biosens Bioelectron 191:113474. https://doi.org/https://doi.org/10.1016/j.bios.2021.113474

102. Kaliva M, Vamvakaki M (2010) Materials Characterization. In: Materials Research Society Symposium Proceedings. Elsevier Inc., pp 401–433

103. Senthil Kumar P, Grace Pavithra K, Naushad M (2019) Characterization techniques for nanomaterials. In: Nanomaterials for Solar Cell Applications, 1st ed. Elsevier Inc., pp 97–124

104. Bohren CF (1983) Absorption and scattering of light by small particles. Absorpt Scatt Light by small Part. https://doi.org/10.1088/0031-9112/35/3/025

105. Huang X, El-Sayed MA (2010) Gold nanoparticles: Optical properties and implementations in cancer diagnosis and photothermal therapy. J Adv Res 1:13–28. https://doi.org/10.1016/j.jare.2010.02.002

106. Nielsen SS (1998) Ultraviolet, Visible, and Fluorescence Spectroscopy. Instr Man Food Anal Second Ed 91–94. https://doi.org/10.1007/978-1-4615-5439-4_26

107. Inkson BJ (2016) Scanning Electron Microscopy (SEM) and Transmission Electron Microscopy (TEM) for Materials Characterization. Elsevier Ltd

108. Reimer L (1989) Introduction: Transmision Electron Microscopy. In: Transmision Electron Microscopy: Physics of Image Formation and Microanalysis, Fourth edi. Springer, pp 1–15

109. Stetefeld J, McKenna SA, Patel TR (2016) Dynamic light scattering: a practical guide and applications in biomedical sciences. Biophys Rev 8:409–427. https://doi.org/10.1007/s12551-016-0218-6

110. Bhattacharjee S (2016) DLS and zeta potential - What they are and what they are not? J Control Release 235:337–351. https://doi.org/10.1016/j.jconrel.2016.06.017

111. Gan SD, Patel KR (2013) Enzyme immunoassay and enzyme-linked immunosorbent assay. J Invest Dermatol 133:1–3. https://doi.org/10.1038/jid.2013.287

112. Butler JE (2000) Enzyme-linked immunosorbent assay. J Immunoassay 21:165–209. https://doi.org/10.1080/01971520009349533

113. Paulie S, Perlmann P, Perlmann H (2006) Enzyme- Linked I mmunosorbent Assay. In: Cell Biology, 3rd ed. Elsevier, p 2328

114. Hnasko R (2015) ELISA: Methods and Protocols. ELISA Methods Protoc 1–216. https://doi.org/10.1007/978-1-4939-2742-5

115. Crowther JR (1995) ELISA: Theory and Practice, 1st ed. Humana Press, New Jersey

116. Galbraith DW, Bohnert HJ, Bourque DP, Biology AS for C (1995) Methods in Plant

Cell Biology. Academic Press

117. Immunosensors P, Reader O, Russell SM, et al (2022) Improving the Quantification of Colorimetric Signals in. 1–9

118. Monroy IL (2013) Using the contrast ratio method and achromatic transmission densitometry as a substitute for Status A transmission densitometry with the Photographic Activity Test For Enclosure Materials

119. Johnson J, Harris T (2010) Full-field optical thickness profilometry of semitransparent thin films with transmission densitometry. Appl Opt 49:2920–2928. https://doi.org/10.1364/AO.49.002920

120. Park J (2018) An Optimized Colorimetric Readout Method for Lateral Flow Immunoassays. Sensors (Basel) 18:. https://doi.org/10.3390/s18124084

121. Coleman B, Coarsey C, Asghar W, et al (2020) HHS Public Access. 225–231. https://doi.org/10.1016/j.snb.2018.11.036.Point-of-care

122. Wang J, Wu H, Yang Y, et al (2018) Bacterial species-identifiable magnetic nanosystems for early sepsis diagnosis and extracorporeal photodynamic blood disinfection. Nanoscale 10:132–141. https://doi.org/10.1039/C7NR06373C

123. Paoli CJ, Reynolds MA, Sinha M, et al (2018) Epidemiology and Costs of Sepsis in the United States—An Analysis Based on Timing of Diagnosis and Severity Level*. Crit Care Med 46:

124. Henriquez-Camacho C, Losa J (2014) Biomarkers for sepsis. Biomed Res Int 2014:547818. https://doi.org/10.1155/2014/547818

125. Meisner M (2002) Pathobiochemistry and clinical use of procalcitonin. Clin Chim Acta 323:17–29. https://doi.org/https://doi.org/10.1016/S0009-8981(02)00101-8

126. Meynaar IA, Droog W, Batstra M, et al (2011) In Critically Ill Patients, Serum Procalcitonin Is More Useful in Differentiating between Sepsis and SIRS than CRP, Il-6, or LBP. Crit Care Res Pract 2011:594645. https://doi.org/10.1155/2011/594645

127. Toma M, Tawa K (2016) Polydopamine Thin Films as Protein Linker Layer for Sensitive Detection of Interleukin-6 by Surface Plasmon Enhanced Fluorescence Spectroscopy. ACS Appl Mater Interfaces 8:22032–22038. https://doi.org/10.1021/acsami.6b06917

128. Gong L, Dai H, Zhang S, Lin Y (2016) Silver Iodide-Chitosan Nanotag Induced Biocatalytic Precipitation for Self-Enhanced Ultrasensitive Photocathodic Immunosensor. Anal Chem 88:5775–5782. https://doi.org/10.1021/acs.analchem.6b00297

129. Lau UY, Saxer SS, Lee J, et al (2016) Direct Write Protein Patterns for Multiplexed Cytokine Detection from Live Cells Using Electron Beam Lithography. ACS Nano 10:723–729. https://doi.org/10.1021/acsnano.5b05781

130. Hao Z, Pan Y, Shao W, et al (2019) Graphene-based fully integrated portable nanosensing system for on-line detection of cytokine biomarkers in saliva. Biosens Bioelectron 134:16–23. https://doi.org/10.1016/j.bios.2019.03.053

131. Russell C, Ward AC, Vezza V, et al (2019) Development of a needle shaped

microelectrode for electrochemical detection of the sepsis biomarker interleukin-6 (IL-6) in real time. Biosens Bioelectron 126:806–814. https://doi.org/10.1016/j.bios.2018.11.053

132. Peng J, Guan J, Yao H, Jin X (2016) Magnetic colorimetric immunoassay for human interleukin-6 based on the oxidase activity of ceria spheres. Anal Biochem 492:63–68. https://doi.org/10.1016/j.ab.2015.09.018

133. Tang CK, Vaze A, Shen M, Rusling JF (2016) High-Throughput Electrochemical Microfluidic Immunoarray for Multiplexed Detection of Cancer Biomarker Proteins. ACS sensors 1:1036–1043. https://doi.org/10.1021/acssensors.6b00256

134. Wu D, Rios-Aguirre D, Chounlakone M, et al (2018) Sequentially multiplexed amperometry for electrochemical biosensors. Biosens Bioelectron 117:522–529. https://doi.org/https://doi.org/10.1016/j.bios.2018.06.049

135. Wei H, Ni S, Cao C, et al (2018) Graphene Oxide Signal Reporter Based Multifunctional Immunosensing Platform for Amperometric Profiling of Multiple Cytokines in Serum. ACS sensors 3:1553–1561. https://doi.org/10.1021/acssensors.8b00365

136. Borse V, Srivastava R (2019) Fluorescence lateral flow immunoassay based point-of-care nanodiagnostics for orthopedic implant-associated infection. Sensors Actuators B Chem 280:24–33. https://doi.org/https://doi.org/10.1016/j.snb.2018.10.034

137. Wang Y, Sun J, Hou Y, et al (2019) RETRACTED: A SERS-based lateral flow assay biosensor for quantitative and ultrasensitive detection of interleukin-6 in unprocessed whole blood. Biosens Bioelectron 141:111432. https://doi.org/10.1016/j.bios.2019.111432

138. Reddy BJ, Hassan U, Seymour C, et al (2018) Point-of-care sensors for the management of sepsis. Nat Biomed Eng 2:640–648. https://doi.org/10.1038/s41551-018-0288-9

139. Hou T, Huang D, Zeng R, et al (2015) Accuracy of serum interleukin (IL)-6 in sepsis diagnosis: a systematic review and meta-analysis. Int J Clin Exp Med 8:15238–15245

140. Vashist SK, van Oordt T, Schneider EM, et al (2015) A smartphone-based colorimetric reader for bioanalytical applications using the screen-based bottom illumination provided by gadgets. Biosens Bioelectron 67:248–255. https://doi.org/10.1016/j.bios.2014.08.027

141. Wang L-J, Chang Y-C, Sun R, Li L (2017) A multichannel smartphone optical biosensor for high-throughput point-of-care diagnostics. Biosens Bioelectron 87:686–692. https://doi.org/10.1016/j.bios.2016.09.021

142. Russell SM, Alba-Patiño A, Borges M, de la Rica R (2019) Multifunctional motion-to-color janus transducers for the rapid detection of sepsis biomarkers in whole blood. Biosens Bioelectron 140:111346. https://doi.org/10.1016/j.bios.2019.111346

143. Tsai D-H, Shelton MP, DelRio FW, et al (2012) Quantifying dithiothreitol displacement of functional ligands from gold nanoparticles. Anal Bioanal Chem 404:3015–3023. https://doi.org/10.1007/s00216-012-6418-4

144. Rodríguez-Lorenzo L, de la Rica R, Álvarez-Puebla RA, et al (2012) Plasmonic

nanosensors with inverse sensitivity by means of enzyme-guided crystal growth. Nat Mater 11:604–607. https://doi.org/10.1038/nmat3337

145. Kong T, You JB, Zhang B, et al (2019) Accessory-free quantitative smartphone imaging of colorimetric paper-based assays. Lab Chip 19:1991–1999. https://doi.org/10.1039/C9LC00165D

146. Stalenhoef JE, van Nieuwkoop C, Wilson DC, et al (2018) Biomarker guided triage can reduce hospitalization rate in community acquired febrile urinary tract infection. J Infect 77:18–24. https://doi.org/10.1016/j.jinf.2018.05.007

147. Russell SM, Doménech-Sánchez A, de la Rica R (2017) Augmented Reality for Real-Time Detection and Interpretation of Colorimetric Signals Generated by Paper-Based Biosensors. ACS sensors 2:848–853. https://doi.org/10.1021/acssensors.7b00259

148. Reboud J, Xu G, Garrett A, et al (2019) Paper-based microfluidics for DNA diagnostics of malaria in low resource underserved rural communities. Proc Natl Acad Sci U S A 116:4834–4842. https://doi.org/10.1073/pnas.1812296116

149. Roig-Sanchez S, Jungstedt E, Anton-Sales I, et al (2019) Nanocellulose films with multiple functional nanoparticles in confined spatial distribution. Nanoscale Horizons 4:634–641. https://doi.org/10.1039/C8NH00310F

150. Tenda K, van Gerven B, Arts R, et al (2018) Paper-Based Antibody Detection Devices Using Bioluminescent BRET-Switching Sensor Proteins. Angew Chemie Int Ed 57:15369–15373. https://doi.org/https://doi.org/10.1002/anie.201808070

151. Chu W, Chen Y, Liu W, et al (2017) Paper-based chemiluminescence immunodevice with temporal controls of reagent transport technique. Sensors Actuators B Chem 250:324–332. https://doi.org/https://doi.org/10.1016/j.snb.2017.04.126

152. Wang S, Ge L, Song X, et al (2012) Simple and covalent fabrication of a paper device and its application in sensitive chemiluminescence immunoassay. Analyst 137:3821–3827. https://doi.org/10.1039/c2an35266d

153. Calabria D, Caliceti C, Zangheri M, et al (2017) Smartphone-based enzymatic biosensor for oral fluid L-lactate detection in one minute using confined multilayer paper reflectometry. Biosens Bioelectron 94:124–130. https://doi.org/10.1016/j.bios.2017.02.053

154. Russell SM, de la Rica R (2018) Paper transducers to detect plasmon variations in colorimetric nanoparticle biosensors. Sensors Actuators B Chem 270:327–332. https://doi.org/https://doi.org/10.1016/j.snb.2018.05.052

155. Catala C, Mir-Simon B, Feng X, et al (2016) Online SERS Quantification of Staphylococcus aureus and the Application to Diagnostics in Human Fluids. Adv Mater Technol 1:1600163. https://doi.org/https://doi.org/10.1002/admt.201600163

156. Ellairaja S, Krithiga N, Ponmariappan S, Vasantha VS (2017) Novel Pyrimidine Tagged Silver Nanoparticle Based Fluorescent Immunoassay for the Detection of Pseudomonas aeruginosa. J Agric Food Chem 65:1802–1812. https://doi.org/10.1021/acs.jafc.6b04790

157. Liang B, Zhu Q, Fang L, et al (2017) An origami paper device for complete elimination of interferents in enzymatic electrochemical biosensors. Electrochem commun 82:43–46. https://doi.org/https://doi.org/10.1016/j.elecom.2017.07.001

158. Ruivo S, Azevedo AM, Prazeres DMF (2017) Colorimetric detection of D-dimer in a paper-based immunodetection device. Anal Biochem 538:5–12. https://doi.org/10.1016/j.ab.2017.09.009

159. Deraney RN, Mace CR, Rolland JP, Schonhorn JE (2016) Multiplexed, Patterned-Paper Immunoassay for Detection of Malaria and Dengue Fever. Anal Chem 88:6161–6165. https://doi.org/10.1021/acs.analchem.6b00854

160. Kim HJ, Kwon C, Noh H (2019) Paper-Based Diagnostic System Facilitating Escherichia coli Assessments by Duplex Coloration. ACS sensors 4:2435–2441. https://doi.org/10.1021/acssensors.9b01034

161. Liu H, Xiang Y, Lu Y, Crooks RM (2012) Aptamer-Based Origami Paper Analytical Device for Electrochemical Detection of Adenosine. Angew Chemie Int Ed 51:6925–6928. https://doi.org/https://doi.org/10.1002/anie.201202929

162. McLintock A, Cunha-Matos CA, Zagnoni M, et al (2014) Universal Surface-Enhanced Raman Tags: Individual Nanorods for Measurements from the Visible to the Infrared (514–1064 nm). ACS Nano 8:8600–8609. https://doi.org/10.1021/nn503311d

163. Cai W, Wang W, Lu L, Chen T (2013) Coating sulfonated polystyrene microspheres with highly dense gold nanoparticle shell for SERS application. Colloid Polym Sci 291:2023–2029. https://doi.org/10.1007/s00396-013-2928-7

164. Basarir F (2012) Fabrication of Gold Patterns via Multilayer Transfer Printing and Electroless Plating. ACS Appl Mater Interfaces 4:1324–1329. https://doi.org/10.1021/am201605q

165. Khan S, Ul-Islam M, Ullah MW, et al (2018) Nano-gold assisted highly conducting and biocompatible bacterial cellulose-PEDOT:PSS films for biology-device interface applications. Int J Biol Macromol 107:865–873. https://doi.org/10.1016/j.ijbiomac.2017.09.064

166. Choi S, Kim S-K, Lee G-J, Park H-K (2015) Paper-based 3D microfluidic device for multiple bioassays. Sensors Actuators B Chem 219:245–250. https://doi.org/https://doi.org/10.1016/j.snb.2015.05.035

167. Chen C-A, Yeh W-S, Tsai T-T, et al (2019) Three-dimensional origami paper-based device for portable immunoassay applications. Lab Chip 19:598–607. https://doi.org/10.1039/c8lc01255e

168. Susmel S, O'Sullivan CK, Guilbault GG (2000) Human cytomegalovirus detection by a quartz crystal microbalance immunosensor. Enzyme Microb Technol 27:639–645. https://doi.org/10.1016/s0141-0229(00)00196-4

169. Pires F, Arcos-Martinez MJ, Dias-Cabral AC, et al (2018) A rapid magnetic particle-based enzyme immunoassay for human cytomegalovirus glycoprotein B quantification. J Pharm Biomed Anal 156:372–378. https://doi.org/10.1016/j.jpba.2018.04.019

170. Pires F, Silva H, Domínguez-Renedo O, et al (2015) Disposable immunosensor for human cytomegalovirus glycoprotein B detection. Talanta 136:42–46. https://doi.org/10.1016/j.talanta.2014.12.016

171. de la Rica R, Aili D, Stevens MM (2012) Enzyme-responsive nanoparticles for drug release and diagnostics. Adv Drug Deliv Rev 64:967–978.

https://doi.org/10.1016/j.addr.2012.01.002

172. Boris DC, Colby RH (1998) Rheology of Sulfonated Polystyrene Solutions. Macromolecules 31:5746–5755. https://doi.org/10.1021/ma971884i

173. Zhang D, Gao B, Chen Y, Liu H (2018) Converting colour to length based on the coffee-ring effect for quantitative immunoassays using a ruler as readout. Lab Chip 18:271–275. https://doi.org/10.1039/c7lc01127j

174. Cui L, Zhang J, Zhang X, et al (2012) Suppression of the Coffee Ring Effect by Hydrosoluble Polymer Additives. ACS Appl Mater Interfaces 4:2775–2780. https://doi.org/10.1021/am300423p

175. Karami A, Hasani M, Azizi Jalilian F, Ezati R (2021) Conventional PCR assisted single-component assembly of spherical nucleic acids for simple colorimetric detection of SARS-CoV-2. Sensors Actuators B Chem 328:128971. https://doi.org/https://doi.org/10.1016/j.snb.2020.128971

176. Huang C, Wang Y, Li X, et al (2020) Clinical features of patients infected with 2019 novel coronavirus in Wuhan, China. Lancet 395:497–506. https://doi.org/https://doi.org/10.1016/S0140-6736(20)30183-5

177. Channappanavar R, Perlman S (2017) Pathogenic human coronavirus infections: causes and consequences of cytokine storm and immunopathology. Semin Immunopathol 39:529–539. https://doi.org/10.1007/s00281-017-0629-x

178. Polidoro RB, Hagan RS, de Santis Santiago R, Schmidt NW (2020) Overview: Systemic Inflammatory Response Derived From Lung Injury Caused by SARS-CoV-2 Infection Explains Severe Outcomes in COVID-19 . Front. Immunol. 11:1626

179. Wang H, Luo S, Shen Y, et al (2020) Multiple Enzyme Release, Inflammation Storm and Hypercoagulability Are Prominent Indicators For Disease Progression In COVID-19: A Multi-Centered, Correlation Study with CT Imaging Score. SSRN Electron J. https://doi.org/10.2139/SSRN.3544837

180. Christopher M, Iva F, Andrea P, et al (2020) Natural killer cell immunotypes related to COVID-19 disease severity. Sci Immunol 5:eabd6832. https://doi.org/10.1126/sciimmunol.abd6832

181. Kwon J-S, Kim JY, Kim M-C, et al (2020) Factors of Severity in Patients with COVID-19: Cytokine/Chemokine Concentrations, Viral Load, and Antibody Responses. Am J Trop Med Hyg 103:2412–2418. https://doi.org/10.4269/ajtmh.20-1110

182. Han H, Ma Q, Li C, et al (2020) Profiling serum cytokines in COVID-19 patients reveals IL-6 and IL-10 are disease severity predictors. Emerg Microbes Infect 9:1123–1130. https://doi.org/10.1080/22221751.2020.1770129

183. Chen G, Wu D, Guo W, et al (2020) Clinical and immunological features of severe and moderate coronavirus disease 2019. J Clin Invest 130:2620–2629. https://doi.org/10.1172/JCI137244

184. Cai Q, Huang D, Ou P, et al (2020) COVID-19 in a designated infectious diseases hospital outside Hubei Province, China. Allergy 75:1742–1752. https://doi.org/https://doi.org/10.1111/all.14309

185. Hollander JE, Carr BG (2020) Virtually Perfect? Telemedicine for Covid-19. N Engl J

Med 382:1679–1681. https://doi.org/10.1056/NEJMp2003539

186. Russell SM, Alba-Patiño A, Barón E, et al (2020) Biosensors for Managing the COVID-19 Cytokine Storm: Challenges Ahead. ACS sensors 5:1506–1513. https://doi.org/10.1021/acssensors.0c00979

187. Zhao H, Liu F, Xie W, et al (2021) Ultrasensitive supersandwich-type electrochemical sensor for SARS-CoV-2 from the infected COVID-19 patients using a smartphone. Sensors Actuators B Chem 327:128899. https://doi.org/https://doi.org/10.1016/j.snb.2020.128899

188. Alba-Patiño A, Adrover-Jaume C, de la Rica R (2020) Nanoparticle Reservoirs for Paper-Only Immunosensors. ACS sensors 5:147–153. https://doi.org/10.1021/acssensors.9b01937

189. Alba-Patiño A, Russell SM, Borges M, et al (2020) Nanoparticle-based mobile biosensors for the rapid detection of sepsis biomarkers in whole blood. Nanoscale Adv 2:1253–1260. https://doi.org/10.1039/D0NA00026D

190. Tertis M, Leva PI, Bogdan D, et al (2019) Impedimetric aptasensor for the label-free and selective detection of Interleukin-6 for colorectal cancer screening. Biosens Bioelectron 137:123–132. https://doi.org/https://doi.org/10.1016/j.bios.2019.05.012

191. Sabaté del Río J, Henry OYF, Jolly P, Ingber DE (2019) An antifouling coating that enables affinity-based electrochemical biosensing in complex biological fluids. Nat Nanotechnol 14:1143–1149. https://doi.org/10.1038/s41565-019-0566-z

192. Militano F, Poerio T, Mazzei R, et al (2017) Development of biohybrid immuno-selective membranes for target antigen recognition. Biosens Bioelectron 92:54–60. https://doi.org/https://doi.org/10.1016/j.bios.2017.02.003

193. Khosravi F, Loeian SM, Panchapakesan B (2017) Ultrasensitive Label-Free Sensing of IL-6 Based on PASE Functionalized Carbon Nanotube Micro-Arrays with RNA-Aptamers as Molecular Recognition Elements. Biosens. 7

194. Gentili D, D'Angelo P, Militano F, et al (2018) Integration of organic electrochemical transistors and immuno-affinity membranes for label-free detection of interleukin-6 in the physiological concentration range through antibody–antigen recognition. J Mater Chem B 6:5400–5406. https://doi.org/10.1039/C8TB01697F

195. Fabri-Faja N, Calvo-Lozano O, Dey P, et al (2019) Early sepsis diagnosis via protein and miRNA biomarkers using a novel point-of-care photonic biosensor. Anal Chim Acta 1077:232–242. https://doi.org/https://doi.org/10.1016/j.aca.2019.05.038

196. Diacci C, Berto M, Di Lauro M, et al (2017) Label-free detection of interleukin-6 using electrolyte gated organic field effect transistors. Biointerphases 12:05F401. https://doi.org/10.1116/1.4997760

197. Chen P, Chung MT, McHugh W, et al (2015) Multiplex Serum Cytokine Immunoassay Using Nanoplasmonic Biosensor Microarrays. ACS Nano 9:4173–4181. https://doi.org/10.1021/acsnano.5b00396

198. Chen H, Li J, Zhang X, et al (2018) Automated in Vivo Nanosensing of Breath-Borne Protein Biomarkers. Nano Lett 18:4716–4726. https://doi.org/10.1021/acs.nanolett.8b01070

199. Aydın EB, Aydın M, Sezgintürk MK (2020) The development of an ultra-sensitive electrochemical immunosensor using a PPyr-NHS functionalized disposable ITO sheet for the detection of interleukin 6 in real human serums. New J Chem 44:14228–14238. https://doi.org/10.1039/D0NJ03183F

200. Aydın EB (2020) Highly sensitive impedimetric immunosensor for determination of interleukin 6 as a cancer biomarker by using conjugated polymer containing epoxy side groups modified disposable ITO electrode. Talanta 215:120909. https://doi.org/https://doi.org/10.1016/j.talanta.2020.120909

201. Zhu J, He J, Verano M, et al (2018) An integrated adipose-tissue-on-chip nanoplasmonic biosensing platform for investigating obesity-associated inflammation. Lab Chip 18:3550–3560. https://doi.org/10.1039/C8LC00605A

202. Zhang K, Liu G, Goldys EM (2018) Robust immunosensing system based on biotin-streptavidin coupling for spatially localized femtogram mL−1 level detection of interleukin-6. Biosens Bioelectron 102:80–86. https://doi.org/https://doi.org/10.1016/j.bios.2017.11.023

203. Rutkowski P, Kaminska J, Kowalska M, et al (2002) Cytokine serum levels in soft tissue sarcoma patients: Correlations with clinico-pathological features and prognosis. Int J Cancer 100:463–471. https://doi.org/https://doi.org/10.1002/ijc.10496

204. Del Valle DM, Kim-Schulze S, Huang H-H, et al (2020) An inflammatory cytokine signature predicts COVID-19 severity and survival. Nat Med 26:1636–1643. https://doi.org/10.1038/s41591-020-1051-9

205. Huang BX, Kim H-Y, Dass C (2004) Probing three-dimensional structure of bovine serum albumin by chemical cross-linking and mass spectrometry. J Am Soc Mass Spectrom 15:1237–1247. https://doi.org/10.1016/j.jasms.2004.05.004

206. Luo P, Liu Y, Qiu L, et al (2020) Tocilizumab treatment in COVID-19: A single center experience. J Med Virol 92:814–818. https://doi.org/https://doi.org/10.1002/jmv.25801

207. Fu B, Xu X, Wei H (2020) Why tocilizumab could be an effective treatment for severe COVID-19? J Transl Med 18:164. https://doi.org/10.1186/s12967-020-02339-3

208. Seymour CW, Gesten F, Prescott HC, et al (2017) Time to Treatment and Mortality during Mandated Emergency Care for Sepsis. N Engl J Med 376:2235–2244. https://doi.org/10.1056/NEJMoa1703058

209. Rhodes A, Evans LE, Alhazzani W, et al (2017) Surviving Sepsis Campaign: International Guidelines for Management of Sepsis and Septic Shock: 2016. Intensive Care Med 43:304–377. https://doi.org/10.1007/s00134-017-4683-6

210. Hirsch EB, Tam VH (2010) Impact of multidrug-resistant Pseudomonas aeruginosa infection on patient outcomes. Expert Rev Pharmacoecon Outcomes Res 10:441–451. https://doi.org/10.1586/erp.10.49

211. Jochumsen N, Marvig RL, Damkiær S, et al (2016) The evolution of antimicrobial peptide resistance in Pseudomonas aeruginosa is shaped by strong epistatic interactions. Nat Commun 7:13002. https://doi.org/10.1038/ncomms13002

212. Jones RN (2010) Microbial Etiologies of Hospital-Acquired Bacterial Pneumonia and Ventilator-Associated Bacterial Pneumonia. Clin Infect Dis 51:S81–S87.

https://doi.org/10.1086/653053

213. Pazos-Perez N, Pazos E, Catala C, et al (2016) Ultrasensitive multiplex optical quantification of bacteria in large samples of biofluids. Sci Rep 6:29014. https://doi.org/10.1038/srep29014

214. Papadakis G, Pantazis AK, Ntogka M, et al (2019) 3D-printed Point-of-Care Platform for Genetic Testing of Infectious Diseases Directly in Human Samples Using Acoustic Sensors and a Smartphone. ACS sensors 4:1329–1336. https://doi.org/10.1021/acssensors.9b00264

215. Zheng L, Cai G, Qi W, et al (2020) Optical Biosensor for Rapid Detection of Salmonella typhimurium Based on Porous Gold@Platinum Nanocatalysts and a 3D Fluidic Chip. ACS sensors 5:65–72. https://doi.org/10.1021/acssensors.9b01472

216. Amiri M, Bezaatpour A, Jafari H, et al (2018) Electrochemical Methodologies for the Detection of Pathogens. ACS sensors 3:1069–1086. https://doi.org/10.1021/acssensors.8b00239

217. Zhou S, Lu C, Li Y, et al (2020) Gold Nanobones Enhanced Ultrasensitive Surface-Enhanced Raman Scattering Aptasensor for Detecting Escherichia coli O157:H7. ACS sensors 5:588–596. https://doi.org/10.1021/acssensors.9b02600

218. Song J, Li Y, Yin F, et al (2020) Enhanced Electrochemical Impedance Spectroscopy Analysis of Microbial Biofilms on an Electrochemically In Situ Generated Graphene Interface. ACS sensors 5:1795–1803. https://doi.org/10.1021/acssensors.0c00570

219. Dong T, Santos S, Yang Z, et al (2020) Sputum and salivary protein biomarkers and point-of-care biosensors for the management of COPD. Analyst 145:1583–1604. https://doi.org/10.1039/C9AN01704F

220. Passos da Silva D, Matwichuk ML, Townsend DO, et al (2019) The Pseudomonas aeruginosa lectin LecB binds to the exopolysaccharide Psl and stabilizes the biofilm matrix. Nat Commun 10:2183. https://doi.org/10.1038/s41467-019-10201-4

221. Li X, Kong H, Mout R, et al (2014) Rapid Identification of Bacterial Biofilms and Biofilm Wound Models Using a Multichannel Nanosensor. ACS Nano 8:12014–12019. https://doi.org/10.1021/nn505753s

222. Pastells C, Pascual N, Sanchez-Baeza F, Marco M-P (2016) Immunochemical Determination of Pyocyanin and 1-Hydroxyphenazine as Potential Biomarkers of Pseudomonas aeruginosa Infections. Anal Chem 88:1631–1638. https://doi.org/10.1021/acs.analchem.5b03490

223. Hiraiwa M, Kim J-H, Lee H-B, et al (2015) Amperometric immunosensor for rapid detection of Mycobacterium tuberculosis. J Micromechanics Microengineering 25:55013. https://doi.org/10.1088/0960-1317/25/5/055013

224. Inoue S, Becker AL, Kim J-H, et al (2014) Semi-Automated, Occupationally Safe Immunofluorescence Microtip Sensor for Rapid Detection of Mycobacterium Cells in Sputum. PLoS One 9:e86018

225. Kim J-H, Yeo W-H, Shu Z, et al (2012) Immunosensor towards low-cost, rapid diagnosis of tuberculosis. Lab Chip 12:1437–1440. https://doi.org/10.1039/C2LC21131A

226. Massai F, Imperi F, Quattrucci S, et al (2011) A multitask biosensor for micro-volumetric detection of N-3-oxo-dodecanoyl-homoserine lactone quorum sensing signal. Biosens Bioelectron 26:3444–3449. https://doi.org/https://doi.org/10.1016/j.bios.2011.01.022

227. Kukhtin A V, Norville R, Bueno A, et al (2020) A Benchtop Automated Sputum-to-Genotype System Using a Lab-on-a-Film Assembly for Detection of Multidrug-Resistant Mycobacterium tuberculosis. Anal Chem 92:5311–5318. https://doi.org/10.1021/acs.analchem.9b05853

228. Zheng L, Cai G, Wang S, et al (2019) A microfluidic colorimetric biosensor for rapid detection of Escherichia coli O157:H7 using gold nanoparticle aggregation and smart phone imaging. Biosens Bioelectron 124–125:143–149. https://doi.org/10.1016/j.bios.2018.10.006

229. Huang X, Chen R, Xu H, et al (2016) Nanospherical Brush as Catalase Container for Enhancing the Detection Sensitivity of Competitive Plasmonic ELISA. Anal Chem 88:1951–1958. https://doi.org/10.1021/acs.analchem.5b04518

230. Jiang X, Jin H, Sun Y, et al (2020) Assembly of black phosphorus quantum dots-doped MOF and silver nanoclusters as a versatile enzyme-catalyzed biosensor for solution, flexible substrate and latent fingerprint visual detection of baicalin. Biosens Bioelectron 152:112012. https://doi.org/https://doi.org/10.1016/j.bios.2020.112012

231. Sun J, Mathesh M, Li W, Wilson DA (2019) Enzyme-Powered Nanomotors with Controlled Size for Biomedical Applications. ACS Nano 13:10191–10200. https://doi.org/10.1021/acsnano.9b03358

232. Xie Y, Fu S, Wu J, et al (2017) Motor-based microprobe powered by bio-assembled catalase for motion detection of DNA. Biosens Bioelectron 87:31–37. https://doi.org/10.1016/j.bios.2016.07.104

233. Lamberg P, Shleev S, Ludwig R, et al (2014) Performance of enzymatic fuel cell in cell culture. Biosens Bioelectron 55:168–173. https://doi.org/https://doi.org/10.1016/j.bios.2013.12.013

234. Song G, Chen Y, Liang C, et al (2016) Catalase-Loaded TaOx Nanoshells as Bio-Nanoreactors Combining High-Z Element and Enzyme Delivery for Enhancing Radiotherapy. Adv Mater 28:7143–7148. https://doi.org/https://doi.org/10.1002/adma.201602111

235. Jordana-Lluch E, Garcia V, Kingdon ADH, et al (2020) A Simple Polymicrobial Biofilm Keratinocyte Colonization Model for Exploring Interactions Between Commensals, Pathogens and Antimicrobials . Front. Microbiol. 11:291

236. Mangwani N, Shukla SK, Kumari S, et al (2016) Effect of biofilm parameters and extracellular polymeric substance composition on polycyclic aromatic hydrocarbon degradation. RSC Adv 6:57540–57551. https://doi.org/10.1039/C6RA12824F

237. Frederick JR, Elkins JG, Bollinger N, et al (2001) Factors Affecting Catalase Expression in Pseudomonas aeruginosa Biofilms and Planktonic Cells. Appl Environ Microbiol 67:1375–1379. https://doi.org/10.1128/AEM.67.3.1375-1379.2001/ASSET/97E20EB7-F6A8-42B6-8044-D9A65804728B/ASSETS/GRAPHIC/AM0311453004.JPEG

238. Sultana ST, Call DR, Beyenal H (2016) Eradication of Pseudomonas aeruginosa biofilms and persister cells using an electrochemical scaffold and enhanced antibiotic susceptibility. npj Biofilms Microbiomes 2:2. https://doi.org/10.1038/s41522-016-0003-0

239. Fernández M, Porcel M, de la Torre J, et al (2015) Analysis of the pathogenic potential of nosocomial Pseudomonas putida strains . Front. Microbiol. 6:871

240. de la Rica R, Baldi A, Fernández-Sánchez C, Matsui H (2009) Single-cell pathogen detection with a reverse-phase immunoassay on impedimetric transducers. Anal Chem 81:7732–7736. https://doi.org/10.1021/ac901210f

241. Clemente A, Alba-Patiño A, Santopolo G, et al (2021) Optimized detection of lung IL-6: Via enzymatic liquefaction of low respiratory tract samples: Application for managing ventilated patients. Analyst 146:6537–6546. https://doi.org/10.1039/d1an00763g

242. González del Campo M del M, Alba-Patiño A, Palomino C, et al (2022) Boosting the sensitivity of paper-based biosensors with polymeric water-soluble reservoirs. Sensors Actuators B Chem 354:. https://doi.org/10.1016/j.snb.2021.131214

243. Zhang K, Liu G, Goldys EM (2018) Robust immunosensing system based on biotin-streptavidin coupling for spatially localized femtogram mL−1 level detection of interleukin-6. Biosens Bioelectron 102:80–86. https://doi.org/10.1016/j.bios.2017.11.023

244. Wang Y, Sun J, Hou Y, et al (2019) A SERS-based lateral flow assay biosensor for quantitative and ultrasensitive detection of interleukin-6 in unprocessed whole blood. Biosens Bioelectron 141:111432. https://doi.org/10.1016/j.bios.2019.111432

245. Aydın EB, Aydın M, Sezgintürk MK (2020) The development of an ultra-sensitive electrochemical immunosensor using a PPyr-NHS functionalized disposable ITO sheet for the detection of interleukin 6 in real human serums. New J Chem. https://doi.org/10.1039/d0nj03183f

APPENDICES

9.1 Appendix 1. Supplementary materials and methods, and Figures for: NANOPARTICLE-BASED MOBILE BIOSENSORS FOR THE RAPID DETECTION OF SEPSIS BIOMARKERS IN WHOLE BLOOD

Synthesis of PVP-coated nanoparticles

Gold(III) chloride trihydrate (99.9 %, HAuCl4·3H2O), polyvynil pirrolidone (PVP, MW 25000), trisodium citrate dihydrated (99.9 %), ethanol (99.5%) and N,Ndimethylformamide (DMF, 99.9 %) were purchased from Sigma-Aldrich (Germany). All reactants were used without further purification. Milli-Q water (18 MΩ cm-1) was used in all aqueous solutions, and all the glassware was cleaned with aqua regia before the experiments.

Synthesis of gold seeds: spherical gold nanoparticles of approx. 15 nm diameter were produced by a modification of the well-known Turkevich method [1–3]. Briefly, 100 mL of water were heated to boil and an aqueous solution of sodium citrate (2.5 mL, 0.1 mM) was added. One minute after the addition, 198 µL of a 0.127 M $HAuCl_4$ were added into the boiling solution under vigorous stirring. A condenser was used to prevent the evaporation of the solvent and the mixture was allowed to react for 1 hour under continuous boiling and stirring. During this time, the color of the solution gradually changed from colorless to purple to finally become deep red.

Transfer and concentration of the gold seeds: The 15 nm Au particles were transferred into ethanol using PVP as a phase transfer through a modification of the Graff method, which renders them covered with PVP [4,5]. The as prepared gold nanoparticles (100 mL) were added drop-wise under vigorous stirring to an aqueous PVP solution (100 ml, 4 mM) and left under stirring at room temperature for 24 hours. Finally, the Au nanoparticles were centrifuged (twice at 10000rpm, 35 min), and the particles were redispersed in an ethanoic PVP solution (15 mL, 4 mM) to achieve a final Au^{o} concentration of 1 mM.

Spherical gold nanoparticles growth: Au NPs of approx. 45 nm were prepared using a seed mediated approach [5,6]. To this end, a growth solution containing PVP in EtOH (150 mL, 4 mM) was prepared. Next, 550 µL of HAuCl4 (0.127 M) aqueous solution were added, and immediately after to initiate the growth, 4 mL of the Au seeds in PVP/EtOH were injected under vigorous stirring. The solution was left undisturbed overnight to assure the completion of the overgrowth process. Finally, the particles were centrifuged 3 (twice at 7000rpm, 10 min) and redispersed in 190 mL DMF to achieve a final Au^{o} concentration of 3.75 x10-4 M.

Synthesis of PAH- and citrate-coated nanoparticles

Gold(III) chloride hydrate (99.995 %) and sodium citrate tribasic dihydrate (99%) were purchased from Sigma-Aldrich (Germany). Poly(allylamine hydrochloride) (PAH) was purchased from Alfa Aesar. All reactants were used without further purification. Milli-Q water(18 MΩ cm-1) was used in all aqueous solutions , and all the glassware was cleaned with aqua regia before the experiments. PAH-coated nanoparticles were prepared by bringing to a boil a solution containing 33 mg of gold chloride in 190 mL of Milli-Q water and adding 19 mg of PAH dissolved in 10 mL of water under agitation with a magnetic stirrer (Final volume 200 mL). The growth of gold nanoparticles was visually confirmed by the generation of red-burgundy color. After 10 minutes the solution was let to dry at room temperature. The resulting PAH-covered nanoparticles are unstable (the aggregate easily after centrifugation) and therefore PAH around the nanoparticles was substituted for SH-PEG-NH2 for the subsequent covalent attachment of proteins as indicated in the main manuscript. Citrate-capped nanoparticles were obtained by bringing to a boil a solution containing 0.5 mM gold chloride and adding sodium citrate to a final concentration of 0.75 mM under agitation with a magnetic stirrer (Final volume 250 mL). The solution was boiled for 10 min after the color appeared. The citrate around the nanoparticles was substituted for SH-PEG-COOH for the subsequent covalent attachment of proteins as indicated in the main manuscript.

Development of an app for real-time densitometry with an augmented reality guidance system

Table S1 appx 1. Algorithms from the OpenCV library (Java) used to automate image processing steps and a description of their function in the app. Full source code can be found at GitHub, and full documentation on the algorithms can be found at OpenCV.org.

General Pre-processing Steps	
cvtColor with COLOR_RGB2GRAY GaussianBlur	Changes color space from RBG to Gray Scale Applies a slight blur to the image to aid in edge detection
AR Guide Box Steps	
Imgproc.circle Imgproc.rectangle	A whited-out circle that acts as a max distance cap in the guide box Draws a fixed position guide box superimposed on the camera view
Biosensor Recognition Steps	
threshold with THRESH_OTSU Imgproc.Canny RETR_EXTERNAL and CHAIN_APPROX_SIMPLE arcLength and approxPolyDP	Making the image black and white to highlight edges of objects Applies Canny edge detection algorithm to segment edges of objects Finds outside edges of connected lines Checks for four-sided quadrilateral with 89-91 degree angles
Biosensor Image Remapping Steps	
getPerspectiveTransform warpPerspective amd INTER_LINEAR	Calculates perspective transform from four pairs of corresponding points Applies the perspective transformation with inter-linear interpolation
Colorimetric Signal Segmentation Steps	
GaussianBlur adaptiveThreshold with ADAPTVE_THRESH_GAUSSIAN_C THRESH_BINARY	Reduces noise for the adaptive threshold to work well Masks out the background substrate leaving only the signal pixels Prepares the mask to count total number of signal pixels
Pixel Measurement Steps	
getRectSubPix Imgproc.rectangle	Calculates the pixel intensities at the subpixel level for improved accuracy Draws AR boundaries around pixel measurement areas
AR Data Visualization Steps	
putText	real-time AR display of results for the background and the signal mean pixel densities.

Table S2 appx 1. Steps performed by the user for densitometric analysis with the scanner-based method versus the app-based method.

Steps for scanner-based densitometry	Steps for smartphone-based densitometry with our app
1. Place assay in scanner	1. Place assay on a neutral background
2. Choose color space and resolution	2. Align camera using AR guide box
3. Scan the image	3. Hover smartphone until progress bar is full
4. Upload image to ImageJ	
5. Invert colors	
6. Zoom in to locate signal	
7. Choose the region of interested (ROI) where the signal is located	
8. Use histogram function for pixel quantification in the ROI	
9. Choose the ROI where the background signal is located	
10. Use histogram function in background ROI	
11. Record the values for each ROI	
12. Subtract background from signal	
13. Record results	

The app subsitutes hardware to fix the angle and position of the phone with the AR guidance system shown in **Fig S1 appx 1**. With the AR guidance system, the user aligns the real-world view of the immunoassay within a square frame digitally superimposed on the smartphone screen (**Fig S1 appx 1**a-c). This guides the user to position the smartphone within the appropriate distance and angle range to ensure reproducible measurements. Variations in lighting conditions are compensated for by means of gray card calibration [7]. When these imaging parameters are within the correct range, the app automatically segments the paper substrate from the surrounding visual context, locates the colored spot generated by the immunoassay, and starts calculating the pixel intensity while at the same

time subtracting the background signal as calculated from four points around the region of interest (**Fig S1 appx 1**d). This can be followed in real time with a progress bar that advances as the measurements are taken (**Fig S1 appx 1**d(i) and Video S4.1). Any changes in imaging conditions that could result in inconsistent results trigger the app to stop taking measurements, therefore causing the progress bar to stop. This informs the user that the smartphone needs to be realigned with the AR guidance system to be within the accepted range of imaging conditions, at which point the measurements resume. When the app has acquired 50 valid measurements, the data set is evaluated to identify and remove outliers, and the average increase in pixel intensity with respect to the background signal is displayed. The whole process takes a few seconds (Video S4.1).

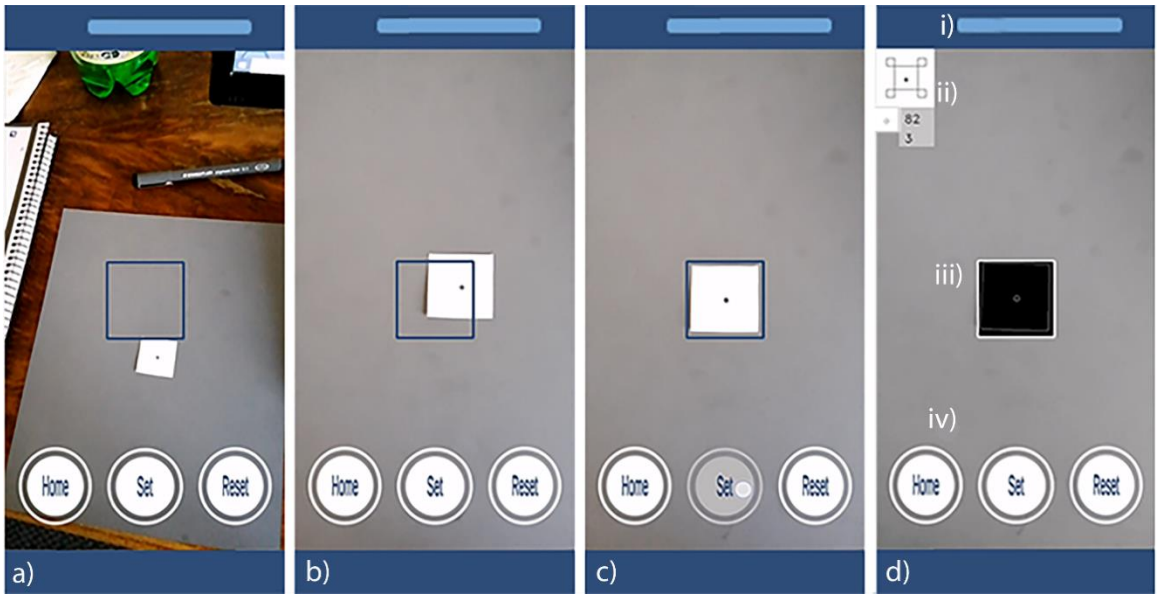

Fig S1 appx 1. Screenshots of the AR guidance system ((a) to (c)) and the measurement screen (d). The guide box is augmented in a fixed position on top of the real-world view as seen through the camera of a smartphone. The user moves the smartphone from a general view of their environment (a), towards the paper biosensor (b), until the biosensor fits inside the guide box as close to the inner edge as possible (c). After tapping the Set button, the Measurement screen (d) appears. In this screen, the progress bar (i) fills up as valid data points are collected. A complete data set contains 50 data points. The data points are measured in the Analysis Zone (ii) where the pixel intensities of the background and the signal are quantified. The paper biosensor is segmented from the real-world environment when it is found in the Detection Zone (iii) and remapped to the Analysis Zone. The user can switch between setting the Detection Zone and Resetting the Guide Box, as well as returning to the Home screen by tapping on the Navigation Buttons (iv).

Additional Figures

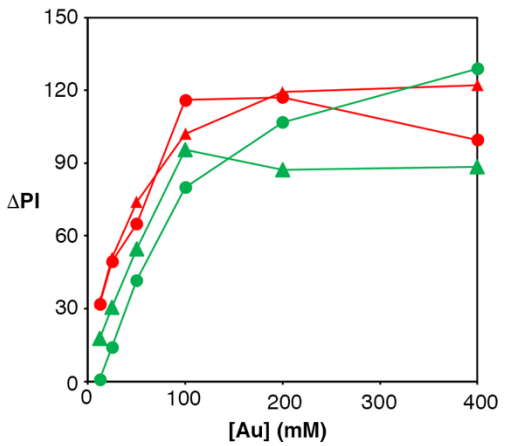

Fig S2 appx 1. Specific signal obtained by subtracting the pixel intensity generated by biosensors modified biotinylated BSA from biosensors modified with non-biotinylated BSA when using amine-coated nanoprobes and unmodified paper (red dots), aminecoated nanoparticles and PAH-modified paper (red triangles), carboxylate-modified nanoparticles and unmodified paper (green dots) and carboxylate-modified nanoparticles and paper modified with PAH and PSS (green triangles). The highest specific signals are obtained with a nanoparticle concentration of 400 mM ([Au]) and amine-coated nanoparticles combined with PAH-modified paper or carboxylate-modified nanoparticles combined with unmodified paper.

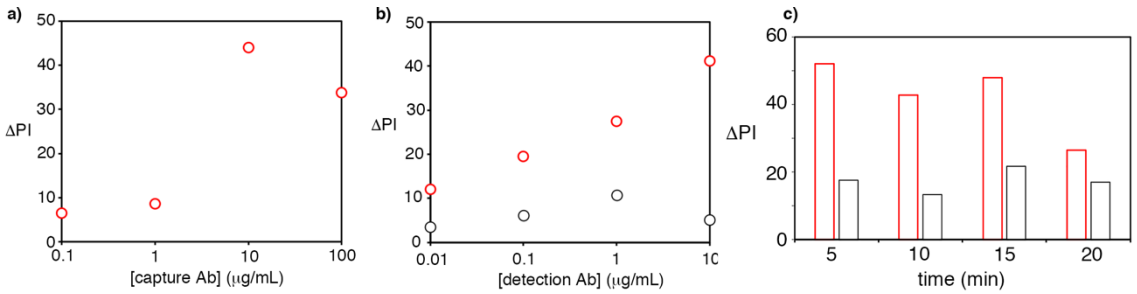

Fig S3 appx 1. Optimization of immunoassay parameters; a) Immunoassay performed with paper biosensors modified with different concentrations of capture antibody (best condition 10 μg·mL^{-1}); b) Immunoassays performed with different concentrations of detection antibody when the biosensors were modified with (red dots) or without (black dots) capture antibodies (best specific signal with 10 μg mL-1); c) Immunoassays performed with different incubation time with the detection antibody and biosensors modified with capture antibodies (red) or control biosensores without capture antibody (black); increasing the incubation times does not result in higher specific signals.

Fig S4 appx 1. Scanned images of wet paper biosensors after adding a drop of blood and performing the washing protocol described in Materials and Methods (4 times with 1mL of

PBST). The average pixel intensity in the region of interest is 4 ± 2, which is lower than the average signal of the blank in **Fig. 4.6**c (15 ± 4), therefore demonstrating that the color of the matrix is not a major source of interference with the proposed biosensors.

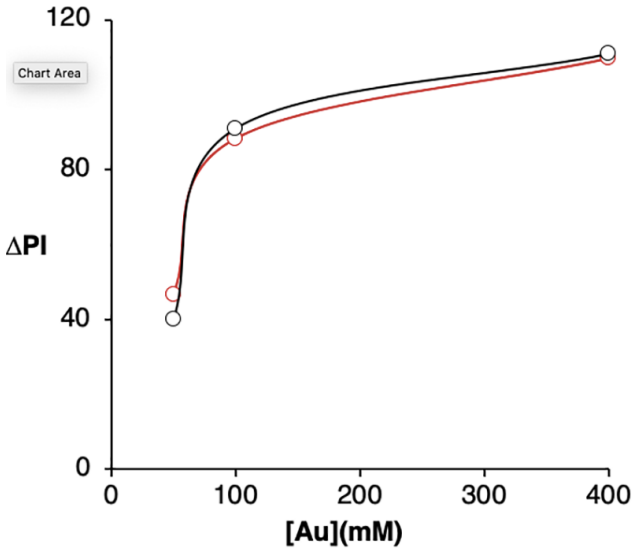

Fig S5 appx 1. Stability of avidin-modified nanoparticles over time. Recently made nanoparticles (black dots) were compared with nanoprobes that were two months old (red dots, kept at 4°C without any additional preservatives). The colorimetric signal DPI was obtained by subtracting the signal obtained with control biosensors modified with BSA from the signal obtained with biosensores modified with biotin-BSA. Both responses are very similar at the different nanoparticle concentrations assayed, which demonstrates that the avidin-modified nanoparticles are stable when kept for two months at 4°C.

Table S3 appx 1. Time required for each step of the assay.

Step	Time (seconds)
Incubation with sample (capture step)	300
Incubation with primary antibody	300
Incubation with nanoprobes	300
Wash steps	10(each)
Mobile detection	Under 5

References

[1] B. V. Enustun and J. Turkevich, *J. Am. Chem. Soc.*, 1963, **85**, 3317–3328.

[2] J. Turkevich, P. C. Stevenson and J. Hillier, *Discuss. Faraday Soc.*, 1951, **11**, 55–75.

[3] N. Pazos-Perez, J. M. Fitzgerald, V. Giannini, L. Guerrini and R. A. Alvarez- Puebla, *Nanoscale Adv.*, 2019, **1**, 122–131.

[4] C. Graf, D. L. J. Vossen, A. Imhof and A. Van Blaaderen, *Langmuir*, 2003, **19**, 6693–6700.

[5] N. Pazos-Perez, L. Guerrini and R. A. Alvarez-Puebla, *ACS Omega*, 2018, **3**, 17173–17179.

[6] M. Sivis, N. Pazos-Perez, R. Yu, R. Alvarez-Puebla, F. J. Garcia de Abajo and C. Ropers, *Commun. Phys.*, 2018, **1**, 3–8.

[7] T. Leeuw and E. Boss, *Sensors (Switzerland)*, 2018, **18**, s18010256.

9.2 Appendix 2. Supplementary Figures for: NANOPARTICLE RESERVOIRS FOR PAPER-ONLY IMMUNOSENSORS.

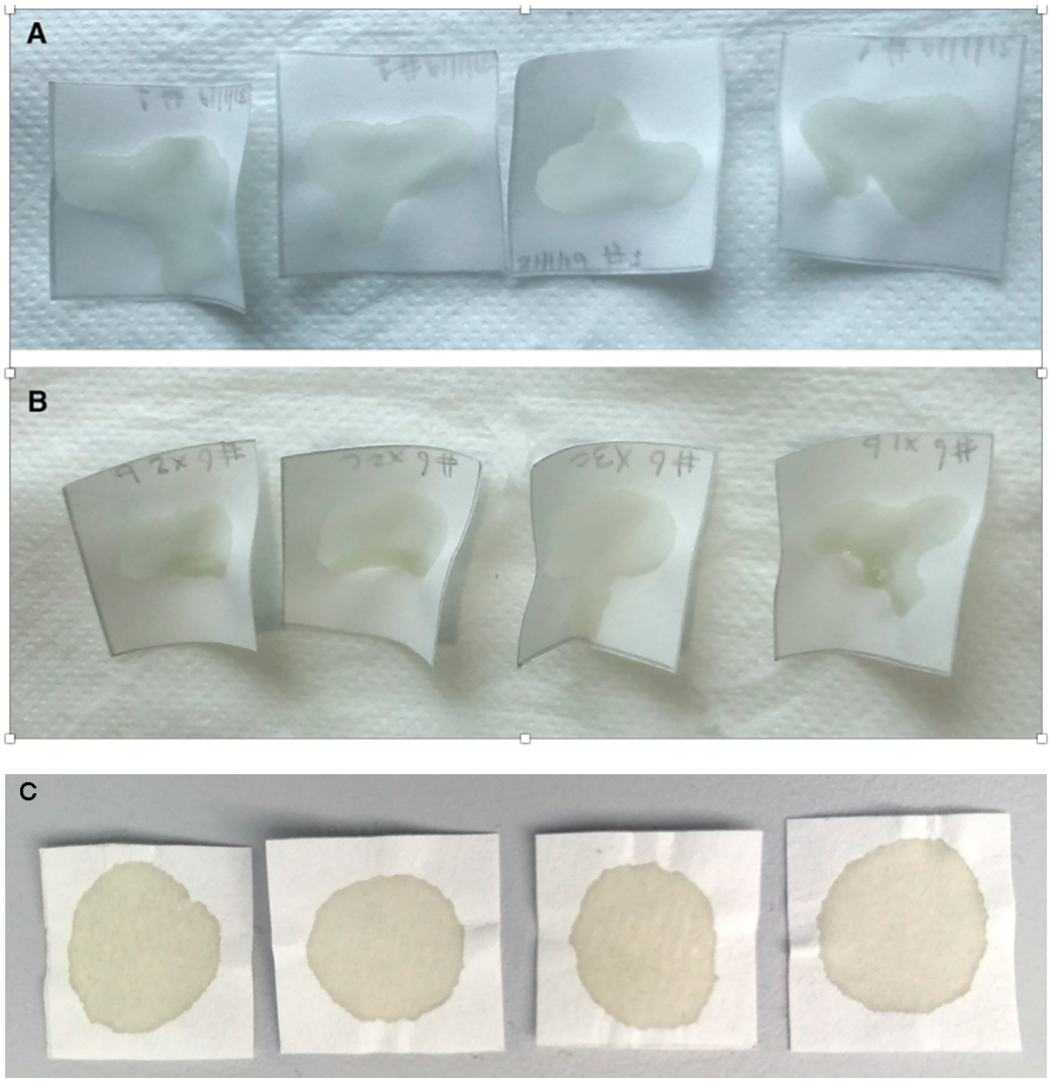

Fig S1 appx 2. Photographs of filter paper after addition of 30% PSS; (**A**) Whatman #1 (pore size 11 µm); (**B**) Whatman # 6 (pore size 3 µm); (**C**) Whatman # 41 (pore size 22 µm). It took a long time for the PSS solution to be adsorbed by the filter paper for paper types 1 and 6, and the substrates became heavily warped upon drying.

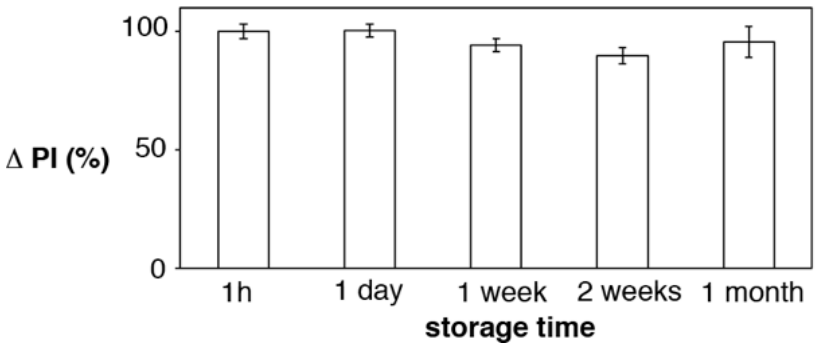

Fig S2 appx 2. Variation of the colorimetric signal (pixel intensity, PI) resulting from biospecific avidin-biotin interactions when the assay is performed using dry nanoparticle reservoirs stored for different times at room temperature. The percentage signal was calculated with respect to the reservoirs stored for 1 h. Error bars are the standard deviation (n = 3). Student´s t-test shows that mean values at different times are not statistically different from the mean value at t = 1 h ($p > 0.05$ in all cases).

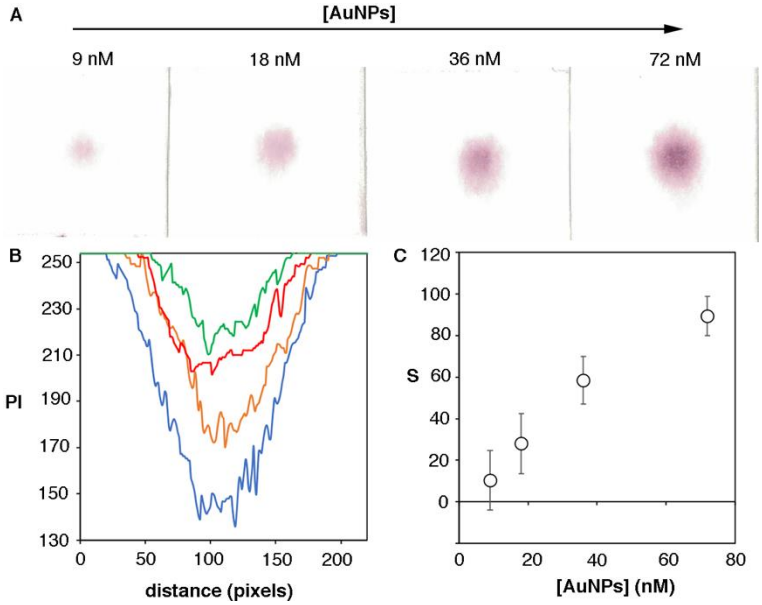

Fig S3 appx 2. Test for the formation of a “coffee ring” made of biotinylated BSA. To rule out that biotin-BSA generates a “coffee ring” upon drying, paper substrates containing dry biotinylated BSA were modified with a drop of avidin-decorated nanoparticles (2 μL) at different concentrations instead of transferring them from the nanoparticle reservoir. In **Fig S3 appx 2**A the colored spots obtained after washing the nanoparticles 3 times with PBST do not show a coffee a ring. Actually, the colored spots are more intense in the center, since the nanoparticles diffuse laterally to a larger extent in the absence of PSS. Profile analyses in **Fig S3 appx 2**B corroborate that no coffee rings are formed when the nanoparticles are dispensed as a drop rather than by transferring them from the reservoir. **Fig S3 appx 2**C shows the quantification of the colorimetric signal in 3 independent experiments (error bars are the standard deviation).

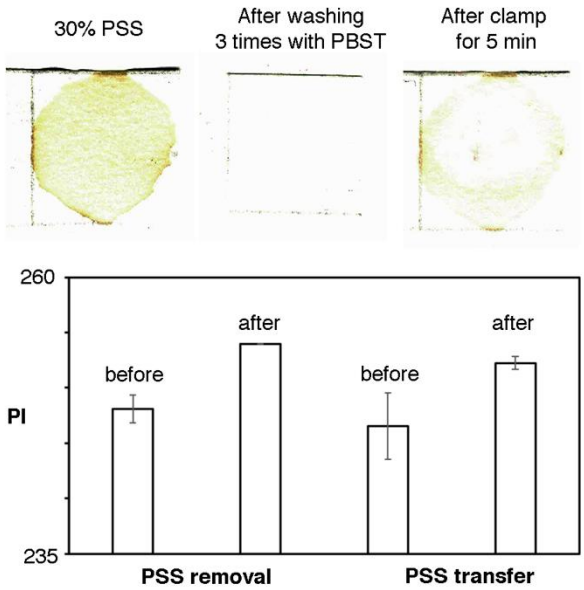

Fig S4 appx 2. The characteristic yellow color of PSS was used to follow its elimination after a washing procedure (3 times with 1 mL of PBST) or after 5 min in contact with a wet substrate (transfer). Error bars are the standard deviation (n = 3). As shown above, the washing procedure completely eliminated the yellow color from the paper, with the subsequent increase in pixel intensity. The transferring process also removed the color from the center of the paper, where the clamp pressed it against the receiving substrate. These experiments show that PSS is transferred along with the nanoparticles upon addition of liquids or after pressing it against a wet receiving substrate. Error bars are the standard deviation (n = 3).

Fig S5 appx 2. Pictures of the clamp used to transfer nanoparticles in Figure 7. It consists of a paper clamp that has been modified with 2 flat objects in order to apply pressure evenly in the center of the paper biosensor. The flat objects are two Eppendorf tube caps that have been glued to the clamp.

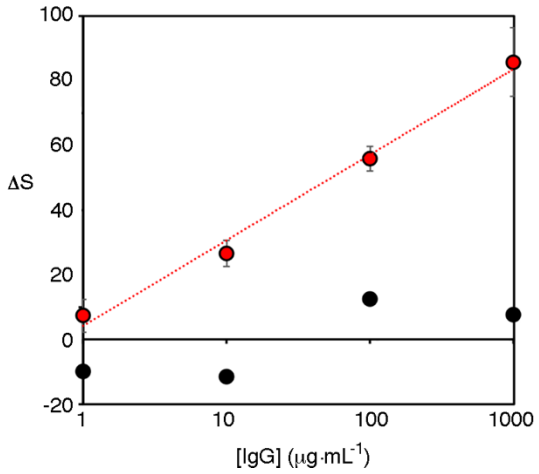

Fig S6 appx 2. Detection of mouse IgG with citrate-capped nanoparticles. Nanoparticles were modified with antibodies with the following procedure based on a previously published protocol [1]. First the pH of the nanoparticle dispersion was adjusted to 9 with sodium bicarbonate (10 mM, pH 11). Then anti-mouse IgG Fc specific (100 μL, 1 mg·mL^{-1}) or anti-*E. coli* (100 μL, 1 mg·mL) was added to the nanoparticles under agitation (1.5 mL, 650 rpm) for 20 min. Subsequently BSA was added to stabilize the colloids (100 μL, 1 mg·mL) for 20 min. The nanoparticles were then centrifuged at 7000 rpm for 6 min and resuspended in 6 μL of PBS-BSA. Nanoparticle reservoirs were prepared by adding 1 μL of nanoparticles to a piece of paper modified with 30% PSS. To prove that the nanoparticles can be transferred and that they retain the ability to specifically recognize their antigen, a receiving paper substrate was modified with mouse IgG (5 μL; 1000, 100, 10, 1 or 0 μg·mL). After drying and blocking with PBSA-BSA (1 mL) the reservoir was pressed against the receiving paper with the aid of the clamp shown in Figure S5. Then the biosensors were washed 3 times with PBST and the images were scanned. The colorimetric signal was calculated as the increase in pixel intensity with respect to the blank experiment with no mouse IgG (DS). In **Fig S6 appx 2** nanoparticles modified with anti-mouse IgG show a concentration-dependent signal (red dots) that is higher than in control experiments with anti-*E. coli* (black dots). This demonstrates that citrate-capped gold nanoparticles modified with antibodies can be stored in the proposed paper reservoirs. Error bars are the standard deviation of 3 independent experiments.

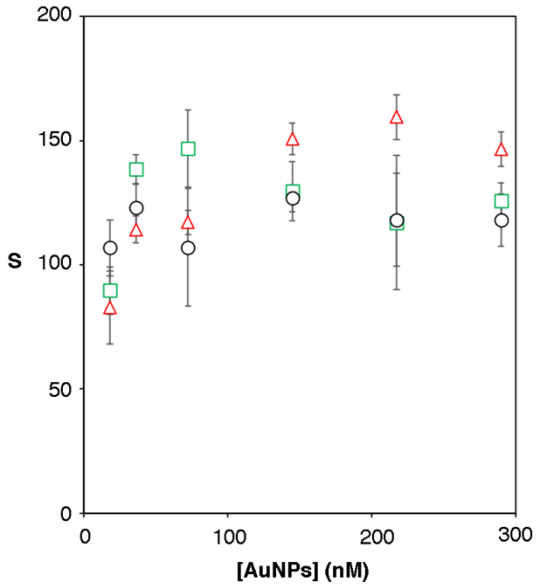

Fig S7 appx 2. Specific signal obtained from transfer experiments in **Fig. 5.6**. The signal S was obtained by subtracting the signal of control experiments performed with nonbiotinylated BSA. Error bars are the standard deviation of 3 independent experiments, and therefore indicate a 90% confidence level. In this Figure, the specific signal was the highest when the receiving paper was Whatman paper #41 (red triangles) and the nanoparticles were stored in the reservoir with a concentration between 140 and 290 nM. The highest specific signal when nanoparticles were stored at a concentration of 36 or 72 nM was achieved with Whatman paper # 1 (green squares). Specific signals obtained with Whatman paper #6 are lower, or not significantly different from those obtained with other paper types (black circles, $p>0.05$).

Reference

[1] Simple paper architecture modifications lead to enhanced sensitivity in nanoparticle based lateral flow immunoassays Claudio Parolo, Mariana Medina-Sánchez et al. Lab on a Chip, 13, 3, 1 2013.

9.3 Appendix 3. Supplementary information for: PAPER BIOSENSORS FOR DETECTING ELEVATED IL-6 LEVELS IN BLOOD AND RESPIRATORY SAMPLES FROM COVID-19 PATIENTS

Table S1 appx 3: Limit of detection (LOD) and dynamic range of previously proposed biosensors for IL-6 detection

				Instrumental			
Ref	**Technique**	**Detection**	**Support**	**LOD**	**Matrix**	**Dynamic range**	**Analysis time**
[193]	Aptamers	Conductance	Carbon nanotube	1 pg mL^{-1}	PBS	1 pg mL^{-1} – 10 ng mL^{-1}	Real-time
[196]	Immunosensor aptamer	Electrochemical	Organic Field Effect Transistors	20 pg mL^{-1}	PBS	20 pg mL^{-1} – 210 ng mL^{-1}	-
[192]	Immunosensor	ELISA	Ultrafiltration regenerated cellulose membranes (RC)	31 pg mL^{-1}	PBS	31-500 pg mL^{-1}	2 h
[91]	Immunosensor	Naked eye Optical spectroscopy	Magnetic nanoparticles (MNPs) and polystyrene (PS) microparticles	11 pg mL^{-1} eye 1.2 pg mL^{-1} instr	PBS	3.7 - 900 pg mL^{-1}	1 h
[83]	Immunosensor	Chemiluminescence	Polydimethylsiloxane (PDMS)	1 pg mL^{-1}	PBS (30% fetal calf serum)	5 - 1280 pg mL^{-1}	90 min
[201]	Immunosensor	Localized-surface plasmon resonance (LSPR)	Gold nanorod	10 pg mL^{-1}	PBS	10–10 000 pg mL^{-1}	30 min
[198]	Immunosensor	Electrochemical	Silicon nanowire field effect transistor	-	PBS	5 - 50000 pg mL^{-1}	Real-time
[243]	Immunosensor	Fluorescence	Optical fiber	0.1 pg mL^{-1}	PBS	0.4 - 400 pg mL^{-1}	60 min
[135]	Immunosensor	Electrochemical	Graphene oxides	5 pg mL^{-1}	PBS	5−150 pg mL^{-1}	30 min
[194]	Immunosensor	Electrochemical	Gold electrode	220 pg mL^{-1}	PBS	-	60 min 10 s signal
[191]	Immunosensor	Electrochemical	Gold electrode	4 pg mL^{-1}	PBS	-	>110 min
[195]	Oligonucleotides and antibodies	Optical	Silica wafers coated with Ti/Au	88 µg mL^{-1}	PBS and SSC	-	-
[244]	Immunosensor	Surface-enhanced Raman scattering (SERS)	Paper and DTNB on gold nano shell with a silica core	1 pg mL^{-1}	PBS	1 pg mL^{-1} – 1 µg mL^{-1}	-
[190]	Aptasensor	Electrochemical	Glassy carbon electrode	1.6 pg mL^{-1}	PBS	5 pg mL^{-1} – 100 ng mL^{-1}	>60 min

			with p-aminobenzoic acid, p-aminothiophenol and AuNPs				
[190]	Immunosensor	Electrochemical	Magnetic microparticles and planar graphite-screen printed electrodes	0.3 pg mL^{-1}	PBS	1 pg mL^{-1} – 1 µg mL^{-1}	30 - 60 min
[89]	Immunosensor	Fluorescence	Nitrocellulose PVC Glass fiber	0.37 pg mL^{-1}	PBST-BSA	2–500 pg mL^{-1}	15 min
[136]	Immunosensor	Fluorescence spectroscopy	Nitrocellulose	0.9 pg mL^{-1}	PBS	1-1000 pg mL^{-1}	30 min
[130]	Aptameric GFET (field effect transistor)	Electrochemical	Graphene	210 pg mL^{-1}	PBS	1 - 16 ng mL^{-1}	6 min
[131]	Immunosensor	Differential pulse voltammetry	TI:Au on silicon subtrate	20 pg mL^{-1}	PBS	0 - 60 pg mL^{-1}	2.5 min
[84]	Immunosensor	Chemiluminescence	Optical fiber	1.05 pg mL^{-1}	PBS	5 to 10 000 pg mL^{-1}	>75 min
[200]	Immunosensor	Electrochemical	Indium tin oxide (ITO) electrode	6.0 fg mL^{-1}	PBS	0.02–16 pg mL^{-1}	>30 min
[189]	Immunosensor	Colorimetric	Plasmonic nanoprobes and paper	0.1 pg mL^{-1}	PBS	---	17 min
[245]	Immunosensor	Localized-surface plasmon resonance (LSPR)	Poly(pyrrole N-hydroxy succinimide)	10 fg mL^{-1}	PBS	0.03 - 22.5 pg mL^{-1}	-
[23]	Multiplexed immunosensor	LSPR	glass	11.29 pg mL^{-1}	PBS	10 – 10^4 pg mL^{-1}	40 min
[24]	Microfluidic immunoarray	electrochemical	gold	0.05 to 2 pg mL^{-1}	serum	sub pg mL^{-1} to well above ng mL^{-1})	<60 min
This work	**Immunosensor**	**Colorimetric**	**Paper/AuNPs**	**10^{-3} pg mL^{-1}**	**PBS**	**10^{-3}–10^{2} pg mL^{-1}**	**7-8 min**

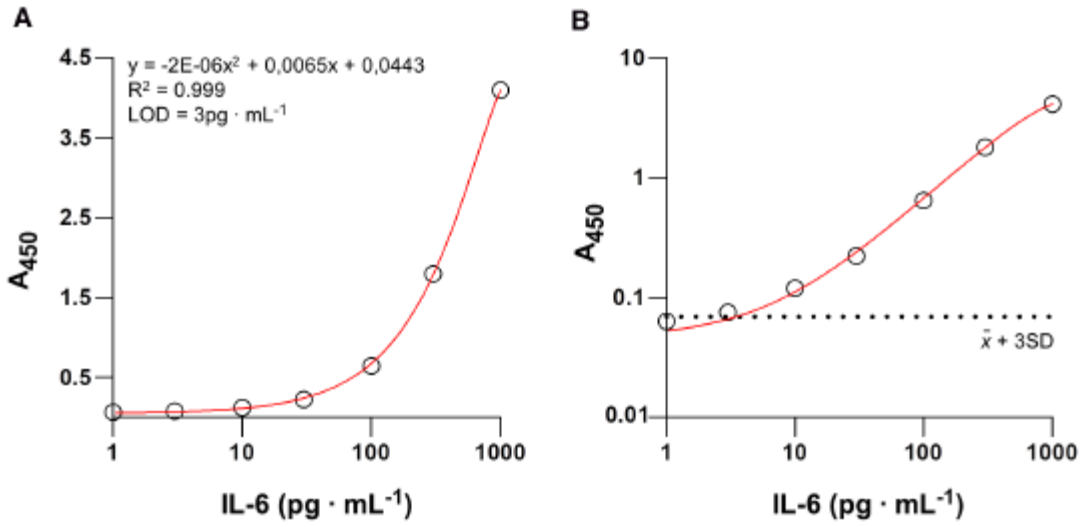

Fig S1 appx 3. Calibration plot for IL-6 detection with an in-house ELISA in semi-logarithmic (A) or log-log (B) scale. The calibration plot was obtained as follows. A 96-well ELISA microplate (Thermo Scientific) was coated with 100 µl of mouse anti-human interleukin-6 (IL-6) monoclonal capture antibody (Abcam) at 1 µg·mL-1 in bicarbonate buffer (0.1 M, pH 9.6). After overnight incubation at 4 ºC, wells were washed 3 times with PBS containing 0.1% Tween 20 (PBST), blocked during 2 h at 37 ºC with PBS containing 2% of bovine serum albumin (BSA) and washed again 3 times with PBST. The calibration curve was obtained by adding 100 µl of IL-6 solutions to coated wells and incubated 2h at room temperature (RT) in a swinging shaker. IL-6 solutions were also applied to wells without capture antibodies in order to subtract nonspecific signals. Each sample was assayed in triplicate. Next, plates were washed 3 times with PBST and then 100 µL of biotinylated mouse anti-human IL-6 monoclonal detection antibody (Sigma-Aldrich) at 10 µg·mL-1 in PBST-BSA 1% was added. After 2h of incubation at RT in a swinging shaker, plates were washed 5 times with PBST and 100 µL of streptavidin-HRP diluted 1:1000 in 1% PBST-BSA was added for 30 min at RT. Then, plates were washed again 5 times with PBST and 100 µL of ready-to-use 1-Step Ultra TMB (Thermo Scientific) was added for 30 min at RT. Finally, the colorimetric reaction was stopped with 100 µL of 2N H2SO4, and absorbance was measured at 450 nm. Absorbance was read with a Biotek power wave plate reader. The limit of detection expressed as the sample that yields a signal above three times the standard deviation of the blank is 3 pg·mL^{-1}.

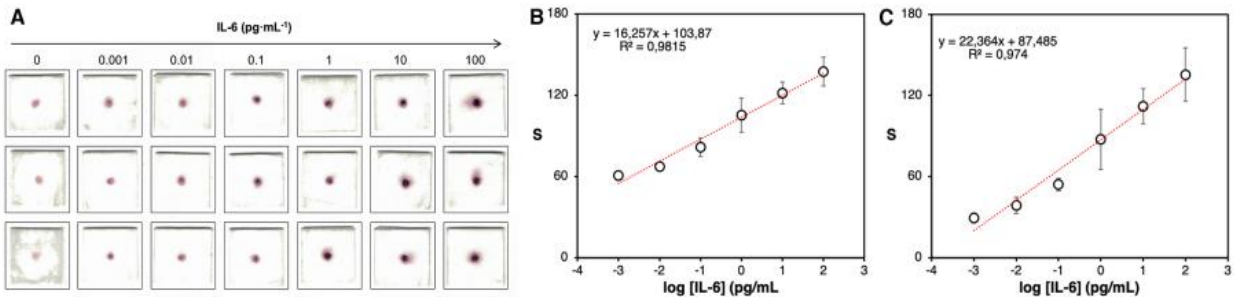

Fig S2 appx 3. Calibration plot with IL-6 diluted in PBS-BSA (40 µg mL^{-1}) instead of in PBS. (A) Scanned images of the paper biosensors; (B) Calibration plot obtained via densitometric

analysis of images in (A) with ImageJ; Sblank + 3s = 59; (C) Calibration plot obtained when measuring the colorimetric signal of the same assays with our app; Sblank + 3s = 23. Error bars are the standard deviation of the three independent experiments.

References

[1] Khosravi, F.; Loeian, S. M.; Panchapakesan, B. Ultrasensitive Label-Free Sensing of IL-6 Based on PASE Functionalized Carbon Nanotube Micro-Arrays with RNA-Aptamers as Molecular Recognition Elements. Biosensors 2017, 7 (2). https://doi.org/10.3390/bios7020017.

[2] Diacci, C.; Berto, M.; Di Lauro, M.; Bianchini, E.; Pinti, M.; Simon, D. T.; Biscarini, F.; Bortolotti, C. A. Label-Free Detection of Interleukin-6 Using Electrolyte Gated Organic Field Effect Transistors. Biointerphases 2017, 12 (5), 05F401. https://doi.org/10.1116/1.4997760.

[3] Militano, F.; Poerio, T.; Mazzei, R.; Salerno, S.; Bartolo, L. De; Giorno, L. Development of Biohybrid Immuno-Selective Membranes for Target Antigen Recognition. Biosens. Bioelectron. 2017, 92 (November 2016), 54–60. https://doi.org/10.1016/j.bios.2017.02.003.

[4] Yin, B.; Zheng, W.; Dong, M.; Yu, W.; Chen, Y.; Joo, S. W.; Jiang, X. An Enzyme-Mediated Competitive Colorimetric Sensor Based on Au@Ag Bimetallic Nanoparticles for Highly Sensitive Detection of Disease Biomarkers. Analyst 2017, 142 (16), 2954–2960. https://doi.org/10.1039/c7an00779e.

[5] Wu, J.; Chen, Y.; Yang, M.; Wang, Y.; Zhang, C.; Yang, M.; Sun, J.; Xie, M.; Jiang, X. Streptavidin-Biotin-Peroxidase Nanocomplex-Amplified Microfluidics Immunoassays for Simultaneous Detection of Inflammatory Biomarkers. Anal. Chim. Acta 2017, 982, 138–147. https://doi.org/10.1016/j.aca.2017.05.031.

[6] Zhu, J.; He, J.; Verano, M.; Brimmo, A. T.; Glia, A.; Qasaimeh, M. A.; Chen, P.; Aleman, J. O.; Chen, W. An Integrated Adipose-Tissueon-Chip Nanoplasmonic Biosensing Platform for Investigating Obesity-Associated Inflammation. Lab Chip 2018, 18 (23), 3550–3560. https://doi.org/10.1039/c8lc00605a.

[7] Chen, H.; Li, J.; Zhang, X.; Li, X.; Yao, M.; Zheng, G. Automated in Vivo Nanosensing of Breath-Borne Protein Biomarkers. Nano Lett. 2018, 18 (8), 4716–4726. https://doi.org/10.1021/acs.nanolett.8b01070.

[8] Zhang, K.; Liu, G.; Goldys, E. M. Robust Immunosensing System Based on Biotin-Streptavidin Coupling for Spatially Localized Femtogram ML^{-1} Level Detection of Interleukin-6. Biosens. Bioelectron. 2018, 102, 80–86. https://doi.org/10.1016/j.bios.2017.11.023.

[9] Wei, H.; Ni, S.; Cao, C.; Yang, G.; Liu, G. Graphene Oxide Signal Reporter Based Multifunctional Immunosensing Platform for Amperometric Profiling of Multiple Cytokines in Serum. ACS Sensors 2018, 3 (8), 1553–1561. https://doi.org/10.1021/acssensors.8b00365.

[10] Gentili, D.; D'Angelo, P.; Militano, F.; Mazzei, R.; Poerio, T.; Brucale, M.; Tarabella, G.; Bonetti, S.; Marasso, S. L.; Cocuzza, M.; et al. Integration of Organic Electrochemical Transistors and Immuno-Affinity Membranes for Label-Free Detection of Interleukin-6 in the Physiological Concentration Range through Antibody-Antigen Recognition. J. Mater. Chem. B 2018, 6 (33), 5400–5406. https://doi.org/10.1039/c8tb01697f.

[11] Sabaté, J.; Henry, O. Y. F.; Jolly, P.; Ingber, D. E. An Antifouling Coating That Enables Affinity-Based Electrochemical Biosensing in Complex Biological Fluids. Nat. Nanotechnol. 2019, 14 (December), 1143–1149. https://doi.org/10.1038/s41565-019-0566-z.

[12] Fabri-Faja, N.; Calvo-Lozano, O.; Dey, P.; Terborg, R. A.; Estevez, M. C.; Belushkin, A.; Yesilköy, F.; Duempelmann, L.; Altug, H.; Pruneri, V.; et al. Early Sepsis Diagnosis via Protein and MiRNA Biomarkers Using a Novel Point-of-Care Photonic Biosensor. Anal. Chim. Acta 2019, 1077, 232–242. https://doi.org/10.1016/j.aca.2019.05.038.

[13] Wang, Y.; Sun, J.; Hou, Y.; Zhang, C.; Li, D.; Li, H.; Yang, M.; Fan, C.; Sun, B. A SERS-Based Lateral Flow Assay Biosensor for Quantitative and Ultrasensitive Detection of Interleukin-6 in Unprocessed Whole Blood. Biosens. Bioelectron. 2019, 141 (June), 111432. https://doi.org/10.1016/j.bios.2019.111432.

[14] Tertis, M.; Ionut, P.; Bogdan, D.; Suciu, M.; Graur, F.; Cristea, C. Biosensors and Bioelectronics Impedimetric Aptasensor for the Label-Free and Selective Detection of Interleukin-6 for Colorectal Cancer Screening. Biosens. Bioelectron. 2019, 137 (April), 123–132. https://doi.org/10.1016/j.bios.2019.05.012.

[15] Huang, D.; Ying, H.; Jiang, D.; Liu, F.; Tian, Y.; Du, C.; Zhang, L.; Pu, X. Rapid and Sensitive Detection of Interleukin-6 in Serum via Time-Resolved Lateral Flow Immunoassay. Anal. Biochem. 2020, 588 (October 2019), 113468. https://doi.org/10.1016/j.ab.2019.113468.

[16] Borse, V.; Srivastava, R. Fluorescence Lateral Flow Immunoassay Based Point-of-Care Nanodiagnostics for Orthopedic Implant-Associated Infection. Sensors Actuators, B Chem. 2019, 280, 24–33. https://doi.org/10.1016/j.snb.2018.10.034.

[17] Hao, Z.; Pan, Y.; Shao, W.; Lin, Q.; Zhao, X. Graphene-Based Fully Integrated Portable Nanosensing System for on-Line Detection of Cytokine Biomarkers in Saliva. Biosens. Bioelectron. 2019, 134, 16–23. https://doi.org/10.1016/j.bios.2019.03.053.

[18] Russell, C.; Ward, A. C.; Vezza, V.; Hoskisson, P.; Alcorn, D.; Steenson, D. P.; Corrigan, D. K. Development of a Needle Shaped Microelectrode for Electrochemical Detection of the Sepsis Biomarker Interleukin-6 (IL-6) in Real Time. Biosens. Bioelectron. 2019, 126, 806–814. https://doi.org/10.1016/j.bios.2018.11.053.

[19] Nie, R.; Huang, J.; Xu, X.; Yang, L. A Portable Pencil-like Immunosensor for Point-of-Care Testing of Inflammatory Biomarkers. Anal. Bioanal. Chem. 2020, 412, 3231–3239. https://doi.org/https://doi.org/10.1007/s00216-020-02582-z.

[20] Aydın, E. B. Highly Sensitive Impedimetric Immunosensor for Determination of Interleukin 6 as a Cancer Biomarker by Using Conjugated Polymer Containing Epoxy Side Groups Modified Disposable ITO Electrode. Talanta 2020, 215, 120909. https://doi.org/10.1016/j.talanta.2020.120909.

[21] Alba-Patiño, A.; Russell, S. M.; Borges, M.; Pazos-Perez, N.; Alvarez-Puebla, R. A.; de la Rica, R. Nanoparticle-Based Mobile Biosensors for the Rapid Detection of Sepsis Biomarkers in Whole Blood. Nanoscale Adv. 2020, 2, 253–1260. https://doi.org/10.1039/d0na00026d.

[22] Aydın, E. B.; Aydın, M.; Sezgintürk, M. K. The Development of an Ultra-Sensitive Electrochemical Immunosensor Using a PPyr-NHS Functionalized Disposable ITO Sheet for the Detection of Interleukin 6 in Real Human Serums. New J. Chem. 2020. https://doi.org/10.1039/d0nj03183f.

[23] Chen, P.; Chung, M. T.; McHugh, W.; Nidetz, R.; Li, Y.; Fu, J.; Cornell, T. T.; Shanley, T. P.; Kurabayashi, K. Multiplex Serum Cytokine Immunoassay Using Nanoplasmonic Biosensor Microarrays. ACS Nano 2015, 9 (4), 4173–4181. https://doi.org/10.1021/acsnano.5b00396.

[24] Tang, C. K.; Vaze, A.; Shen, M.; Rusling, J. F. High-Throughput Electrochemical Microfluidic Immunoarray for Multiplexed Detection of Cancer Biomarker Proteins. ACS Sensors 2016, 1 (8), 1036–1043. https://doi.org/10.1021/acssensors.6b00256.

9.4 Appendix 4. Supplementary methods and results for: RAPID DETECTION OF PSEUDOMONAS AERUGINOSA BIOFILMS VIA ENZYMATIC LIQUEFACTION OF RESPIRATORY SAMPLES.

ELISA for *P. aeruginosa*

ELISA protocol: 100 µL of samples containing *P. aeruginosa* was added to a 96-well ELISA plates and dried by overnight incubation at 37 ºC on a heating plate. Next, plates were washed 3 times with PBS containing 0.1% Tween 20 (PBST), blocked during 2 h at room temperature (RT) with PBS containing 5 mg·mL-1 bovine serum albumin (BSA) and washed again 3 times with PBST. Then, 100 µL of primary anti-*Pseudomonas* mouse IgG monoclonal antibody (Abcam) diluted 1:600 in PBST was added and incubated for 1 h at RT. After washing 5 times with PBST, 100 µL of secondary biotinylated anti-mouse IgG (Fc specific) produced in goat (ThermoFisher, 1:3000 in PBST) was added for 1 h at RT. After washing 5 times, 100 µL of streptavidin-HRP diluted 1:3000 in PBST was added for 30 min at RT. Subsequently, the plates were washed 5 times with PBST and 100 µL of 100 µg/mL of TMB (3,3',5,5'-Tetramethylbenzidine, Sigma) with 1.2 mM of H2O2 in 50 mM acetate buffer (pH 5.0) was added for 5 min at RT. Finally, the colorimetric reaction was stopped with 100 µL of 2N H_2SO_4 and absorbance was measured at 450 nm.

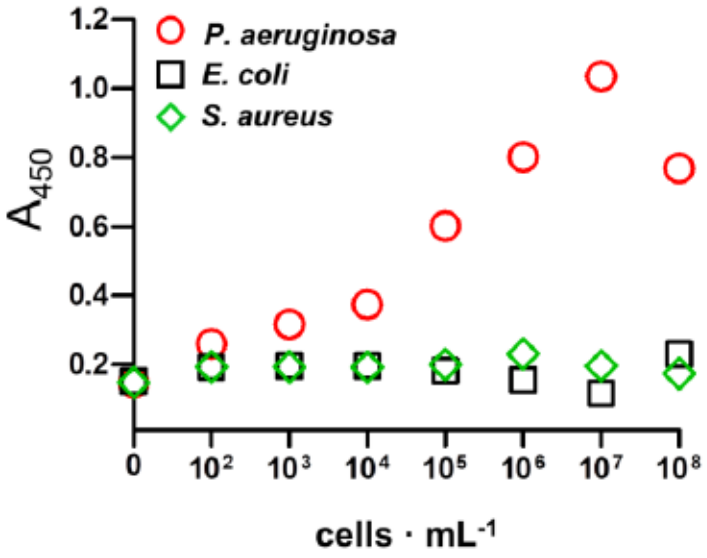

Fig S1 appx 4. Detection of *P. aeruginosa* with ELISA; Absorbance with respect to the concentration of *P. aeruginosa* (red dots), *E. coli* (black squares) or *S. aureus* (green diamonds) after following the proposed ELISA protocol for *P. aeruginosa* detection using bacterial suspensions in PBS.

Fig S1 appx 4 shows a calibration plot using solutions containing known concentrations of *P. aeruginosa* and *E. coli* or *S. aureus* as controls. Experiments with increasing concentrations of *P. aeruginosa* show a concentration-dependent signal, whereas the signal in control 3 experiments remains constant. These experiments validate the proposed ELISA for the specific detection and quantification of *P. aeruginosa* antigens.

To demonstrate that bacterial antigens are released from the plate by the H_2O_2-mediated generation of bubbles (**Fig. 7.3**D), the plates were rinsed after biofilm formation and 175 µL of PBS containing H2O2 in the concentration range between 0.01 M to 1 M was added. After 1, 3 or 5 min, 100 µL of the resulting samples was collected and kept at -20 °C until analyzed with the ELISA protocol shown above. Results are shown in **Fig. 7.3** in the main text and in **Fig S3 appx 4**.

Impact of H_2O_2 treatment on antibody-antigen interactions

100 µL of solutions containing known concentrations of *P. aeruginosa* were added to a 96-well ELISA plates and left to dry. After washing and blocking as detailed in the last section, 100 µL of primary anti-*Pseudomonas* mouse IgG monoclonal antibody (Abcam) diluted 1:600 in PBST with increasing concentrations of hydrogen peroxide between 0.01M and 1M was added for 1 h at RT. Subsequent ELISA steps were performed as before.

In **Fig S2 appx 4** there is a light decrease in signal when the concentration of H_2O_2 is 0.3 M and the concentration of bacteria is 10^6 cells·mL^{-1} or higher. This decrease is more pronounced when the concentration of H_2O_2 is 1 M. These experiments show that adding an excess of H_2O_2 may impair antibody-antigen interactions in sandwich-type ELISA.

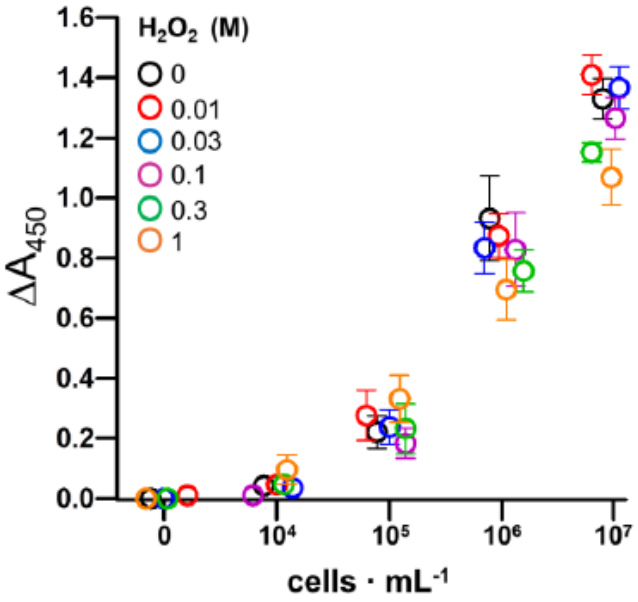

Fig S2 appx 4. Evaluation of the impact of H_2O_2 treatment on antibody-antigen interactions; Absorbance with respect to the concentration of *P. aeruginosa* detected by a modified ELISA protocol in which the primary monoclonal antibody against *P. aeruginosa* is incubated in the presence of hydrogen peroxide at 0 M (black), 0.01 M (red), 0.03 M (blue), 0.1 M (purple), 0.3 M (green) or 1 M (orange). Error bars are the standard deviation (n = 5). Data are expressed as the increase in absorbance (ΔA) with respect to the wells without bacteria for each experimental condition.

Impact of incubation time with H_2O_2 on antigen release from biofilms.

Fig S3 appx 4 shows ELISA performed in the same conditions as the experiment in **Fig. 7.3**D but adding H_2O_2 for 3 or 5 min. Increasing the incubation time with H_2O_2 increases the ELISA signal at low concentrations of peroxide. However, the signal is the same when H_2O_2 is added to a final concentration of 0.3 M regardless of the incubation time. Since our aim is to disrupt the biofilms as rapidly as possible, and adding 0.3 M H_2O_2 has a small impact on antibody-interactions (**Fig S2 appx 4**), an incubation time of 60 s with 0.3 M H_2O_2 was chosen as optimal for posterior experiments involving the detection of *P. aeruginosa* in respiratory samples.

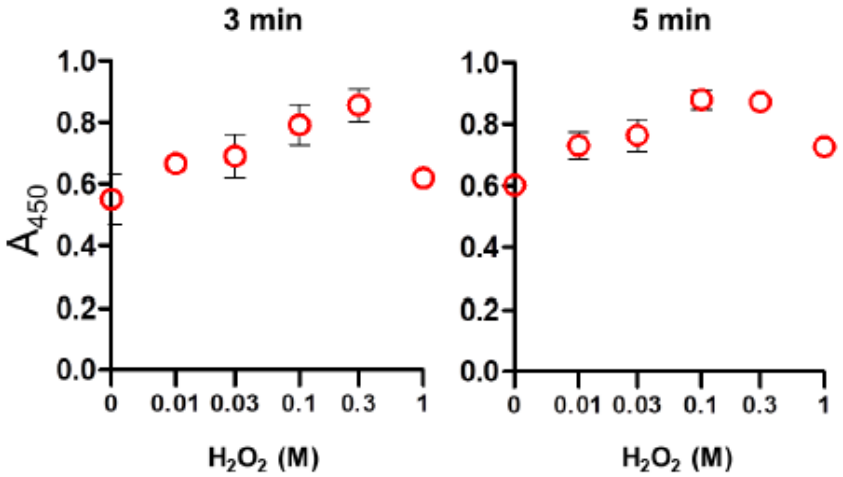

Fig S3 appx 4. Influence of incubation time with H_2O_2 on bacterial antigens release; Absorbance measured after releasing bacterial antigens from biofilms using H_2O_2 at different concentrations for 3 min (left) or 5 min (right), following the proposed ELISA protocol to detect *P. aeruginosa*. Error bars are the standard deviation (n = 6).

H2O2 effect on microstructure and cell viability of P. aeruginosa biofilms evaluated by CLSM

We performed confocal laser scanning microscopy (CLSM) experiments to observe with higher resolution the biofilm microstructure and the integrity of the bacterial membranes after

hydrogen peroxide addition (**Fig S4 appx 4**). After growing *P. aeruginosa* control biofilms or Fedeprived biofilms for 24 hours in micro-slides for CLSM observations, as detailed in the methods section of the main text and S5-S6, cells were died by a double staining procedure with SYTO9 and Propidium iodide using the FilmTracer LIVE/DEAD Biofilm Viability Kit (Invitrogen). Then, CLSM images were obtained with a LSM 710 confocal microscope (Carl Zeiss) previously and after 0.3 M H_2O_2 treatment by using 63X oil immersion objective lenses.

In **Fig S4 appx 4** confocal 3D images of biofilms show the intense fluorescent signal of SYTO9 dye (green) and negligible signal of Propidium iodide (red) in biofilms grown in the absence or presence of Fe chelator (**Fig S4 appx 4**(i-ii)) indicating a high density of viable cells within biomass. After addition of 0.3 M H2O2 the green signal drastically decreases in control biofilms without Fe deprivation (**Fig S4 appx 4**(i-iii) but remains unaltered in those grown in the presence of Fe chelator (**Fig S4 appx 4**(ii-iv). In contrast, the red signal is absent when H_2O_2 is added in both cases (**Fig S4 appx 4**(iii-iv)). This experiment demonstrates that when catalase generates bubbles by the hydrolysis of H_2O_2 the biofilm architecture is deeply disrupted and that this disruption can be prevented if catalase activity is inhibited. Cell viability is conserved, reinforcing the idea that biofilm disruption is originated by the generation of bubbles and not by the biocide action of H_2O_2.

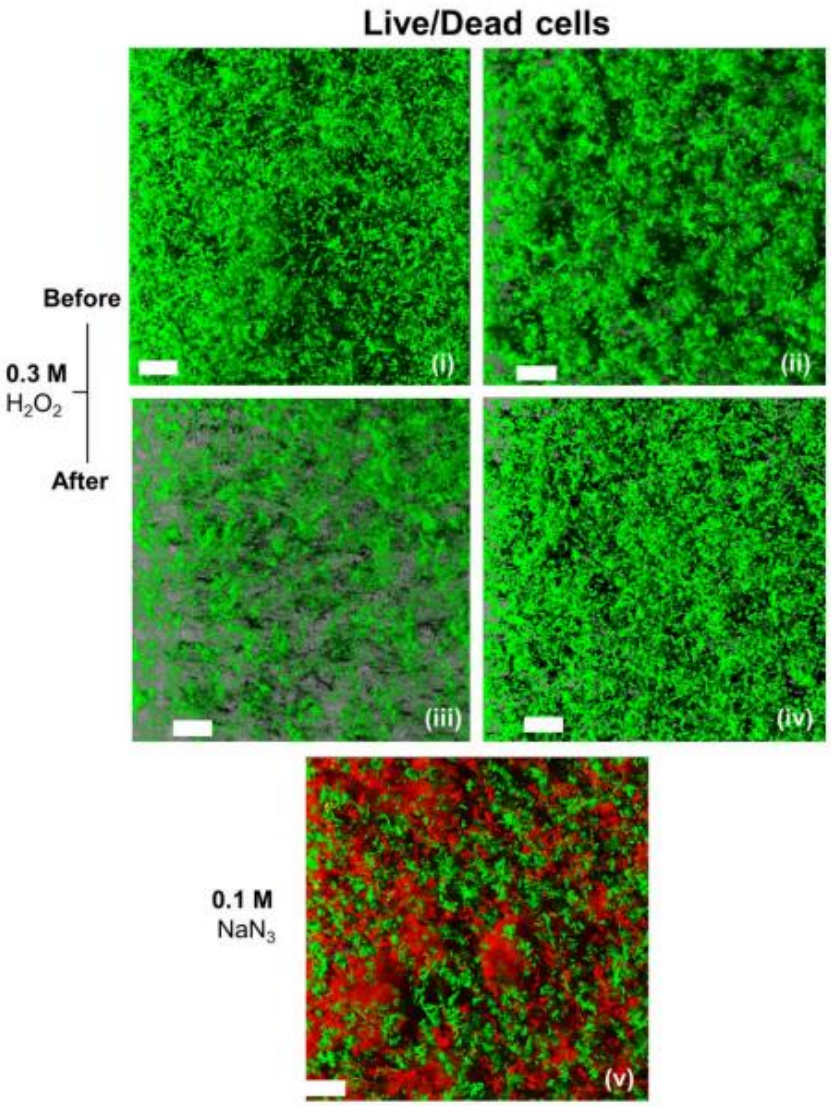

Fig S4 appx 4. *P. aeruginosa* biofilm microstructure and bacterial membrane integrity after H_2O_2 treatment; 3D confocal imaging before (i-ii) and after (iii-iv) 0.3 M H_2O_2 treatment in control biofilms (left) and biofilms with low catalase activity grown in the presence of 0.25 mM 2-2'- Bipyridyl as Fe chelator (right) for 24 hours. 3D confocal imaging after adding 0.1 M NaN_3 (v) as positive control of membrane integrity loss (cell death) in a control biofilm. Green (SYTO9) and red (Propidium iodide) colours indicate the presence of live and dead cells respectively. Scale bar: 15 μm.

Biofilms grown under Fe starvation conditions.

When *P. aeruginosa* biofilms are grown in the presence of a chelating agent the resulting Fe starvation condition decreases the catalase activity of the bacteria [20]. With this in mind, we designed experiments to prove that catalase activity is responsible for release of antigens shown in **Fig. 7.3**D. PAO1 strain of *P. aeruginosa* was inoculated into 96-well round

bottom plates filled with 100 µL of LB broth culture supplemented with the chelating agent 2,2'-bypiridyl (Sigma) to increasing final concentrations between 0.125 mM and 1.75 mM. Then, plates were incubated 24 h in a 5% CO_2 atmosphere and 37 ºC until biofilms were formed. Next, we followed the protocol for *in vitro* disruption of *P. aeruginosa* biofilms (detailed in the methods section of the main text) and evaluated the antigen release by ELISA as explained before.

When biofilms were formed under Fe limitation conditions the production of bubbles after addition of H_2O_2 decreases, as shown in **Fig S4 appx 4**A, which shows that catalase activity is reduced. We analyzed the bacterial membrane permeability by a propidium iodide staining protocol (detailed in the methods section of the main text) in order to evaluate the extent to which catalase activity can be inhibited without increasing cell death susceptibility against hydrogen peroxide. To this end, we applied the 0.3 M H_2O_2 treatment for 60 s and then we analyzed the membrane permeability. In **Fig S4 appx 4**B adding H_2O_2 has no effect when the concentration of 2,2'-bypiridyl is 0.5 mM. However, at higher concentrations the cell permeability increases as the concentration of chelating agent increases because catalase activity is reduced, and therefore the cells are more susceptible to the biocide action of H_2O_2.

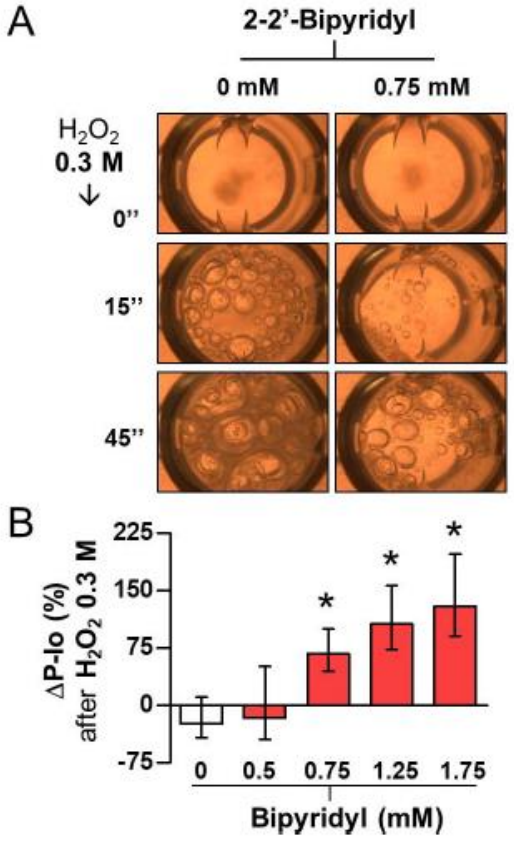

Fig S5 appx 4. Effect of Fe starvation on bubble production (A) and cell death susceptibility (B). (A) Photographs of *P. aeruginosa* biolfims grown in the presence of the Fe chelator 2-2'-Bipyridyl in a 96-well plate after adding H_2O_2 at 0.3 M for 0, 15 and 45 s. (B) Percentage increase of propidium iodide (P-Io) fluorescence intensity (cell death) after adding H2O2 at 0.3 M for 60 s to biofilms grown in the presence of increasing concentrations of Fe chelator. Data are expressed as medians with interquartile range (n = 24). *p-value < 0.05 obtained with a Kruskall-wallis test.

To prove that catalase activity is responsible for releasing antigens, we quantified the concentration of antigens in supernatants after adding hydrogen peroxide to biofilms grown under optimal conditions to preserve cell survival (<0.5 mM chelating agent, **Fig S4 appx 4**B). Inhibiting catalase activity under this condition decreases the ELISA signal in **Fig S5 appx 4**A, which indicates that less antigens are being released from the biofilm. The following experiment was performed to demonstrate that the lower ELISA signal is originated by a reduction in antigen release and not by variations in the biomass of the biofilm induced by the Fe starvation protocol. Briefly, Fe-starved biofilms were decanted in order to remove all planktonic cells and flocs and washed 3 times by immersion in sterile PBS. Then, 125 µL of 0.1% crystal violet was added to empty wells containing adherent biofilms and plates were incubated for 15 min at RT. Finally, stained biofilms were washed 3 times again and dissolved for 10 min with 200 µL of 30% acetic acid prior to biomass quantification by measuring the absorbance at 590 nm. In Fig. S5B the biomass of biofilms is not altered when the chelating agent is added at the concentration used in **Fig S5 appx 4**A. Since the biomass (**Fig S5 appx 4**) and susceptibility to the biocide action of H_2O_2 (**Fig S4 appx 4**B) are not significantly altered by the Fe starvation protocol, then the decrease in ELISA in **Fig S5 appx 4**A can be attributed to a decrease in antigen release due to the inhibition of catalase activity in the biofilm. These experiments demonstrate that the formation of bubbles by catalase is the key factor for disrupting biofilms with the proposed method.

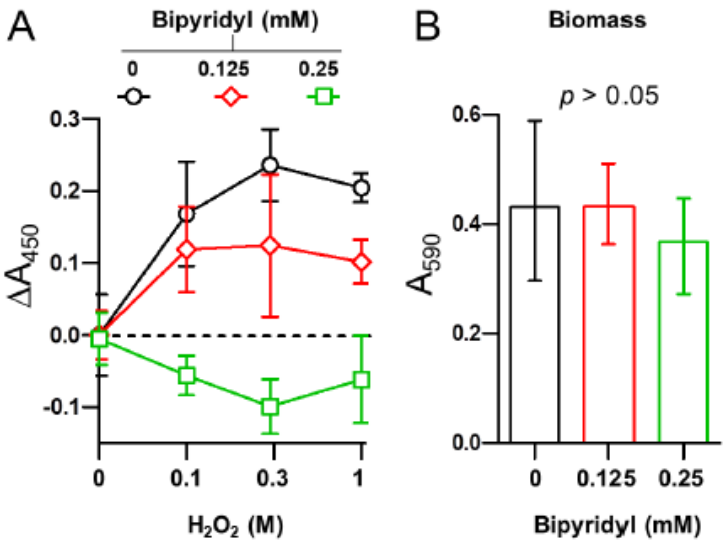

Fig S6 appx 4. Effect of H_2O_2 addition on antigen release (A) and biomass (B) of biofilms grown under Fe starvation conditions (2,2 bipyridyl at 0, 0.125 and 0.25 mM). (A) Absorbance measured after releasing bacterial antigens from biofilms using H_2O_2 at different concentrations for 60 s following the proposed ELISA protocol to detect *P. aeruginosa*. Error bars are the standard deviation (n = 5). Data are expressed as the increase in absorbance (ΔA) at different H2O2 concentrations with respect to the release of bacterial antigens induced by PBS alone (no H2O2). (B) Biomass of *P. aeruginosa* biofilms grown without Fe chelator (black) or under low Fe starvation conditions (green and red). Data are expressed as medians with interquartile range (n = 30). *P*-value was obtained with a Kruskall-wallis test.

Hydrogen peroxide reduction of disulfide bonds

Sputasol (dithiotreitol 6.5 mM) acts as a liquefying agent for sputum samples by reducing disulfide bonds within mucin. We performed an Ellman's test in order to evaluate the reducing properties of hydrogen peroxide under the experimental conditions proposed for our alternative sputum liquefaction protocol. Briefly, 20 µL of 4 mg·mL-1 Ellman's reagent (5,5'-dithiobis-(2-nitrobenzoic acid) or DTNB from Sigma) in Ellman's buffer (0.1 M phosphate supplemented with 1 mM EDTA, pH 7.4) was added to 100 µL of Ellman's buffer with 0.3 M hydrogen peroxide or 0.3 mM dithiotreitol (Sputasol from Oxoid) in a 96-well ELISA plate. The reduction of disulfide bonds within DTNB produces a measurable colorimetric reaction. After 15 min of incubation at RT 80 µL of Ellman's buffer was added to wells and the yellow-colored product was measured at 412 nm, following the instructions provided by the manufacturer.

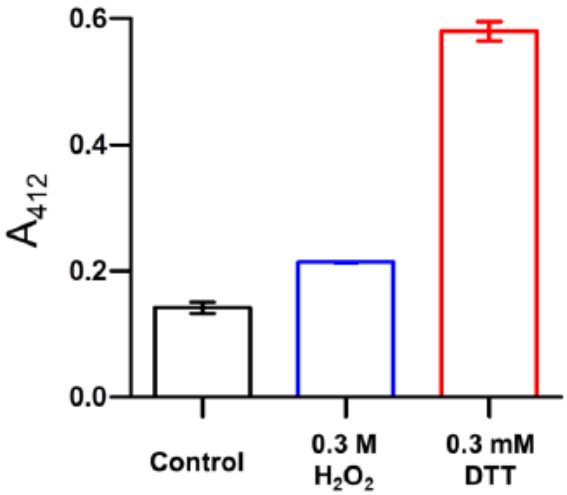

Fig S7 appx 4. Ellman's reagent reduction by hydrogen peroxide and dithiotreitol. Plot representing the absorbance after adding Ellman's reagent to control buffer (black), 0.3 M H_2O_2 (blue) and 0.3 mM dithiotreitol (DTT, red). Error bars are the standard deviation (n = 3).

In **Fig S6 appx 4** the addition of 0.3 M H_2O_2 has little effect compared to the experiment performed in the presence of 0.3 mM DTT. It should be noted that 0.3 mM DTT is 20 times less concentrated than Sputasol; this dilution was necessary in order to obtain a quantifiable signal with the Ellman test. These experiments demonstrate that 0.3 M H_2O_2 has negligible reducing power compared to 6.5 mM DTT, which is the standard procedure for liquefying sputum samples. Therefore, these results demonstrate that the main factor for the rapid liquefaction of respiratory samples with the proposed method is the generation of bubbles by the enzyme catalase and not the reduction of disulfide bonds by H_2O_2.

Detection of *P. aeruginosa* with immunosensors and a scanner

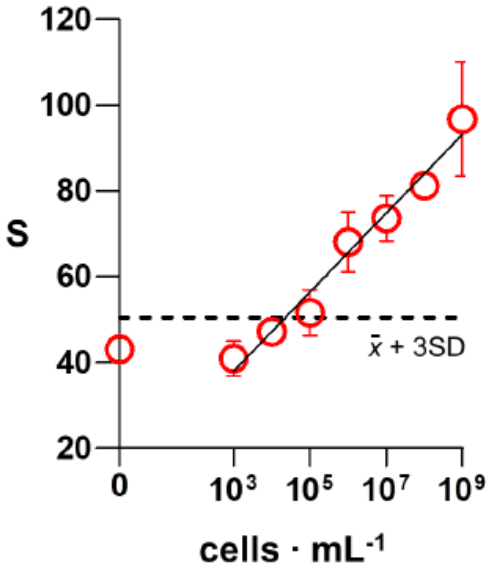

Fig S8 appx 4. Detection of *P. aeruginosa* with immunosensors and a scanner instead of with the mobile app; Calibration plot representing the colorimetric signal S with respect to the concentration of *P. aeruginosa* (red dots) measured by scanning the paper biosensor with a desktop scanner and quantifying the pixel intensity in grayscale in a circular area within the area of interest with the histogram function of ImageJ. The dotted line shows the signal above 3 times the standard deviation of the blank. Error bars are the standard deviation (n = 3).

Representative images of sputum samples liquefied with 0.3 M H_2O_2 for 60 s

Images shown in **Fig S8 appx 4** show sputum samples after the liquefaction procedure. As shown in **Fig. 7.2** in the main manuscript, sputum samples infected by *P. aeruginosa* are almost completely dissolved, whereas those containing a mixed flora show different degrees of liquefaction and negative samples are almost intact. These results agree well with the idea that the presence of catalase-producing cells in respiratory samples is the key factor for liquefying samples after the addition of hydrogen peroxide.

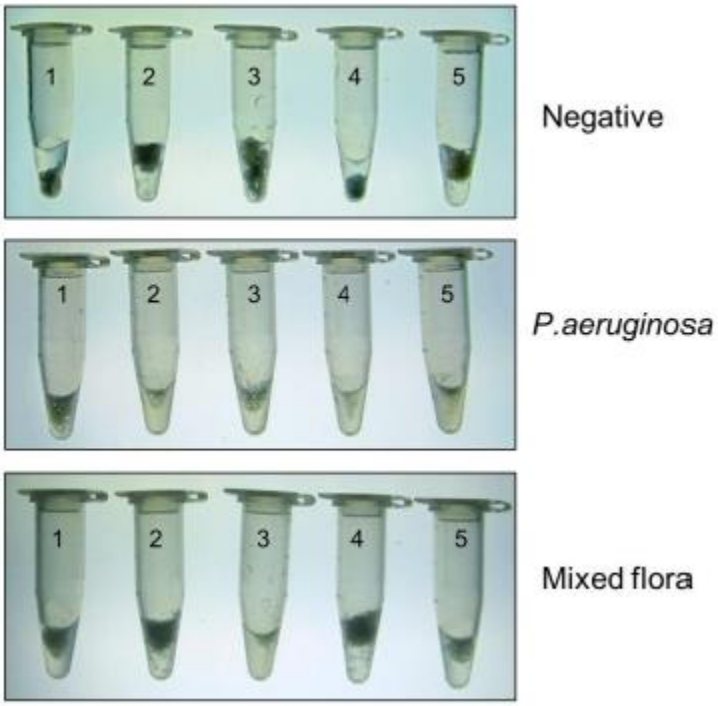

Fig S9 appx 4. Liquefaction of sputum samples. Photographs of sputum samples (10 mg) negative for bacterial infection (upper row) and containing *P. aeruginosa* (middle row) or a mixed flora (lower row), after the addition of 0.3 M H_2O_2 for 60 s.

Table S1 appx 4. Comparison between our immunosensor and other methods to detect *P. aeruginosa.*

	Target	Detection Principle	LOD	Dynamic Range	Sample	Time	Culture required
Alhogail et al[1]	Protease	Colorimetric	10^2 cells/mL	NP	Sputum	1 min	Yes
Thet et al[2]	Toxins	Fluorescence	10^7 -10^8 cells/swab	10^7 -10^8 cells/swab	Wound	2 h	No
Ciui et al[3]	Virulence factors	Electrochemical	NP	NP	Surfaces	4 min	No
Bai et al[4]	Cells	Near-field sensing	NP	0.5-1x10^4 cells/mL	Medium	5 min	NP
Liu et al[5]	Nucleic acid	Colorimetric	10^1 cfu	0 -10 cfu	water	70 min	No
Ferreira e Silva[6]	Pyocyanin	Electrochemical	50-10^3 nM	10 nM	Saliva, water, surfaces	10 min	No
Sheybani[7]	Cells	Electrochemical	10^2 cfu/mL	10^2 -10^6 cfu/mL	Wound	5 min	Yes
Liu et al[8]	Cells	Electrochemical	10^2 cfu/mL	10^2 -10^6 cfu/mL	Tris–HCl buffer	30 min	No
Chen et al[9]	Nucleic acid	Colorimetric	20 cfu/mL	NP	Water, soil	50 min	Yes
Krithiga et al[10]	Cells	Electrochemical	9x10^2 cfu/mL	10^1 -10^7 cfu/mL	buffer	45 min	No
Alatraktchi et al[11]	Pyocyanin	Electrochemical	172 nM	NP	saline, endolaryngeal suctions	1 min	No
Mukama et al[12]	Nucleic acid	Colorimetric	1 cfu/mL	NP	Milk, serum, sputum	50-80 min	No
Elkhawaga et al[13]	Pyocyanin	Electrochemical	500 nM	1.9 - 238 µM	culture	NP	Yes
Maldonado et al[14]	cells	BiMW	49 cfu/mL	8x10^2 -10^7 cfu/mL	PBST	12 min	No
Ji et al[15]	Nucleic acid	SH-SAW	0.28 nM	0.1-10^3 nM	NP	NP	No
Zhao et al[16]	Nucleic acid	Colorimetric	10 fg	NP	sputum	40 min	No
Zhou et al[17]	Nucleic acid	Electrochemical	10 cfu/mL	10^1 -10^8 cfu/mL	Simulated sputum	375 min	No
Das et al[18]	Cells	Electrochemical	60 cfu/mL	6x10^1 - 6x10^7 cfu/mL	water	10 min	No
Peng et al[19]	Cells	Colorimetric	100 cells	NP	Water, serum	60 min	No
This work	Cells	Colorimetric	105 cells/mL	104 -109 cells/mL	sputum	8 min	No

NP: not provided, “Culture” refers whether bacteriological culture was necessary prior to or during the detection.

References

[1] Alhogail, S.; Suaifan, G. A. R. Y.; Bikker, F. J.; Kaman, W. E.; Weber, K.; CiallaMay, D.; Popp, J.; Zourob, M. M. Rapid Colorimetric Detection of Pseudomonas Aeruginosa in Clinical Isolates Using a Magnetic Nanoparticle Biosensor. ACS Omega 2019, 4 (26), 21684–21688. https://doi.org/10.1021/acsomega.9b02080.

[2] Thet, N. T.; Mercer-Chalmers, J. D.; Greenwood, R.; Young, A.; Coy, K.; Booth, S.; Sack, A.; Jenkins, A. T. A. The SPaCE Swab: Point of Care Sensor for Simple and Rapid Detection of Acute Wound Infection. ACS Sensors 2020. https://doi.org/10.1021/acssensors.0c01265.

[3] Ciui, B.; Tertiş, M.; Cernat, A.; Săndulescu, R.; Wang, J.; Cristea, C. Finger-Based Printed Sensors Integrated on a Glove for On-Site Screening of Pseudomonas Aeruginosa Virulence Factors. Anal. Chem. 2018, 90 (12), 7761–7768. https://doi.org/10.1021/acs.analchem.8b01915.

[4] Bai, Z.; Liu, Y.; Kong, R.; Nie, T.; Sun, Y.; Li, H.; Sun, T.; Pandey, C.; Wang, Y.; Zhang, H.; et al. Near-Field Terahertz Sensing of HeLa Cells and Pseudomonas Based on Monolithic Integrated Metamaterials with a Spintronic Terahertz Emitter. ACS Appl. Mater. Interfaces 2020, 12, 35895−35902. https://doi.org/10.1021/acsami.0c08543.

[5] Liu, D.; Zhu, Y.; Li, N.; Lu, Y.; Cheng, J.; Xu, Y. A Portable Microfluidic Analyzer for Integrated Bacterial Detection Using Visible Loop-Mediated Amplification. Sensors Actuators, B Chem. 2020, 310 (February), 127834. https://doi.org/10.1016/j.snb.2020.127834.

[6] Ferreira e Silva, R.; Longo Cesar Paixão, T. R.; Der Torossian Torres, M.; de Araujo, W. R. Simple and Inexpensive Electrochemical Paper-Based Analytical Device for Sensitive Detection of Pseudomonas Aeruginosa. Sensors Actuators, B Chem. 2020, 308 (October 2019), 127669. https://doi.org/10.1016/j.snb.2020.127669.

[7] Sheybani, R.; Shukla, A. Highly Sensitive Label-Free Dual Sensor Array for Rapid Detection of Wound Bacteria. Biosens. Bioelectron. 2017, 92 (July 2016), 425–433. https://doi.org/10.1016/j.bios.2016.10.084.

[8] Liu, X.; Marrakchi, M.; Xu, D.; Dong, H.; Andreescu, S. Biosensors Based on Modularly Designed Synthetic Peptides for Recognition, Detection and Live/Dead Differentiation of Pathogenic Bacteria. Biosens. Bioelectron. 2016, 80, 9–16. https://doi.org/10.1016/j.bios.2016.01.041.

[9] Chen, Y.; Cheng, N.; Xu, Y.; Huang, K.; Luo, Y.; Xu, W. Point-of-Care and Visual 15 Detection of P. Aeruginosa and Its Toxin Genes by Multiple LAMP and Lateral Flow Nucleic Acid Biosensor. Biosens. Bioelectron. 2016, 81, 317–323. https://doi.org/10.1016/j.bios.2016.03.006.

[10] Krithiga, N.; Viswanath, K. B.; Vasantha, V. S.; Jayachitra, A. Specific and Selective Electrochemical Immunoassay for Pseudomonas Aeruginosa Based on Pectin-Gold Nano Composite. Biosens. Bioelectron. 2016, 79, 121–129. https://doi.org/10.1016/j.bios.2015.12.006.

[11] Alatraktchi, F. A. Z. a.; Dimaki, M.; Støvring, N.; Johansen, H. K.; Molin, S.; Svendsen, W. E. Nanograss Sensor for Selective Detection of Pseudomonas Aeruginosa by Pyocyanin

Identification in Airway Samples. Anal. Biochem. 2020, 593 (January), 113586. https://doi.org/10.1016/j.ab.2020.113586.

[12] Mukama, O.; Wu, J.; Li, Z.; Liang, Q.; Yi, Z.; Lu, X.; Liu, Y.; Liu, Y.; Hussain, M.; Makafe, G. G.; et al. An Ultrasensitive and Specific Point-of-Care CRISPR/Cas12 Based Lateral Flow Biosensor for the Rapid Detection of Nucleic Acids. Biosens. Bioelectron. 2020, 159 (November 2019), 112143. https://doi.org/10.1016/j.bios.2020.112143.

[13] Elkhawaga, A. A.; Khalifa, M. M.; El-Badawy, O.; Hassan, M. A.; El-Said, W. A. Rapid and Highly Sensitive Detection of Pyocyanin Biomarker in Different Pseudomonas Aeruginosa Infections Using Gold Nanoparticles Modified Sensor. PLoS One 2019, 14 (7), 1–16. https://doi.org/10.1371/journal.pone.0216438.

[14] Maldonado, J.; Estévez, M. C.; Fernández-Gavela, A.; González-López, J. J.; González-Guerrero, A. B.; Lechuga, L. M. Label-Free Detection of Nosocomial Bacteria Using a Nanophotonic Interferometric Biosensor. Analyst 2020, 145 (2), 497– 506. https://doi.org/10.1039/c9an01485c.

[15] Ji, J.; Yang, C.; Zhang, F.; Shang, Z.; Xu, Y.; Chen, Y.; Chen, M.; Mu, X. A High Sensitive SH-SAW Biosensor Based 36° Y-X Black LiTaO3 for Label-Free Detection of Pseudomonas Aeruginosa. Sensors Actuators, B Chem. 2019, 281 (October 2018), 757–764. https://doi.org/10.1016/j.snb.2018.10.128.

[16] Zhao, F.; Niu, L.; Nong, J.; Wang, C.; Wang, J.; Liu, Y.; Gao, N.; Zhu, X.; Wu, L.; Hu, S. Rapid and Sensitive Detection of Pseudomonas Aeruginosa Using Multiple Cross Displacement Amplification and Gold Nanoparticle-Based Lateral Flow Biosensor Visualization. FEMS Microbiol. Lett. 2018, 365 (14), 1–6. https://doi.org/10.1093/femsle/fny147.

[17] Zhou, H.; Duan, S.; Huang, J.; He, F. An Ultrasensitive Electrochemical Biosensor 16 ForPseudomonas Aeruginosaassay Based on a Rolling Circle Amplification-Assisted Multipedal DNA Walker. Chem. Commun. 2020, 56 (46), 6273–6276. https://doi.org/10.1039/d0cc01619e.

[18] Das, R.; Dhiman, A.; Kapil, A.; Bansal, V.; Sharma, T. K. Aptamer-Mediated Colorimetric and Electrochemical Detection of Pseudomonas Aeruginosa Utilizing Peroxidase-Mimic Activity of Gold NanoZyme. Anal. Bioanal. Chem. 2019, 411 (6), 1229–1238. https://doi.org/10.1007/s00216-018-1555-z.

[19] Peng, H.; Chen, I. A. Rapid Colorimetric Detection of Bacterial Species through the Capture of Gold Nanoparticles by Chimeric Phages. ACS Nano 2019, 13 (2), 1244– 1252. https://doi.org/10.1021/acsnano.8b06395.

[20] Frederick, J.R., Elkins, J.G., Bollinger, N., Hasset, D.J., McDermott, T.R., 2001. Factors affecting catalase expression in Pseudomonas aeruginosa biofilms and planktonic cells. Appl Environ Microbiol. 67(3): 1375–1379. doi:10.1128/AEM.67.3.1375-1379.2001.

Annex

Industrial property resulting from this thesis

- **Invention patent: Process for storing and releasing protein-decorated nanoparticles on paper substrates**. Inventors / authors: Roberto de la Rica Quesada; Francy Alejandra Alba Patiño; Cristina Adrover Jaume. Entity holder of rights: University of the Balearic Islands and The Balearic Islands Health Research Institute (IdISBa). Application number: PCT/EP2020/075013.

Conference contributions

Oral Communications

- **Paper biosensor based on gold nanoparticles for the rapid detection of respiratory tract infections caused by Pseudomonas aeruginosa**. Authors: Francy Alejandra Alba Patiño; Antonio clemente; Roberto de la Rica Quesada. IEEE International Congress of Biomedical Engineering and Bioengineering (CI-IB&BI 2021). Virtual. Colombia. 2021. Conference paper DOI: 10.1109/CI-IBBI54220.2021.9626049.

Poster Presentations

- **Origami immunosensor for rapid detection of viral and bacterial infections**. Authors: Alejandra Alba-Patiño, Cristina Adrover-Jaume, Antonio Clemente, María del Mar González del Campo, Roberto de la Rica. NANO 2022, the 16th International Conference on Nanostructured Materials. Sevilla, Spain. 2022
- **Nanoparticle Reservoirs for Paper Inmunosensors**. Authors: Francy Alejandra Alba Patiño; Cristina Adrover Jaume; Roberto de la Rica Quesada. Nanotexnology 2020. Thessaloniki, Greek. 2020

Additional publications not included in this thesis

- **Micro - and nanosensors for detecting blood pathogens and biomarkers at different points of sepsis care**. Alba Patiño Alejandra, Vaquer Andreu, Barón Enrique, Russell Steven, Borges Marcio, De la Rica Roberto. Microchimica Acta. 2022. https://doi.org/10.1007/s00604-022-05171-2.

Publications resulting from this thesis